Doctor of Philosophy

Computational Exploration of Electronic Structure and
Lattice Thermal Transport in Novel 2D Semiconductor
M_xX_y (M=Cd/Ge, X=Te/S)

The Graduate School

of the University of Ulsan

Department of Physics

Asad Ali

Computational Exploration of Electronic Structure and

Lattice Thermal Transport in Novel 2D Semiconductor

M_xX_y (M=Cd/Ge, X=Te/S)

Supervisor: Prof. Young-Han Shin

A Dissertation

Submitted to

the Graduate School of the University of Ulsan

In Partial Fulfillment of the Requirements

for the Degree of

Doctor of Philosophy

by

Asad Ali

Department of Physics

University of Ulsan

February, 2024

University of Ulsan

Department of Physics

This dissertation, "Computational exploration of electronic structure and lattice thermal transport in novel 2D semiconductor M_xX_y (M=Cd/Ge, X=Te/S)" is hereby approved in partial fulfillment of the requirements for the degree of Doctor of Philosophy in physics.

Prof. Sung Lae Cho (Committee Chair)
Department of Physics, University of Ulsan

Prof. Jungdae Kim
Department of Physics, University of Ulsan

Prof. Tae Heon Kim
Department of Physics, University of Ulsan

Prof. Hye Jung Kim (External Examiner)
Department of Physics,
Pusan National University, Busan

Prof. Young-Han Shin (Supervisor)
Department of Physics, University of Ulsan

To my wife and parents, the guiding forces behind my PhD journey.

Declaration

I confirm that this PhD thesis is a product of my original work. Except for duly acknowledged references, it has not been previously presented or submitted for any other academic degree or qualification at this university or any other institution.

<div align="right">

Asad Ali

January 4, 2024

</div>

Acknowledgements

I would like to extend my heartfelt gratitude to several individuals who have contributed significantly to the completion of my PhD thesis. First and foremost, I express my deep appreciation to Prof. Young-Han Shin, my supervisor, for providing me with the opportunity to work in the Multiscale Materials Modeling Lab at the University of Ulsan. His unwavering guidance, invaluable expertise, and continuous support have been pivotal in shaping my research journey and achieving the milestones. I would also like to acknowledge BreanKorea21 (BK21) for providing funds during my PhD studies.

In addition to my supervisor, I am indebted to Dr. Kim, Dr. Abdus Samad (who also happens to be my brother), Dr. Hamid Ullah, and Dr. Aamir Shafique for their invaluable technical support and assistance. Their expertise and willingness to share their knowledge have been instrumental in tackling complex challenges during my research. Their collective contributions have undoubtedly enriched the quality and depth of my work.

I would also like to express my sincere appreciation to my current labmates, whose support have created a stimulating and collaborative research environment. Their insightful discussions, constructive feedback, and willingness to lend a helping hand have been invaluable in shaping my ideas and refining my research methodologies.

On a personal note, I would like to acknowledge the unwavering support and understanding of my wife, Shuhrat. Her encouragement, patience, and belief in my abilities have been a constant source of motivation throughout this challenging journey. I am also grateful for the support I received from my brother, Muktar Ali, who sadly passed away recently. During his time with me, his economic support, guidance, and encouragement played an influential role in my academic growth. Though he is no longer with us, his memory inspire me to persevere and make the most of the opportunities before me.

Furthermore, I express my heartfelt gratitude to my late mother, Musabbiha, and my father, Gohar Zaman. Their unwavering support and belief in my abilities have been guiding lights throughout my academic pursuit.

Abstract

The experimental realization of silicene and germanene opens a new avenue for exploring two-dimensional (2D) configurations of non-layered bulk materials. Previously, it was believed that monolayer forms were possible only for layered materials such as graphite, hexagonal boron nitride, and transition metal dichalcogenides, collectively known as Van der Waals (vdW) materials. In vdW materials, atoms within a layer are connected through chemical bonds, and the layers are attached via weak long-range vdW forces. In contrast, bulk materials have nearly isotropic bond strength in all directions, lacking a preferred cleavage plane as in layered materials, allowing the construction of various 2D layers from non-layered bulk materials. It often results in high surface reconstruction and the potential transition to new phases without corresponding bulk counterparts.

However, the search for the ground state among various possible initial structures for density functional theory (DFT) relaxations remains a challenge, especially for materials with polymorphic behavior such as Cd_xTe_y and Ge_xS_y. The ground-state phase of a material is significant due to its high possibility in experimental preparation. This thesis focuses on finding ground-state structures in the variable composition of 2D Cd-Te and Ge-S, exhibiting polymorphic characteristics. To address this complexity, the highly successful genetic algorithm-based code, USPEX, in conjunction with VASP for total energy calculations, is employed to predict low-energy phases. The results reveal CdTe as the ground state, with $CdTe_2$ being 8 meV/atom higher than the convex hull. For Ge-S, novel 2D structures of Ge_2S, GeS, and GeS_2 are identified, all exhibiting significantly lower formation energy than previously reported ones. The dynamic, elastic, and thermal stability of these low-energy structures are rigorously confirmed through state-of-the-art first principles methods.

This research emphasizes on the electronic structure of low-energy phases of 2D Cd-Te, crucial for solar cell applications, and the lattice thermal conductivity of 2D Ge-S, essential for thermoelectric device applications. Our analysis demonstrates the robust nature of the direct band structure of CdTe and the ultralow lattice thermal conductivity of GeS, making it promising for thermoelectric applications. Notably, the ground state structure of 2D GeS_2 exhibits giant anisotropic lattice thermal conductivity, surpassing that of other 2D materials. Detailed discussions on underlying mechanisms, including phonon group velocity, phonon

lifetimes, weighted phase space for three-phonon scattering, and Güneisen parameter, shed light on the ultralow and anisotropic lattice thermal conductivity observed in 2D GeS and GeS$_2$, respectively.

Contents

List of Figures

List of Tables

Chapter 1

Introduction

1.1 Polymorphism in crystals

Polymorphism, the ability of a material to exist in different crystal structures, is a subject of great interest and significance in materials science. In elemental solids, the different crystal forms are referred to as allotropes, and in compound solids, they are known as polymorphs. For example, carbon exhibits various allotropes [3]. Diamond and graphite are well-known examples due to their contrasting properties: diamond is renowned for its hardness, while graphite is soft. These distinct properties arise from their crystal structures, illustrated in figs. 1.1(a & b). Graphite has a layered structure where consecutive layers are held together by weak Van der Waal's forces, making it soft and slippery. In contrast, diamond features a non-layered bulk structure, making it the hardest natural material.

Similarly, compound materials like cadmium telluride (CdTe) can exist in different structures. The cubic and hexagonal structures, shown in figs. 1.1(c & d), are well-studied examples. Polymorphism stems from the various arrangements and bonding of atoms or molecules within a crystal lattice, resulting in distinct crystal structures with varying physical and chemical properties. The existence of multiple crystal structures for a given material offers a diverse range of material properties and applications.

The discovery and understanding of polymorphism in three-dimensional (3D) crystals have been extensively studied and well-established. Factors such as temperature, pressure, and composition can induce phase transitions between different crystal structures [4]. These phase transitions often lead to remarkable changes in material properties, including electrical conductivity, optical properties, mechanical strength, and thermal conductivity. Consequently, polymorphic materials have found applications in various fields, including electronics, catalysis, and thermoelectric devices.

(a) Diamond

(b) Graphite

(c) CdTe (cubic)
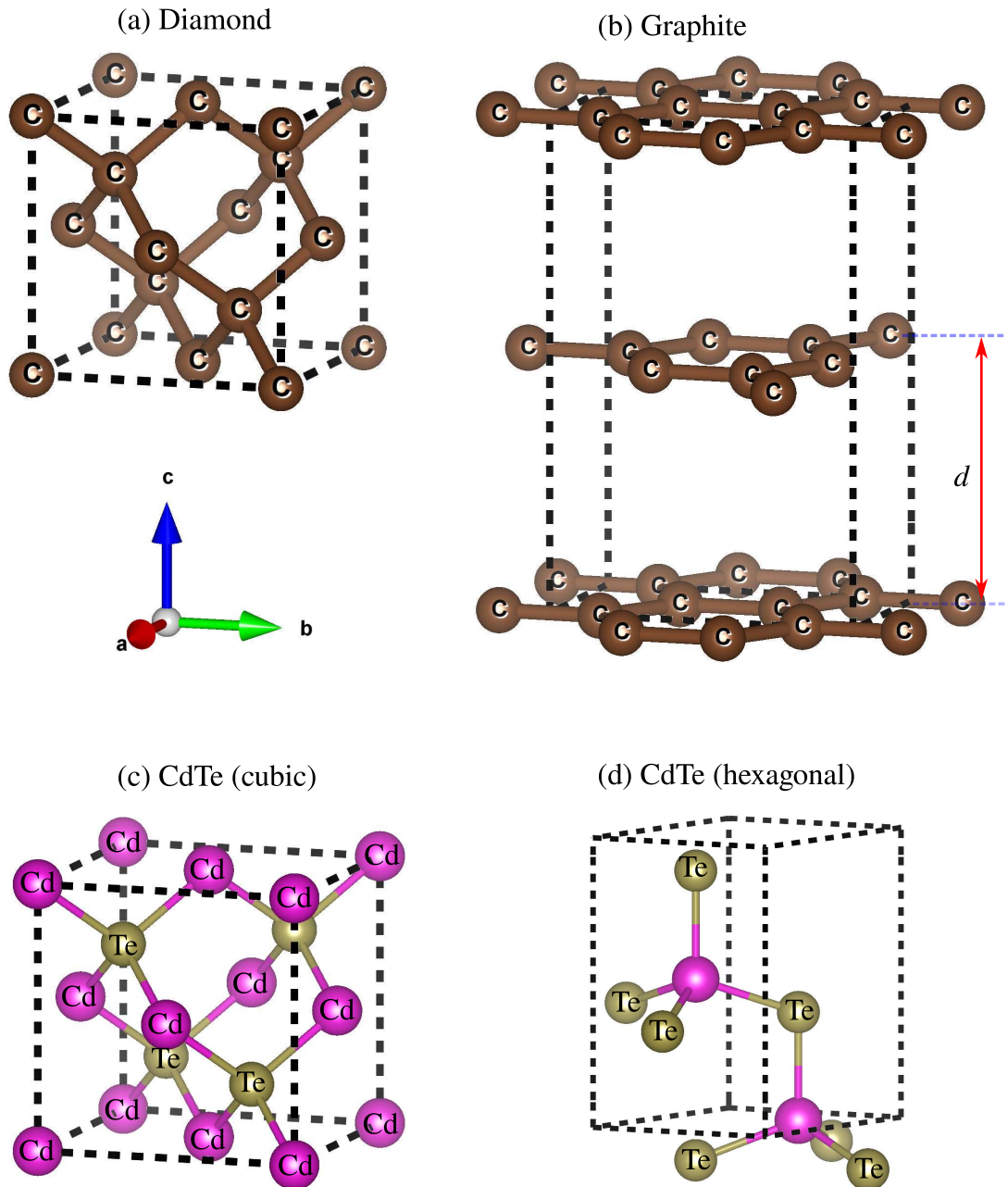
(d) CdTe (hexagonal)

Figure 1.1: Structures of carbon allotropes (a) Diamond, (b) Graphite, and CdTe polymorphs (c) cubic, and (d) hexagonal

1.2   Polymorphism in two-dimensional (2D) materials

In recent years, the emergence of two-dimensional (2D) materials has expanded the scope of polymorphism studies beyond 3D crystals. These 2D materials, composed of a single layer or a few layers of atoms, exhibit unique properties due to their reduced dimensionality. Graphene [5, 6], the well-known 2D material composed of carbon atoms arranged in a hexagonal lattice, sparked tremendous interest in the field. Since then, researchers have explored a diverse range of 2D materials, including transition metal dichalcogenides (TMDs), phosphorene, hexagonal boron nitride, and many more.

Similar to their 3D counterparts, 2D materials can exhibit polymorphism, although with distinct characteristics. For monolayers whose bulk counterpart is layered, these polymorphs often result from various stacking, buckling, and bending of the single layer. However, in the case of monolayers of non-layered bulk materials, such as CdTe, the structures of these polymorphs could be vastly different from each other due to the absence of a preferred cleavage plane. For example, we show four polymorphs of 2D CdTe in fig. 1.2, i.e., single-layer flat and buckled and bilayer low and high-buckled structures from the literature [7–9]. Additionally, a 2D CdTe with a unit cell of 8 atoms has also been reported [10].

The constraints imposed by reduced dimensionality and surface reconstruction can lead to different crystal structures and arrangements of atoms within the 2D plane. These variations in structure result in distinct electronic, optical, and mechanical properties. For example, the direct band gap of monolayer MoS_2 becomes indirect with increasing thickness [11]. Consequently, understanding and characterizing polymorphism in 2D materials are crucial for tailoring their properties for specific applications.

1.3   Ground-state structure

The structure within the configuration space with the lowest total energy is referred to as the ground state of that material, while those with higher energies are considered meta-stable structures. The importance of the ground state lies in the fact that every natural system aims to minimize its energy. Consequently, the likelihood of a material existing in its ground-state structure is higher compared to a meta-stable state. However, claiming a structure to be the ground state of a material is subjective. This means that the energy of the alleged ground-state structures is compared with various structures in the configuration space. Total energy calculation codes depend on the initially provided structure. If the initial structure is significantly different from the global minimum, there is a high probability of getting trapped in local energy minima. To accurately determine the ground state of a material, a wide range

(a) 1L (flat)   (b) 1L (buckeld)

Top-view

Side-view

(c) 2L (low-buckled)   (d) 2L (high-buckled)

Top-view

Side-view
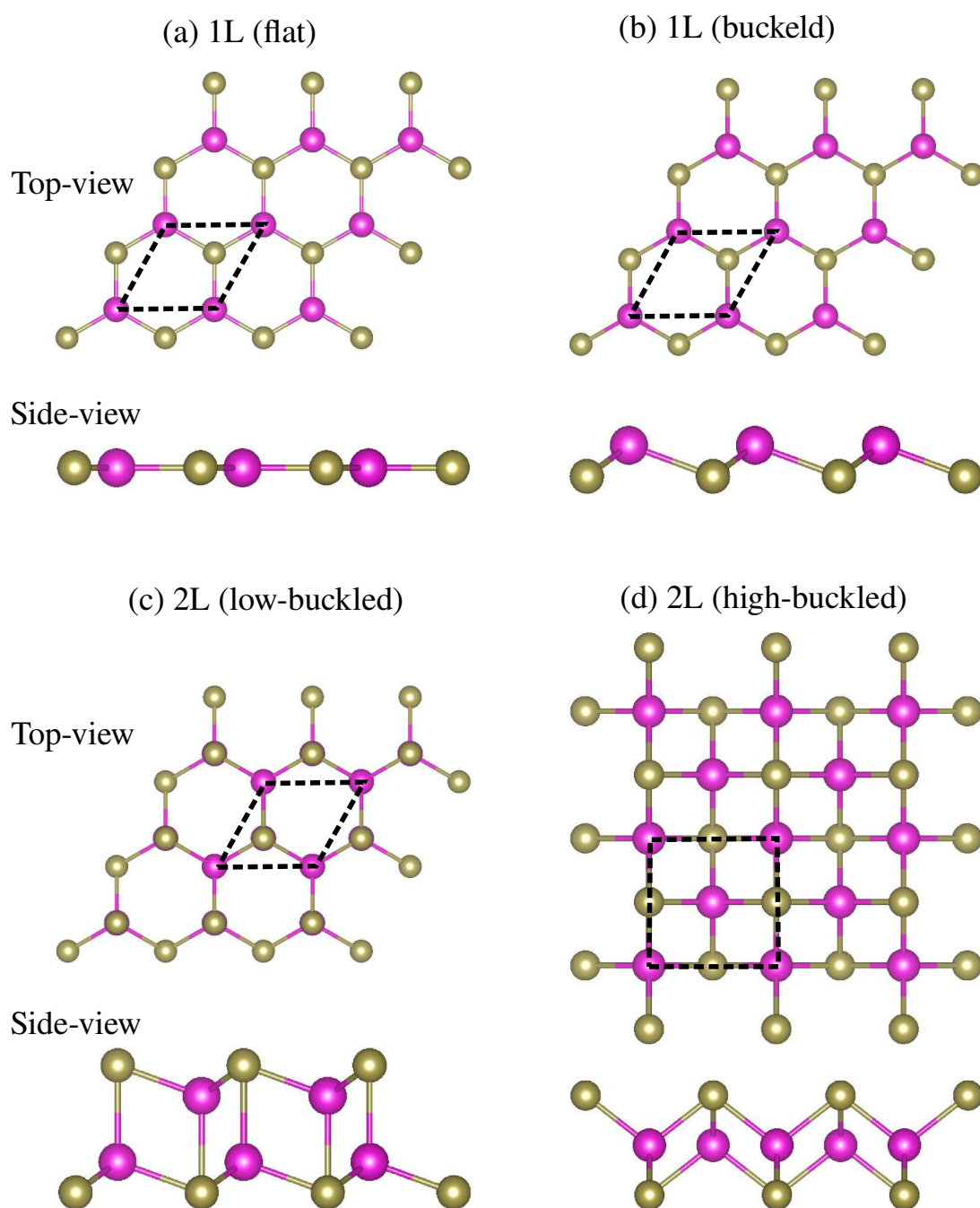
Figure 1.2: Two-dimensional CdTe polymorphs found in the literature. The dashed lines mark the unit cell in each case.

of initial structures with varying numbers of atoms in the unit cell should be considered.

1.4 Significance of evolutionary algorithms

The prediction of global minimum energy structure in 2D materials are challenging tasks due to the complex configuration space and the presence of local minima in energy landscape. The configuration space illustrates the different arrangements of atoms within a material. Typically, it's a high-dimensional $3N$ space, where N represents the number of atoms in the unit cell. This intricate nature poses challenges, especially when dealing with polymorphic and non-layered bulk materials like CdTe and GeS, where a preferred cleavage plane is absent. Identifying the ground-state configuration becomes exceptionally challenging in such cases. Employing strategic search methods becomes crucial to navigate this complexity and find the most stable arrangement and other feasible configurations in these materials. Recently, evolutionary algorithms have emerged as powerful tools for efficiently exploring this configuration space and identifying global-minimum energy polymorphs.

Evolutionary algorithms are inspired by biological evolution and mimic the process of natural selection and genetic variation. These algorithms employ a population of candidate structures, subject them to evolutionary operators such as mutation and crossover, and iteratively refine the population towards more favorable solutions. The use of evolutionary algorithms enables efficient exploration of the configuration space, significantly increasing the chances of discovering novel and stable polymorphs.

The incorporation of evolutionary algorithms in the prediction of 2D material polymorphs offers several advantages. Firstly, they can efficiently sample a wide range of structural possibilities, enabling the discovery of polymorphs that may have been overlooked using traditional methods. Secondly, these algorithms can guide the search towards global-minimum energy structures, thereby providing more accurate predictions of the most stable polymorphs. Thirdly, evolutionary algorithms allow for the exploration of composition-structure-property relationships, aiding in the design and optimization of materials with tailored properties.

1.5 Why CdTe and GeS?

Silicon, a widely used material in solar cells, faces limitations in efficiency due to its indirect band gap. It has led the search for alternative materials, with Cadmium Telluride (CdTe) gaining significant attention due to its favorable direct band gap of 1.45 eV. The demand for two-dimensional (2D) materials has surged following the successful isolation of graphene and other metal chalcogenides, making it imperative to fabricate a 2D sheet of CdTe experimen-

tally. Although there have been reports on the synthesis of CdTe nanoplatelets and nanorods, the elusive 2D form has yet to be realized. On the theoretical front, density functional theory (DFT) studies have unveiled the monolayer of CdTe in various forms, including flat single-layer hexagonal, bilayer hexagonal, and buckled configurations. However, a significant gap in the literature pertains to the absence of investigations into ground-state structure, which holds more practical relevance for experimentalists. Moreover, understanding the influence of strain and thickness, which are ubiquitous factors in experimental preparation, on the electronic structure remains a critical area of research. By addressing these crucial aspects, we can not only enhance our fundamental understanding but also pave the way for the practical utilization of 2D CdTe in emerging technologies.

The conversion of waste heat into useful electrical energy is a critical pursuit, addressing both the global energy crisis and environmental sustainability. The figure of merit, ZT, serves as a vital metric for quantifying the efficiency of material in this conversion process and is directly related to the Seebeck coefficient while being inversely proportional to thermal conductivity. Consequently, there is a growing demand for semiconductors exhibiting ultralow lattice thermal conductivities. In this context, 2D materials emerge as a promising avenue for enhancing thermal transport properties. Among these materials, 2D IV-VI compounds have captured the research community's attention. For instance, the 2D orthorhombic structure of GeS has demonstrated a higher Seebeck coefficient and low lattice thermal conductivity. However, the non-layered, low-energy bulk structure of GeS hints at the possibility of other 2D configurations beyond the orthorhombic phase. Surprisingly, a comprehensive investigation into the ground-state structure of 2D GeS is absent in the literature.

Slack's theory suggests that materials exhibiting high average atomic mass with weak bonds tend to have low lattice thermal conductivity, which is advantageous for heat-to-electricity conversion. We're interested in a group of 2D materials, M_xX_y (M=Cd/Ge, X=S/Te), that include heavy metals. These materials may possess remarkably low lattice thermal conductivity, but their thermal transport properties remain largely unexplored in the literature. Investigating these properties could unlock promising options for efficient heat-to-electrical conversion.

1.6   Phonon transport in 2D materials

Phonon transport in 2D materials is crucial for a comprehensive understanding of their thermal properties and potential for thermoelectric applications. Phonons, the quantized vibrations of the crystal lattice, are the primary heat carriers in semiconducting materials. The study of phonon transport involves investigating the propagation, scattering, and thermal conductivity of phonons in 2D materials.

Phonon transport in 2D materials is influenced by various factors, including the material's crystal structure, phonon dispersion relations, and phonon-phonon scattering mechanisms. The unique 2D nature of these materials introduces additional considerations, such as the presence of edge states and the impact of substrate interactions. The band gap in semiconducting 2D materials further affects the phonon transport properties, as phonons with energies close to the band gap can exhibit reduced scattering rates and contribute significantly to thermal conductivity.

Understanding the phonon transport characteristics in polymorphic structures of 2D materials allows for the optimization of thermal management strategies and the design of thermo-electric devices. Additionally, it provides insights into the interplay between electronic and thermal properties in 2D materials and facilitates the exploration of their potential for energy conversion and heat dissipation applications.

1.7 Research objectives

Building upon the aforementioned concepts and considerations, the research objectives of this thesis are as follows:

1. To employ evolutionary algorithms in conjunction with stability analysis techniques to predict polymorphic structures in 2D materials, specifically focusing on Cd_xTe_y, Ge_xS_y.

2. To investigate the structural stability, including dynamical, thermal, and mechanical stability, of the identified low-energy structures by state-of-the-art first-principles methods.

3. To study the electronic properties, including energy band structures and density of states, of the low-energy structures for their implications in potential applications.

4. To explore the phonon transport characteristics in low-energy structures of 2D materials, due to the semiconducting nature of the predicted monolayers.

5. To assess the effects of thickness and strain on the electronic structure of CdTe, $CdTe_2$, which are ubiquitous during synthesis.

1.8 Significance of the study

The comprehensive investigation of polymorphism, stability, electronic structure, and phonon transport in 2D materials contributes to the advancement of fundamental knowledge and paves the way for the design and optimization of materials with tailored properties. The prediction of low-energy polymorphs, incorporating stability analysis, enhances the discovery of stable and viable structures, expanding the design space for 2D materials. Understanding the electronic

structure and phonon transport properties enables the rational design of materials for diverse electronic, optoelectronic, and thermoelectric applications.

1.9   Thesis outline

In order to achieve the research objectives outlined earlier, this thesis is structured as follows:

Chapter 2 offers a comprehensive theoretical foundation, providing essential insights into the computational methodologies utilized for generating and analyzing the results presented in this thesis.

Chapter 3 delves into a detailed exploration of the outcomes related to 2D CdTe and $CdTe_2$. While focusing on these materials, we briefly touch upon meta-stable structures such as $CdTe_4$ and Cd_3Te_2.

Chapter 4 offers an in-depth investigation into the prediction of low-energy structures within 2D Ge_xS_y compounds. It primarily concentrates on the lattice thermal conductivity of these low-energy structures, shedding light on their unique characteristics.

In Chapter 5, we provide a comprehensive summary of our findings and their implications. Furthermore, we outline the direction for future studies, offering an outlook on the exciting possibilities that lie ahead.

Chapter 2

Theoretical background and computational methods

In this chapter, the background of density functional theory (DFT) and the key computational methods utilized in the thesis are presented. The discussion commences by addressing the complex many-body problem and its three essential approximations. Following this, the application of density functional theory as a solution to this intricate problem is explained.

2.1 Atomic scale interactions

At a microscopic level, all materials consist of molecules or atoms, comprising nuclei and electrons. The way these components change over time and space can be described using the Schrödinger wave equation:

$$\hat{H}\psi = i\hbar\frac{\partial\psi}{\partial\psi} \tag{2.1}$$

where the Hamiltonian $\hat{H}$ can be represented as follow:

$$\hat{H} = -\frac{\hbar^2}{2m_i}\sum_i \nabla_i^2 - \sum_I \frac{\hbar^2}{2m_I}\nabla_I^2 - \sum_{i,I}\frac{Z_I e^2}{|r_i - R_I|} + \frac{1}{2}\sum_{i\neq j}\frac{e^2}{|r_i - r_j|} + \frac{1}{2}\sum_{I\neq J}\frac{Z_I Z_J e^2}{|R_I - R_J|}. \tag{2.2}$$

In this context, the subscript denoted by small letters signifies electrons, while capital letters represents nuclei. For instance, the mass and position of ith electron as m_i, r_i and I^{th} nucleus with m_I, r_I. Since the Hamiltonian ($\hat{H}$) in eq. 2.2 is not dependent of time, the wave function ψ can be expressed as $\psi(\{r_i\},t) = \phi_E(\{r_i\},t)e^{-iEt}$. Consequently, the Schrödinger

wave equation simplifies as:

$$\hat{H}\psi = E\psi \tag{2.3}$$

where E stands for the total energy of the system. Moreover, due to the significant mass difference between the nucleus and electron, the kinetic energy of the nuclei term can be disregarded. By employing this approximation (known as Born-Oppenheimer's approximation [12]), the Hamiltonian can be simplified to depict a system where the motion of the nuclei is considered static or frozen as:

$$\hat{H} = -\frac{\hbar^2}{2m_i}\sum_i \nabla_i^2 - \sum_{i,I}\frac{Z_I e^2}{|r_i - R_I|} + \frac{1}{2}\sum_{i\neq j}\frac{e^2}{|r_i - r_j|} + \frac{1}{2}\sum_{I\neq J}\frac{Z_I Z_J e^2}{|R_I - R_J|}. \tag{2.4}$$

In this expression, the final term remains constant for a specific structure, given the known positions and charges of the nuclei. Consequently, an electron-only Hamiltonian can be derived as:

$$\hat{H}_e = \underbrace{-\frac{\hbar^2}{2m_i}\sum_i \nabla_i^2}_{\hat{T}_e} \underbrace{- \sum_{i,I}\frac{Z_I e^2}{|r_i - R_I|}}_{\hat{V}_{ext}} + \underbrace{\frac{1}{2}\sum_{i\neq j}\frac{e^2}{|r_i - r_j|}}_{\hat{V}_{ee}} \tag{2.5}$$

This Hamiltonian consists of three parts: $\hat{T}_e$ (electron kinetic energy), $\hat{V}_{ext}$ (external potential energy due to stationary nuclei), and $\hat{V}_{ee}$ (Coulomb repulsion between electrons). Electron masses vary due to relativistic effects at high speeds, but this complexity is often simplified. Accurately calculating $\hat{V}_{ee}$ requires a many-body wave function with $3N$ variables, making exact calculations impossible for systems with more than two electrons.

Initially, the problem was tackled by Hartree, who averaged electron interactions, allowing each electron to respond to the effective potential generated by the other N-1 electrons. This simplified the problem, representing each electron solely through the electron density distribution of the remaining electrons, regardless of their exact positions. This approach reduced the complex many-body electron wave function into a product of individual electron wave functions, from which the single electron Hamiltonian equations were derived through the variational principle.

However, the Fermionic nature of electrons posed a challenge due to the Pauli exclusion principle. To address this, the Hartree-Fock formalism was introduced, representing the many-body wave function in a Slater determinantal form. Although this was an improvement, it introduced an additional potential (exchange potential) into the resulting Hamiltonian equation. While effective for small systems, these methods lacked accuracy, primarily due to the neglect of electron correlation effects.

Both the Hartree and Hartree-Fock methods relied on wave functions, demanding substan-

tial computational resources, particularly for large systems. Constructing the wave function for an N-electron system necessitated 4N variables, leading to a significant increase in complexity with a growing number of electrons. In response, a density functional-based approach emerged, gaining popularity in computational studies of condensed matter physics and chemistry. Unlike wave function-based methods, this approach focused on the degree of freedom of electron density, involving only four variables (three spatial and one spin variable) in an N-electron system. This made it far more manageable for larger systems.

2.2 Density functional theory (DFT)

2.2.1 Principles of DFT: Hohenberg-Kohn theorems

Density Functional Theory (DFT) operates on the principle that a system's characteristics can be exclusively defined by its ground state density [13, 14], denoted as $n_0(r)$. This fundamental concept, established by Hohenberg and Kohn [15] in 1964, represents a pivotal breakthrough. It introduces a precise theory for interacting many-body systems, grounded in two fundamental principles.

Firstly, in a system composed of equivalent Fermi particles, disregarding spins, the ground state energy is solely dictated by the particle density distribution function, $\rho(r)$. Thus, it's feasible to entirely describe a system without delving into its wavefunctions or spin densities.

Secondly, the energy function $E[\rho]$ achieves its minimum value precisely when ρ corresponds to the ground state, with $E[\rho]_{min}$ representing the ground state energy. This principle, integral to density functional theory, serves as a variational approach, providing a method for employing variational methods to tackle specific problems. The Hohenberg-Kohn formalism emphasizes that the particle density function ρ stands as the pivotal variable defining a many-body system's ground state properties. The variation in the energy functional $E[\rho]$ offers a means to identify a system's ground state accurately.

In summary, as per the Hohenberg and Kohn theorem, both the ground state energy and particle density function can be ascertained by minimizing:

$$E[\rho] \equiv \int dr \upsilon_{ext}(\mathrm{r}) + < \psi | T + U | \psi >, \tag{2.6}$$

Here, $\upsilon_{ext}(\mathrm{r})$ represents the external potential energy at position r, while T signifies the kinetic energy of electrons, and U denotes the interaction energy between electrons. The term

$<\psi|T+U|\psi>$ in eq. 2.6 can be written as:

$$<\psi|T+U|\psi> = T[\rho] + \underbrace{\frac{1}{2}\int d\mathbf{r}d\mathbf{r}'\frac{\rho(\mathbf{r})\rho(\mathbf{r}')}{|\mathbf{r}-\mathbf{r}'|}}_{J_H} + E_{ncl}[\rho], \tag{2.7}$$

The first two terms on the right side of eq. 2.7 represent the functions for electron kinetic energy and Coulomb interactions among electrons (Hartree term), respectively. The third term, $E_{ncl}[\rho]$, incorporate the non-classical factors such as self-interaction, exchange, and correlation effects. Minimizing the energy functional $E[\rho(\mathbf{r})]$ allows for the determination of the ground state density distribution and the total energy corresponding to it. However, while the external potential and the Hartree terms in eq. 2.7 are known, the precise forms of the other terms still require determination.

2.2.2 Kohn-Sham (KS) DFT

To address the unknown terms in the Hohenberg-Kohn equation, W. Kohn and L. J. Sham [16] introduced a practical solution. The Kohn-Sham formalism involves replacing the kinetic energy (T) and non-classical term (E_{ncl}) of the many-body system with a sum of the exact kinetic energy of a non-interacting system (T_s) possessing the same charge density distribution, and an exchange-correlation term E_{XC}. This modification results in

$$T[\rho(\mathbf{r})] + J_H[\rho(\mathbf{r})] + E_{ncl}[\rho(\mathbf{r})] = T_s[\rho(r)] + J_H[\rho(\mathbf{r}) + E_{XC}[\rho(\mathbf{r})] \tag{2.8}$$

The $T_s[\rho(\mathbf{r})]$ term can be expressed as a functional of the individual electron Kohn-Sham orbitals as:

$$T_s[\rho(\mathbf{r})] = -\frac{\hbar^2}{2m_e}\sum_{i=1}^{occ}<\psi_i|\nabla_i^2|\psi_i>. \tag{2.9}$$

Therefore, the system's energy functional can be expressed as

$$E_{KS}[\rho(\mathbf{r})] = T_s[\rho(\mathbf{r})] + J_H[\rho(\mathbf{r})] + V_{ext}[\rho(\mathbf{r})] + E_{XC}[\rho(\mathbf{r})]. \tag{2.10}$$

In this approach, T_s and J_H describe the electron distribution and apply universally to all systems. The unique electronic properties of different structures stem from their distinct external potentials (V_{ext}). Although the exchange-correlation term remains undefined (next section), we can deduce the system's ground state energy form by employing the Hohenberg-Kohn theorem, that minimizing the energy functional gives the ground state of the system. This minimization process gives rise to the Kohn-Sham equation, which resembles the Schrödinger equation.

$$H_{KS}(\mathrm{r})\psi_i(\mathrm{r}) = \left[-\frac{1}{2}\nabla^2 + V_{KS}(\mathrm{r})\right]\psi_i(\mathrm{r}) = \varepsilon_i\psi_i(\mathrm{r}), \tag{2.11}$$

where

$$V_{KS}(\mathrm{r}) = V_{ext}(\mathrm{r}) + V_H(\mathrm{r}) + V_{XC}(\mathrm{r}), \tag{2.12}$$

in which the Hartree and exchange-correlation potentials are written as

$$V_H = \int \frac{\rho(\mathrm{r}_2)}{|\mathrm{r} - \mathrm{r}_2|}d\mathrm{r}_2 \tag{2.13}$$

$$V_{XC} = \frac{\delta E[\rho(\mathrm{r})]}{\delta\rho(\mathrm{r})}. \tag{2.14}$$

Subsequently, the electron density distribution of the system's ground state can be calculated as follows:

$$\rho(\mathrm{r}) = \sum_{i=1}^{occ} |\psi_i(\mathrm{r})|^2. \tag{2.15}$$

Next, the total energy can be determined by summing the energy values of the occupied eigenstates.

Now, the only remaining term in the eq. 2.15 is the exchange-correlation term $E_{XC}[\rho(\mathrm{r})]$, for which several efficient approximations have been introduced.

2.3 Density functionals approximations

2.3.1 Local density approximation

Utilizing the Hohenberg-Kohn-Sham equation, the many-body system can be evaluated through a single-particle model. However, it is pivotal to choose an effective $E_{XC}[\rho(\mathrm{r})]$ term for accurate calculations. Several approximations have been proposed to determine a suitable $E_{XC}[\rho(\mathrm{r})]$, with one widely used method being the local density approximation (LDA) introduced by W. Kohn and L. J. Sham [16]. This approach essentially involves approximating the exchange-correlation functional of electrons by considering that of the uniform electron gas.

$$E_{XC}(\rho) = \int d\mathrm{r}\rho(r)\varepsilon_{XC}[\rho(\mathrm{r})] \tag{2.16}$$

The corresponding exchange-correlation potential is given as:

$$V_{XC}[\rho(\mathrm{r})] = \frac{\delta E_{XC}[\rho]}{\delta\rho} = \frac{d}{d\rho(r)}(\rho(r)\varepsilon_{XC}[\rho(\mathrm{r})]) \tag{2.17}$$

It is possible to obtain ε_{XC} for a uniform electron gas with various ρ, and then determine $\rho(r)$ using interpolation. The exchange-correlation term can be split into the exchange term ε_X and the correlation term ε_C. Dirac defined the exchange term ε_X as follows:

$$\varepsilon_X(\rho) = -\frac{3}{4}[\frac{3\rho}{\pi}]^{1/3} \tag{2.18}$$

However, there is no analytical solution for the correlation part. Typically, it is parameterized based on Quantum Monte Carlo simulations results.

When compared to experimental results, LDA often faces issues like overestimating binding energy and underestimating bond length and bandgap. This is especially problematic in systems with uneven electron density, such as transition metal oxide systems, where LDA's performance weakens due to the interdependence of exchange-correlation energy on electron densities across positions.

2.3.2 Generalized-gradient approximation

A frequently applied enhancement to LDA involves expanding the exchange-correlation energy density beyond local electron density to include neighboring spaces [15]. This improvement incorporates the electron density gradient, resulting in a first-order correction to the exchange-correlation energy density.

$$E_{XC}[\rho] = \int dr \varepsilon_{XC}[\rho(r), |\nabla \rho(r)|]. \tag{2.19}$$

Several methods based on Generalized Gradient Approximation (GGA) have been introduced, including approaches like Perdew-Wang (PW91) [17], Perdew-Burke-Ernzerhof (PBE) [18, 19], and others.

2.3.3 Hybrid density functional

As the exchange-correlation terms in LDA and GGA lack precision, properties like bond lengths and energy band gaps often deviate significantly from experimental findings. To enhance accuracy, hybrid functional methods, pioneered by A. Beck [20], have been introduced. These methods utilize a hybrid exchange-correlation energy functional, typically combining Hartree-Fock exchange E_X^H with LDA or GGA exchange-correlation energy functionals. Various hybrid functional methods, including B3LYP , PBE0 [21, 22], etc., have been proposed. In this study, a Heyd-Scuseria-Ernzerhof (HSE) [23] exchange-correlation functional is employed for accurate band structures.

2.4 Applying KS equation to periodic crystals

2.4.1 Plane wave basis

The mentioned equations are applicable to systems with a finite number of electrons, like molecules and atoms. However, crystal systems have an infinite number of electrons. In solid crystal systems, the periodic nature allows the equations to have periodic boundary conditions, simplifying and enabling the solution of the KS equations. In a periodic crystal characterized by a lattice translational vector R, the effective potential V_{KS} complies:

$$V_{KS}(\mathbf{r}+\mathbf{R}) = V_{KS}(\mathbf{r}). \tag{2.20}$$

The KS wave function adheres to the following boundary condition:

$$\psi_{l,k}(\mathbf{r}+\mathbf{R}) = e^{i\mathbf{k}\cdot\mathbf{r}}\psi_{l,k}(\mathbf{r}), \tag{2.21}$$

$$\psi(l,\mathbf{r}) = e^{i\mathbf{k}\cdot\mathbf{r}}\omega_{l,k}(\mathbf{r}), \tag{2.22}$$

$$\omega_{l,k}(\mathbf{r}) = \omega_{l,k}(\mathbf{r}+\mathbf{R}) \tag{2.23}$$

Here, k, l represent the Bloch wave vector and the band index, $\psi_{l,k}(\mathbf{r})$, $\omega_{l,k}(\mathbf{r})$ stands for the Bloch wave function and the periodic function, respectively.

Achieving an accurate representation of the wave function necessitates a thorough and inclusive basis set that encompasses all regions within the crystal. Different approximations are utilized in various basis sets, such as linearized augmented plane waves (LAPW), linear combination of atomic orbitals (LCAO), and plane waves (PW). In this section, our focus is solely on introducing the PW approximation. The periodic wave function can be expressed as Fourier series:

$$\omega_{l,k} = \sum_{G} c_{l,G} e^{iG\cdot r}, \tag{2.24}$$

Where G denotes the reciprocal lattice vector, satisfying the condition $G\cdot r = 2\pi m$, where m is an integer. The $c_{l,G}$ represents the expansion coefficient for plane waves. As a result, the KS orbitals can be represented as a linear combination of the complete PW basis set as:

$$\psi_{l,k}(\mathbf{r}) = \sum_{G} c_{l,k}(G) \times \frac{1}{\sqrt{\Omega}} e^{i(k+G)\cdot\mathbf{r}}, \tag{2.25}$$

Here, $c_{l,k}$ stands for the expansion coefficient for the basis set, while $1/\sqrt{\Omega}$ (with Ω is volume)

as the normalization factor. The KS equation can be formulated as follows:

$$\left(-\frac{\hbar^2}{2m_e}\nabla^2 + V_{KS}(\mathbf{r}) \right) \psi_{l,k} = \varepsilon_{l,k}\psi_{l,k}(\mathbf{r}) \tag{2.26}$$

Upon multiplication with $e^{-i(k+G')\cdot r}$ on the left side and subsequent integration over r, we obtain:

$$\sum_{G'} \left(-\frac{\hbar^2}{2m_e}|k+G|^2\delta_{G'G} + V_{KS}(G-G') \right) c_{l,k}(G) = \varepsilon_{l,k}c_{l,k}(G). \tag{2.27}$$

In this equation, the effective potential energy V_{KS} is expressed through Fourier transforms, and the kinetic energy by diagonal components. By diagonalizing the Hamiltonian matrix $H_{k+G,k+G'}$ the equation can be solved.

The computational size is determined by selecting a cutoff energy

$$E_{cutoff} = \frac{\hbar^2}{2m_e}|k+G_{max}|^2 \tag{2.28}$$

Obtaining a meaningful solution involves considering both valence and core electrons, but this can be computationally expensive. Thus, the pseudopotential approximations are introduced.

2.4.2 Pseudopotentials

In a crystal, the core electrons are tightly bound to the nuclei. Their interaction with the surrounding crystalline environment is weak, allowing us to merge the core electron potential with the nuclear Coulomb potential. This combination reduces the number of electrons that require computation and leads to the creation of a pseudopotential. This technique is known as the Frozen-Core Approximation. The pseudowavefunction corresponding to the pseudopotential can be represented in the form plane waves (PW).

2.4.3 Projector augmented wave method

The DFT results in this thesis uses Vienna Ab initio Simulation Package (VASP) [24, 25], which is based on the projector augmented wave (PAW) method [26, 27]. It was introduced by Blöchl, and is based on pseudopotential approach considering all-electron. This method divides the space into two distinct regions: the augmented (core) region and the outer region. The core region behave as spheres around each nucleus, is less system-dependent and less significant. On the other hand, the outer region is crucial for studying solid properties. The PAW method adopts a strategy of splitting the wavefunction into two components: one within

the augmented area and the other in the outer region. These two wavefunctions are smoothly connected at the interface of the two regions.

2.5 Hellmann-Feynman force

In a DFT calculation aiming to find the local energy minimum for a given structure, one can calculate the first derivative of the energy surface, which represents the force. At the local minimum, this first derivative of the energy surface must be precisely zero. The force acting on atom i can be determined through the first derivative of the energy (E) with respect to its position R_i.

$$F_i = -\frac{\partial E}{\partial R_i},$$ (2.29)

where

$$E = \frac{\langle \psi | H | \psi \rangle}{\langle \psi | \psi \rangle} = \langle \psi | H | \psi \rangle.$$ (2.30)

substituting E in eq. 2.30 and using $H|\psi\rangle = E|\psi\rangle$, we get

$$F_i = -\langle \psi | \frac{\partial H}{\partial R_i} | \psi \rangle - E\left(\frac{\partial \langle \psi | \psi \rangle}{\partial R_i}\right) = -\langle \psi | \frac{\partial H}{\partial R_i} | \psi \rangle.$$ (2.31)

Eq. 2.31 represents the Hellmann-Feynman forces. During a geometry optimization, the Hellmann-Feynman force acting on each atom in a structure must meet the given convergence criteria.

2.6 Electron localization function

The Electron Localization Function (ELF) serves as a scalar field in three-dimensional space, offering a straightforward measure of electron localization in atomic and molecular systems [28]. This method proves highly effective in analyzing electron spatial distribution within materials, providing insights into bond types and arrangements. ELF alone has demonstrated its ability to identify bonds and lone pairs in molecules and solids [29–31], making it invaluable in characterizing material properties. The ELF is defined as follows:

$$ELF(r) = \frac{1}{1 + \chi(r)}$$ (2.32)

where $\chi(r)$ represents the ratio of electron localization $D(r)$ to uniform electron density $D_h(r)$:

$$\chi(r) = \frac{D(r)}{D_h(r)}$$ (2.33)

$D(r)$ and $D_h(r)$ can be computed from Hartree-Fock or Kohn-Sham orbitals $\psi_i(r)$ and electron density $\rho_e(r)$ as:

$$D(r) = \frac{1}{2} \sum |\nabla \psi_i(r)|^2 - \frac{1}{8} \frac{|\nabla \rho_e(r)|}{\rho_e(r)}, \tag{2.34}$$

$$D_h(r) = \frac{3}{10} (3\pi^2)^{2/3} \rho_e(r)^{5/3} \tag{2.35}$$

The $ELF(r)$ can have to the values in range 0 to 1, with 1 corresponds to complete localization of electron.

2.7 Evolutionary search method

Crystal structure prediction, as defined by A. Le Bails [32], strives to anticipate a crystal structure before it is confirmed through chemical synthesis or discovered naturally. This facet of crystallography revolves around deducing structures solely through theoretical means, freeing the process from experimental dependencies. Although methods like X-ray diffraction or neutron scattering are frequently utilized, they face challenges, particularly in the realm of 2D materials. Issues such as sample purity, the intensity of light sources, and associated costs frequently complicate the direct experimental determination of a material's structure. In theory, the key factor determining a structure's potential stability is its total energy. While it's often challenging to confirm a structure as the lowest energy state, we can assess its stability by comparing it with numerous other available structures.

Numerous methods have been devised for structure prediction, among which the evolutionary algorithm stands out as highly efficient. Its application has markedly decreased the need for experimental structural information in theoretical investigations of 2D materials [33–35]. Consequently, theoretical results have gained enhanced reliability and credibility in the scientific community.

The steps involved in an evolutionary structure search utilizing the USPEX code [36–38] are illustrated in figure 2.1

1. The first generation is created using the crystal symmetries and the input given as constant/variable chemical composition, maximum and minimum number of atoms in the unit cell, and the vacuum thickness (specifically for 2D materials).

2. These initial structures undergo relaxation using DFT codes such as VASP. Following complete geometry optimization, one obtains the structures at local energy minima along with their respective energies.

3. In step 2, the low-energy structures will serve as seed structures for the next genera-
   tion, whereas additional structures are created through heredity, mutation, and random
   process. To achieve the ground state which has lowest-energy, structures with lower
   energies of previous generation have a greater likelihood as parent structures.

4. Continue iterating the loop from step 2 until the convergence criteria is met. Conver-
   gence is achieved when the lowest energy structures remain unchanged across multiple
   generations. The structure displaying the absolute minimum energy is identified as the
   global minimum structure in the search process.

The heredity operator in step 3 involves dividing the unit cell into multiple segments and sub-
sequently assembling these segments to create a new structure. The mutation operator entails
exchanging the chemical composition among distinct structural components. The search can
be speed up by giving some known structure (if available) as seed. Furthermore, the num-
ber of the structures in the first generation should be larger (around twice) than subsequent
generations to increase the probability of finding the global minimum.

2.8   Lattice vibration in solids

In materials like dielectric and semiconducting materials, heat is transferred through the vi-
brational movments of atoms, which are interconnected by interatomic forces. Figure 2.2(a)
illustrates the interatomic potential U as a function of the interatomic distance r between two
atoms. The force interaction between these atoms can be derived from the first derivative of
U with respect to r as [1]:

$$F = \frac{-dU}{dr} \tag{2.36}$$

When two atoms are at a distance, they experience an attractive force because of the attrac-
tion between one atom's electrons and the nucleus of the other. However, as they get closer,
they repel each other due to the overlap of atomic orbitals. The position at which the potential
is at its minimum is termed the equilibrium position. Moreover, the motion of each atom is
influenced by its neighboring atoms through these interatomic potentials.

A simplified model of these interactions in a crystal resembles a mass-spring system, as
depicted in fig. 2.2(b). In such a setup, the vibration of a single atom can propagate throughout
the entire system by generating lattice waves. The transmission of sound in a solid occurs due
to these long-wavelength lattice waves. When one side of the solid is heated, atoms near the
hot side exhibit larger vibrational amplitudes. These vibrations are then transmitted to atoms
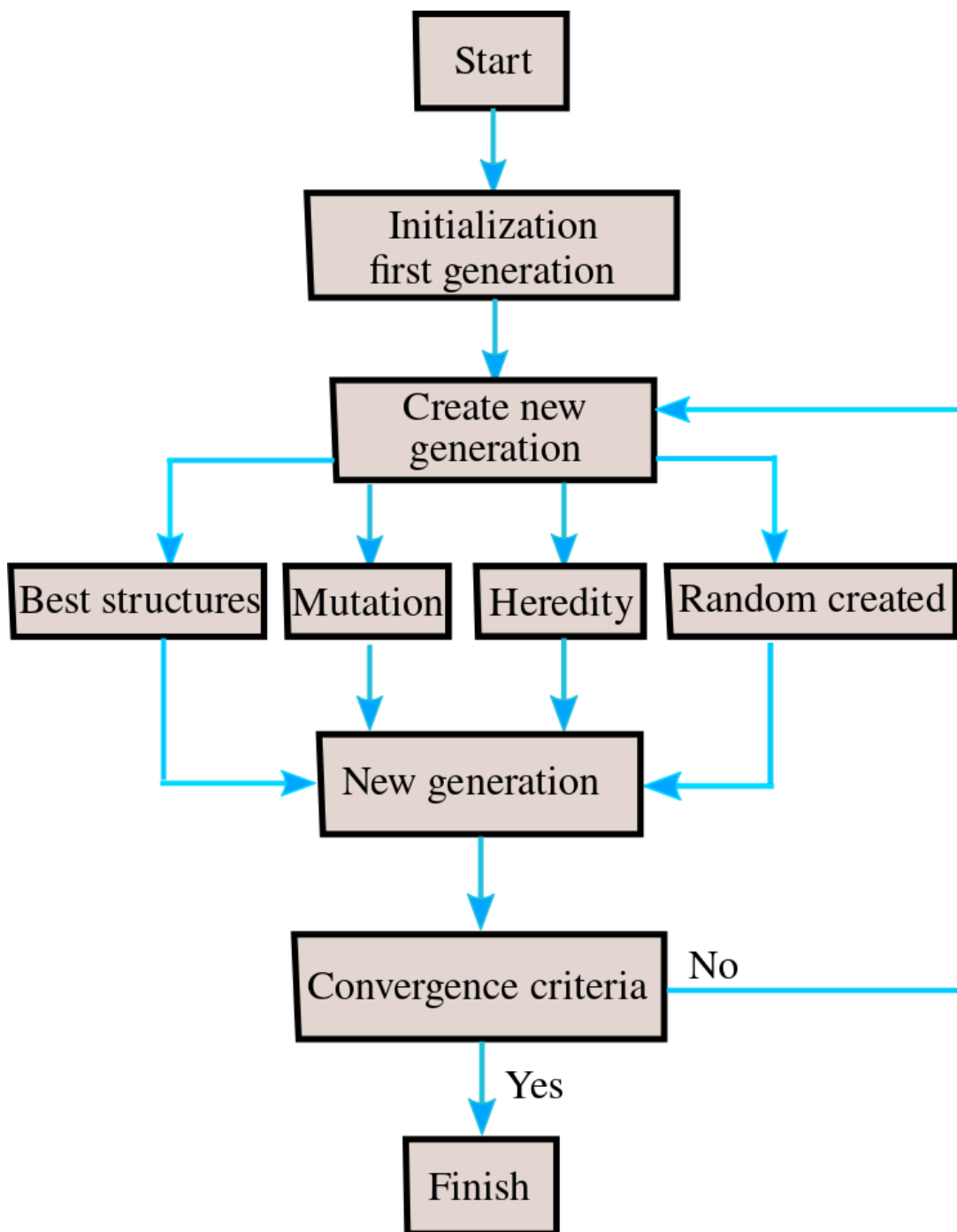
Figure 2.1: Flowchart of USPEX search for low-energy structures
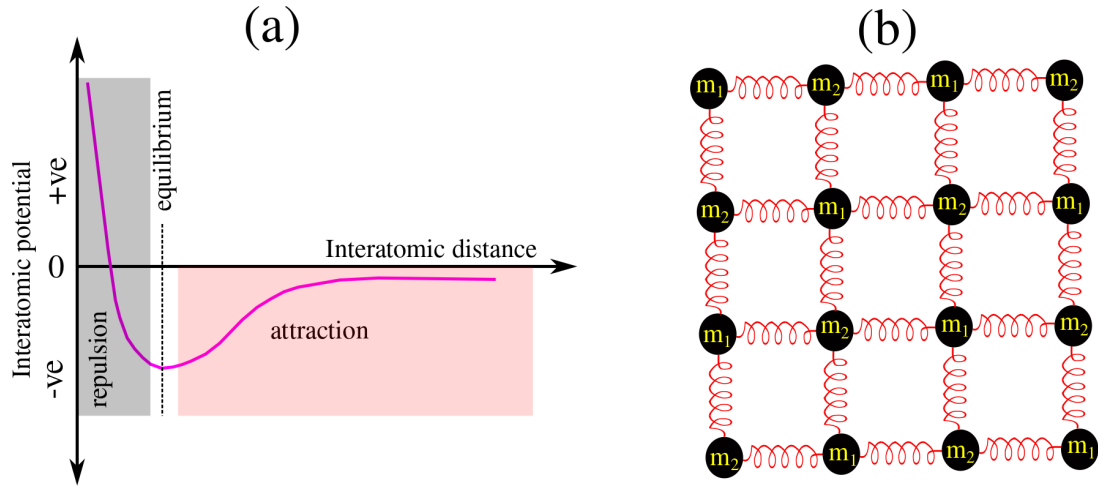
Figure 2.2: (a) Schematic for interatomic potential (b) spring-mass system representing atoms connected in solids [1]

on the opposite side through the propagation and interaction of lattice waves. These lattice waves are referred to as phonons and possess energy given by:

$$E = \hbar \omega \tag{2.37}$$

where ω represents the frequency of the phonon, and $\hbar$ is the reduced Plank constant.

2.9 Thermal conduction in solids

J. Fourier introduced a fundamental concept in heat transfer known as Fourier's law of heat conduction [1], which describes the heat flux ($\vec{Q}$) in response to a temperature gradient (∇T) within a material. The law is mathematically expressed as

$$\vec{Q} = -\kappa \nabla T \tag{2.38}$$

where $\nabla = \frac{\partial}{\partial x}\hat{x} + \frac{\partial}{\partial y}\hat{y} + \frac{\partial}{\partial z}\hat{z}$ represents the gradient operator, and $\hat{x}$, $\hat{y}$, and $\hat{z}$ are unit vectors. Here, $\kappa = \kappa_e + \kappa_l$ denotes the thermal conductivity, which comprises both electronic (κ_e) and lattice (κ_l) thermal conductivity components. This thesis primarily focuses on lattice thermal conductivity, especially in the context of 2D semiconducting materials.

The negative sign in eq. 2.38 indicates the direction of heat flow, moving from regions of high temperature to those of low temperature. While in bulk materials, κ becomes a second-rank tensor, it is crucial to note that Fourier's law, while applicable at a macroscopic level,

faces violations in the domain of 2D materials due to the influence of quantum size effects [39]. Moreover, this law lacks detailed explanations for the intricate microscopic processes governing heat transport. To delve deeper into the mechanisms of heat transfer through lattice vibration, exploring the phonon picture becomes essential.

2.9.1 Boltzmann transport equation BTE

The Boltzmann transport equation (BTE) is a specialized approximation of the general Liouville transport equation, which governs the motion of the N-particle system in the phase space $(r^{(n)}, p^{(n)})$ with distribution function $f^{(N)}(r^{(n)}, p^{(n)})$ [1]. Mathematically, it is represented as:

$$\frac{\partial f^{(N)}}{\partial t} + \sum_{i=1}^{n} \dot{r}^{(i)} \times \frac{\partial f^{(N)}}{\partial r^{(i)}} + \sum_{i=1}^{n} \dot{p}^{(i)} \times \frac{\partial f^{(N)}}{\partial p^{(i)}} = 0 \tag{2.39}$$

with $\dot{p} = \partial p / \partial t$ and $\dot{r} = \partial r / \partial t$.

Solving eq. 2.39 practically is infeasible due to the vast number of variables involved; for instance, one mole of a substance contains 6×10^{23} particles, resulting in an enormous number of variables of $6 \times 6 \times 10^{23}$, which include three variables for space and momentum each. To mitigate this complexity, one approach is to consider a single particle and average over the remaining $N - 1$ particles in the system. This simplification is valid for dilute gases and transforms eq. 2.39 into the form:

$$\frac{\partial f}{\partial t} + \frac{dr}{dt} \cdot \nabla_r f + \frac{dp}{dt} \cdot \nabla_p f = -(\frac{\partial f}{\partial t})_c \tag{2.40}$$

In this equation, the subscripts on ∇ represent the space and momentum gradient operators. The term on the right side of eq. 2.40 accounts for the collision of the single particle under consideration, now external to the $N - 1$ particles. This equation, known as the general Boltzmann transport equation [40–42], finds application in systems with dilute particle densities such as electrons and phonons.

2.9.2 Phonon BTE

In the absence of a temperature gradient, phonons move randomly in all directions within the lattice, and their distribution can be represented by the Bose-Einstein function f_0 as:

$$f_0(\omega_\lambda) = \frac{1}{e^{\frac{\hbar \omega_\lambda}{k_B T}} - 1} \tag{2.41}$$

where k_B is the Boltzmann constant.

When a temperature gradient ∇T is applied to the material, the phonon distribution f_λ deviates from the equilibrium distribution f_0. In the case of phonons, with no external force involved, the third term on the right-hand side of eq. 2.40 is omitted. Furthermore, for steady-state conditions (constant over time), it can be simplified as:

$$\frac{df_\lambda}{dt} = \frac{\partial f_\lambda}{\partial t}\bigg|_d + \frac{\partial f_\lambda}{\partial t}\bigg|_c = 0, \tag{2.42}$$

In this equation, the subscript λ on ω represents both the wavevector q and branch index v of the phonon, i.e., $\lambda \equiv (v, q)$. Eq. 2.42 is the Phonon Boltzmann Transport Equation (PBTE), where the first term is the diffusion term. The name diffusion is due to the fact that in the temperature gradient, heat flows from regions of high to low temperature through a diffusion process. This term can be expressed in a more detailed form as:

$$\frac{\partial f_\lambda}{\partial t}\bigg|_d = -v_\lambda \cdot \frac{\partial f_\lambda}{\partial T} \times \frac{\partial T}{\partial r} = -\nabla T \cdot v_\lambda \frac{\partial f_\lambda}{\partial T}, \tag{2.43}$$

The second term $\partial f_\lambda / \partial t|_c$ in eq. 2.42 encompasses various phonon scattering processes depending on the specific system, including three-phonon scattering, boundary interactions, and impurity scattering.

2.9.3   Solving PBTE

In a more practical form, especially under small temperature gradients, eq. 2.42 can be linearized. The distribution function f_λ of the eq. 2.42 can be expanded to the first order as [2]:

$$f_\lambda = f_0(\omega_\lambda) + g_\lambda, \tag{2.44}$$

in which

$$g_\lambda = -F_\lambda \cdot \nabla T \frac{\partial f_0}{\partial T}, \tag{2.45}$$

where F_λ should be calculated to find g_λ and f_λ from eqs. 2.45 and 2.44. In the case of pure single crystal, where the only source of phonon-phonon scattering exists, F_λ can be expressed as:

$$F_\lambda = \tau_\lambda^0(v_\lambda + \Delta_\lambda), \tag{2.46}$$

where τ_λ^0 represents the single-mode (λ) phonon lifetime computed by first-order perturbation theory, also known as single mode relaxation time approximation (SMRTA). In other words, if $\Delta_\lambda = 0$, eq. 2.46 provides the SMRTA solution for PBTE. The full iterative solution of PBTE calculates τ_λ^0 and Δ_λ using the following relations:

$$\Delta_\lambda = \frac{1}{N} \sum_{\lambda'\lambda''}^{+} \Gamma_{\lambda\lambda'\lambda''}^{+} (\xi_{\lambda\lambda''}F_{\lambda''} - \xi_{\lambda\lambda'}F_{\lambda'})$$

$$+ \frac{1}{N} \sum_{\lambda'\lambda''}^{-} \frac{1}{2}\Gamma_{\lambda\lambda'\lambda''}^{-} (\xi_{\lambda\lambda''}F_{\lambda''} + \xi_{\lambda\lambda'}F_{\lambda'}) \tag{2.47}$$

$$+ \frac{1}{N}\sum_{\lambda'}\Gamma_{\lambda\lambda'}\xi_{\lambda\lambda'}F_{\lambda'},$$

$$\frac{1}{\tau_\lambda^0} = \frac{1}{N} \left(\sum_{\lambda'\lambda''}^{+} \Gamma_{\lambda\lambda'\lambda''}^{+} + \sum_{\lambda'\lambda''}^{-} \frac{1}{2}\Gamma_{\lambda\lambda'\lambda''}^{-} + \sum_{\lambda'}\Gamma_{\lambda\lambda'} \right), \tag{2.48}$$

where $N = N_x + N_y + N_z$ represents the Γ-centered regular q-points grid for discretizing the first Brillouin zone, and $\xi_{\lambda\lambda'} = \omega_{\lambda'}/\omega_\lambda$. The density of the q-point grid must be optimized for each system because the calculated lattice thermal conductivity can vary significantly with different grid spacings. This issue will be discussed in more detail in Chapter 4. The symbols $\Gamma_{\lambda\lambda'\lambda''}^{\pm}$ in eqs. 2.47 and 2.48 denotes the rates of three-phonon scattering processes, given as:

$$\Gamma_{\lambda\lambda'\lambda''}^{+} = \frac{\hbar\pi}{4} \frac{f_0(\omega_{\lambda'}) - f_0(\omega_{\lambda''})}{\omega_\lambda \omega_{\lambda'} \omega_{\lambda''}} \left| V_{\lambda\lambda'\lambda''}^{+} \right|^2 \delta(\omega_\lambda + \omega_{\lambda'} - \omega_{\lambda''}) \tag{2.49}$$

$$\Gamma_{\lambda\lambda'\lambda''}^{-} = \frac{\hbar\pi}{4} \frac{f_0(\omega_{\lambda'}) + f_0(\omega_{\lambda''}) + 1}{\omega_\lambda \omega_{\lambda'} \omega_{\lambda''}} \left| V_{\lambda\lambda'\lambda''}^{-} \right|^2 \delta(\omega_\lambda - \omega_{\lambda'} - \omega_{\lambda''}) \tag{2.50}$$

Eqs. 2.49 and 2.50 describes the absorption and emission processes of three-phonons [41, 43] with modes λ, λ', and λ''. The Dirac delta function δ signifies energy conservation, such as when to phonons with frequencies ω_λ and $\omega_{\lambda'}$ combine into one with frequency $\omega_{\lambda''}$, i.e., $\omega_\lambda + \omega_{\lambda'} = \omega_{\lambda''}$, as shown in fig. 2.3(a). Similarly, in emission process, two phonons with frequencies $\omega_{\lambda'}$ and $\omega_{\lambda''}$ are produced from a single phonon ω_λ, i.e., $\omega_\lambda = \omega_{\lambda'} + \omega_{\lambda''}$, as shown in fig. 2.3(b). Momentum conservation must be followed in these three-phonon inelastic scattering processes, represented as:

$$q'' = q \pm q' + G \tag{2.51}$$

where G is the reciprocal lattice vector. If $G = 0$, then $q'' = q \pm q'$ represents the normal three-phonon process, where the resulting phonon moment stays within the same Brillioun zone, as shown in fig. 2.3(c). However, the three-phonon process with $G \neq 0$ in eq. 2.51, called umklapp process, leads to phonon with momentum extending outside the first BZ. The reciprocal lattice vector G is used to map it back within the first BZ, as shown in in fig. 2.3(d).

In eqs. 2.49 and 2.50, $\Gamma_{\lambda\lambda'\lambda''}^{\pm}$ represents the elements of the scattering matrix, calculated
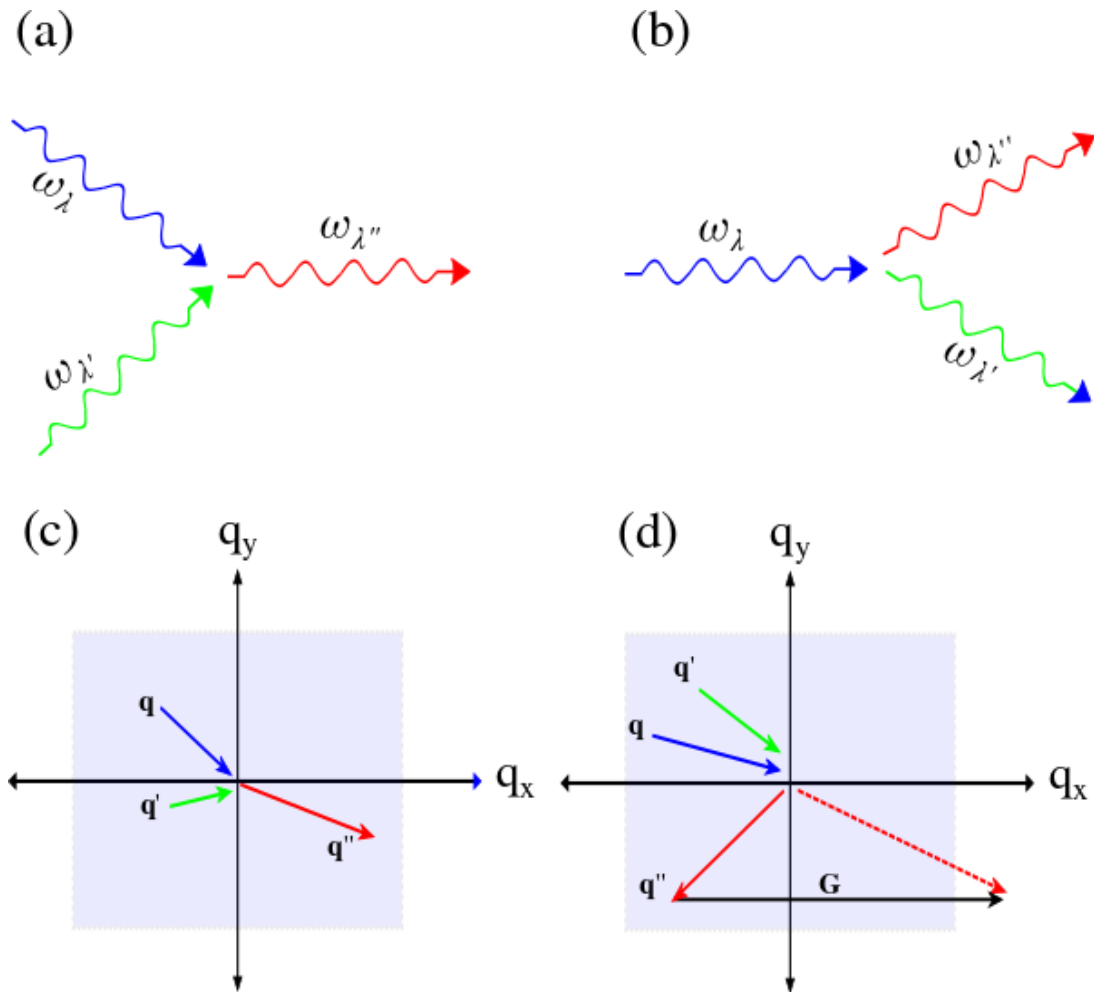
Figure 2.3: The diagram illustrates the processes involved in three-phonon scattering: (a) absorption, (b) emission, (c) normal process, and (d) umklapp process. The shaded regions in (c) and (d) represent the first Brillouin zone, highlighting the fundamental unit in the reciprocal lattice where these processes occur.

from the anharmonic interatomic force constants $\Phi_{ijk}^{\alpha\beta\gamma}$ using the following relation:

$$V_{\lambda\lambda'\lambda''}^{\pm} = \sum_{i\varepsilon \text{u.c}} \sum_{j,k} \sum_{\alpha\beta\gamma} \Phi_{ijk}^{\alpha\beta\gamma} \frac{e_\lambda^\alpha(i)e_{p',\pm q'}^\beta(j)e_{p'',-q'}^\gamma(k)}{\sqrt{M_i M_j M_k}} \tag{2.52}$$

Here (i, j, k) and (α, β, γ) denote atoms and Cartesian coordinates, respectively. The summation of i includes only the unit cell, while (j,k) ranges over the entire system. $e_{p,q}$ represents the normalized eigenfunctions of the phonon involved in the scattering processes (e.g., $e_\lambda^\alpha(i)$ represents the α component of the eigenfunction at the ith atom with mode λ).

The third term in eq. 2.48 accounts for scattering from isotopes disorder present in the material and can be expressed as:

$$\Gamma_{\lambda\lambda'} = \frac{\pi\omega^2}{2} \sum_{i\varepsilon \text{u.c}} g(i) \left| e_\lambda^* \cdot e_{\lambda'}(i) \right|^2 \delta(\omega_\lambda - \omega_{\lambda'}) \tag{2.53}$$

with

$$g(i) = \sum_s f_s(i) \left[1 - \frac{M_s(i)}{\bar{M}(i)} \right]^2 \tag{2.54}$$

In these equations, $M_s(i)$ denotes the mass of isotope s of the ith atom, and $0 < f_s(i) \le 1$ represents its relative frequency of occurrence. $\bar{M} = \sum_s f_s(i)M_s(i)$ is the average atomic mass.

2.9.4   Lattice thermal conductivity

In semiconductors and insulators, most of the heat transfer occurs through lattice vibrations, also known as phonons. The heat flux $\vec{Q}$ due to a temperature gradient ∇T can be analyzed from the perspective of phonons using the following mathematical formulation:

$$\vec{Q} = \sum_s \left[\frac{1}{V} \sum_{q_x} \sum_{q_y} \sum_{q_y} \hbar\omega f_\lambda v_\lambda \right] \tag{2.55}$$

where s denotes the polarization. Eq. 2.55 can be expressed in integral form as:

$$\vec{Q} = \sum_s \int \hbar\omega f_\lambda v_\lambda \frac{dq}{(2\pi)^3} \tag{2.56}$$

Therefore, the lattice thermal conductivity tensor $\kappa_l^{\alpha\beta}$ in the form of F_λ, determined through eq. 2.46, can be written as [2]:

$$\kappa_l^{\alpha\beta} = \frac{1}{k_B T^2 VN} \sum_\lambda f_0(f_0 + 1)(\hbar\omega_\lambda)^2 v_\lambda^\alpha F_\lambda^\beta \tag{2.57}$$
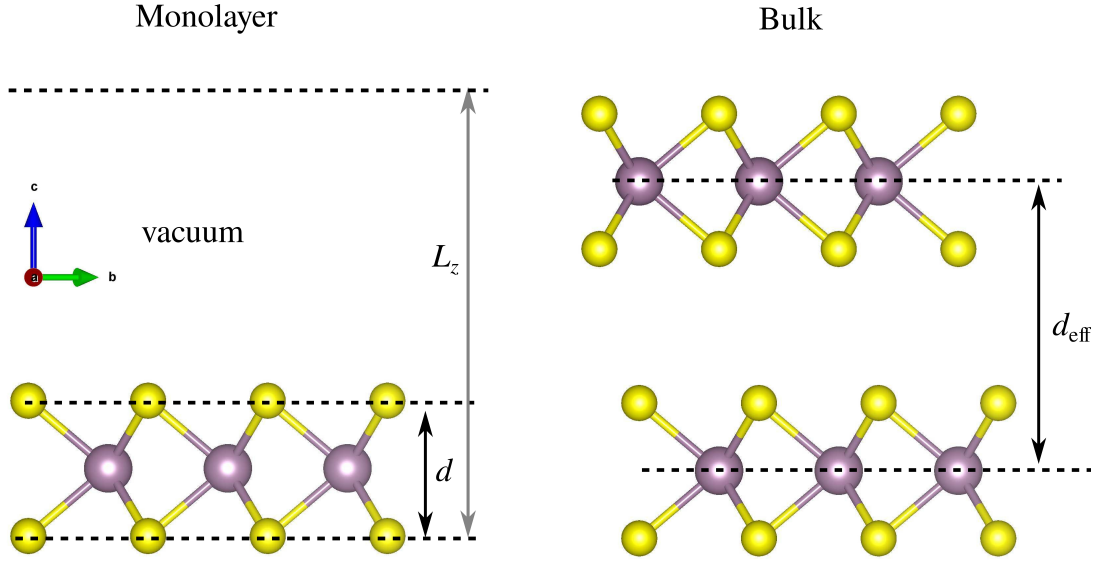
Monolayer   Bulk

Figure 2.4: Illustration of monolayer thickness (d) and effective thickness (d_{eff}).

Here, v_λ^α represents the α component of the group velocity of the λ mode phonon.

In eq. 2.57, V represents the volume of the unit cell. Specifically, for monolayers, which are the primary focus of this thesis, this volume includes the vacuum space usually introduced to prevent interactions between repeated images caused by periodic boundary conditions in DFT calculations. Consequently, the concept of effective thickness d_{eff} is employed to scale the calculated lattice thermal conductivity for 2D materials. It's essential to note that this effective thickness d_{eff} differs from the actual thickness d of the monolayer. In fig 2.4, the thickness is simply the vertical distance between the top and bottom atoms of the monolayer. On the other hand, the effective thickness refers to the vertical distance between the consecutive layers of the corresponding bulk phase.

While alternative methods exist for determining the effective thickness of a monolayer, for example, by adding the Van der Waals radii of the top and bottom atoms to the layer's thickness, our approach involves using the vertical distance between consecutive layers in the out-of-plane direction of the corresponding bulk material as the effective thickness. It's worth mentioning that in some of our predicted 2D materials, we determine the bulk counterpart by removing the vacuum and identifying the most favorable stacking arrangement for the layers after full DFT relaxation.

In this thesis, the ShengBTE code [2, 44] was utilized to calculate lattice thermal conductivity iteratively, finding F_λ with initial values of $F_\lambda^0 = \tau_\lambda^0 v_\lambda$, known as SMRTA values. Within the ShengBTE code, parameters like f_0, ω, and v_λ are computed from harmonic interatomic
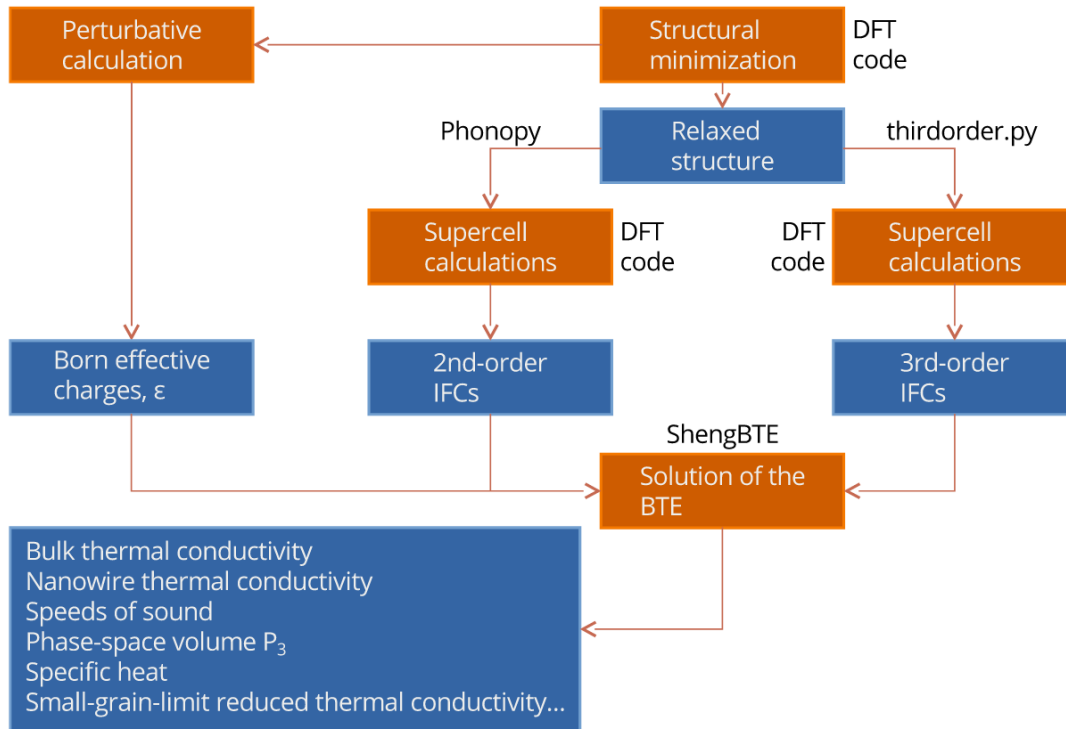
Figure 2.5: Flowchart of lattice thermal conductivity calculation using ShengBTE code [2].

force constants (IFCs), while F_λ, detailed in equations (2.46-2.50), is phonon scattering dependent and employs the anharmonic IFCs.

The computational workflow of the ShengBTE code is outlined in fig. 2.5.

The initial step involves obtaining the optimized structure of the material, a process facilitated by any DFT implemented code. In this thesis, VASP was utilized for this purpose.

The second phase encompasses determining the harmonic properties, achieved through phonopy, as well as the anharmonic properties utilizing the thirdorder.py script. Additionally, Born effective charges and the dielectric constant are computed via density functional perturbation theory (DFPT).

With all these prerequisites in hand, one can proceed to solve the phonon Boltzmann transport equation (PBTE) using the ShengBTE code. This step yields essential information about lattice thermal conductivity and associated processes, including group velocity, phase-space volume for three-phonon scattering, and the Grüneisen parameter (which will be discussed in detail later).

2.10 Inter atomic force constants (IFCs)

Presently, there are two first-principles methods employed to determine the force constants: the linear response method and the finite displacement method. The finite displacement method relies on the concept that when atoms are slightly displaced from their equilibrium positions, the total energy of the structure can be expanded in Taylor's series as follows:

$$E = E_0 + \frac{1}{2!} \sum_{\substack{i,j \\ \alpha,\beta}} \Phi_{ij}^{\alpha\beta} u_i^\alpha u_j^\beta + \frac{1}{3!} \sum_{\substack{i,j,k \\ \alpha,\beta,\gamma}} \Phi_{ijk}^{\alpha\beta\gamma} u_i^\alpha u_j^\beta u_k^\gamma + ..., \tag{2.58}$$

with

$$\Phi_{ij}^{\alpha\beta} = \frac{\partial^2 E}{\partial u_i^\alpha \partial u_j^\beta}, \text{ and } \Phi_{ijk}^{\alpha\beta\gamma} = \frac{\partial^3 E}{\partial u_i^\alpha \partial u_j^\beta \partial u_k^\gamma} \tag{2.59}$$

where E_0 is the total energy of the system at equilibrium position of atoms, displacement of the ith atom along α direction is denoted by u_i^α and the nth order inter atomic force constants (IFCs) by Φ.

2.10.1 Harmonic IFCs

In the context of minor displacements and within the harmonic approximation [45], the motion equation for atom j within the lth unit-cell can be expressed as follows:

$$m_j \frac{\partial^2}{\partial t^2} u_{jl}^\alpha(t) = -\sum_{\substack{j'l' \\ \beta}} \Phi_{jl;j'l'}^{\alpha\beta} u_{j'l'}^\beta(t) \tag{2.60}$$

Here the mass of atom j is denoted by m_j. Applying the Blöch theorem, a plane-wave atomic displacement can serve as the solution for eq. 2.60,

$$u_{jl}(t) = \frac{1}{\sqrt{m_j}} \sum_{q,p} \chi_\lambda e_{j,\lambda} exp\left(i(q.r_{jl} - \omega_\lambda t)\right), \tag{2.61}$$

where, χ_λ represents the transformed coordinate, r_{jl} stands for the equilibrium position vector, and $e_{j,\lambda}$ represents the polarization vector of atom j. It's important to note that λ includes both a polarization and wavevector as before. By utilizing eqs 2.60 and 2.61, the following eigenvalue equation can be derived:

$$\omega_\lambda^2 e_\lambda = D(q)e_\lambda \tag{2.62}$$

where D(q) stands for the dynamical matrix. In the context of an *n*-atom unit cell, D(q) is a Hermitian matrix with dimensions of $3n \times 3n$, and its individual elements can be express as [46]:

$$D(q)^{3(j-1)+\alpha,3(j'-1)+\beta} = \frac{1}{\sqrt{m_j m_{j'}}} \sum_{l'} \Phi^{\alpha\beta}_{j0;j'l'} exp\left(iq \cdot (r_{jl} - r_{j0})\right), \qquad (2.63)$$

In this context, the summation encompasses all unit cells within the system. Additionally, the indices α and β take the values of 1 for the *x*-direction, 2 for the *y*-direction, and 3 for the *z*-direction.

The vibrational frequencies of phonons (denoted as ω_λ) are derived from the square roots of the eigenvalues of the matrix D(q). The corresponding eigenvectors, which have a length of $3 \times n$, represent the polarization vectors of the phonons (also known as phonon mode shapes). These vectors are normalized in such a way that

$$e^T_\lambda \cdot e^\star_\lambda = 1 \qquad (2.64)$$

2.10.2   Anharmonic IFCs

In the harmonic approximation discussed earlier, there is no interaction between different phonon modes [47, 48], leading to infinite phonon lifetime and thus lattice thermal conductivity of the system. This model also fails to explain experimental observations such as thermal expansion [43]. However, including higher-order terms (beyond quadratic) in eq. 2.58 can address these issues. For instance, considering third-order terms in the Taylor series of the potential energy allows for the occurrence of three-phonon scattering processes, explaining these phenomena.

The calculation of three-phonon scattering needed the third-order IFCs as input in eq. 2.52, which is can be calculated using finite difference method [2, 44]:

$$\Phi^{\alpha\beta\gamma}_{ijk} = \frac{\partial^3 E}{\partial u^\alpha_i \partial u^\beta_j \partial u^\gamma_k} \qquad (2.65)$$

Considering the supercell method and Eq. 2.65 the third-order IFCs can be written as:

$$\Phi_{ijk}^{\alpha\beta\gamma} \approx \frac{1}{2h} \left(\frac{\partial^2 E}{\partial u_j^\beta \partial u_k^\gamma} (u_i^\alpha = h) - \frac{\partial^2 E}{\partial u_j^\beta \partial u_k^\gamma} (u_i^\alpha = -h) \right)$$

$$\approx \frac{1}{4h^2} \left(-F_k^\gamma(u_i^\alpha = h, u_j^\beta = h) + F_k^\gamma(u_i^\alpha = h, u_j^\beta = -h) \right. \tag{2.66}$$

$$\left. + F_k^\gamma(u_i^\alpha = -h, u_j^\beta = h) - F_k^\gamma(u_i^\alpha = -h, u_j^\beta = -h) \right)$$

In this context, F_k^λ represents the force experienced by atom k in the direction γ, where atoms i and j are perturbed from their equilibrium positions by a small displacement h along the directions α and β.

Chapter 3

Electronic structures of low-energy two-dimensional Cd$_x$Te$_y$

3.1 Low-dimensional CdTe phases

The optimum and direct band gap of 1.45 eV, high absorption coefficient, easy synthesis processes at low temperatures compared to crystalline silicon (c-Si), and more superior properties of Cadmium Telluride (CdTe) make it an essential material in the thin-film solar cell technology and solar devices based on CdTe are called CdTe photovoltaics (PV) [49]. Recently, CdCl$_2$-activated CdTe-PV has achieved a record laboratory efficiency of 22.2%, reported in Ref. [50], with its underlying mechanism explained by Hatton [51], and has shown the capacity for more improvement than c-Si, whose indirect band gap puts limits on efficiency. Besides these advantages, CdTe-PV has passed through various critical issues like toxicity, low melting point, and scarcity of Te on the earth. Studies related to environmental effects [52, 53] proved that CdTe is a stable material and is not carcinogenic like Cd. The low melting temperature of CdTe (i.e., 1050 °C), which limits its use to domestic appliances, is successfully extended to a higher temperature by encapsulation of molten glass [54]. However, the Tellurium (Te) scarcity in the earth's crust is still a problem of future concern. This issue can be solved to a greater extent by the thickness reduction of CdTe-PV, which will reduce the cost due to low Te consumption and simultaneously meet with the miniaturization of future devices.

The study of CdTe at reduced dimensions attracts more researchers' interest due to its superior properties. For example, Adam [55] synthesized high-quality CdTe nanocrystals (quantum dots and rods) with the one-pot synthesis from the CdO precursor. Further development in this direction was done in experimental work by Ithurria *et al.* [56], in which they prepared nanoplatelets of CdTe as thin as four layers. Recently, the nanorods of CdTe

possessing excellent photon up-conversion (from red to blue), which has potential for applications in photocatalysis and bioimaging, are fabricated [57]. Apart from the nanocrystals (quantum dots, nanorods, nanoplatelets) of CdTe, the progress in the experimental realization of the two-dimensional (2D) form is missing. After the successful exfoliation of graphene [58] and transition metal dichalcogenides [11], researchers thought that syntheses of monolayers are possible only for those materials whose bulk is layered. But the prediction of germanene and silicene [59] compelled the experimentalists to change their thinking. Interestingly, both were grown successfully in the laboratory, followed by more novel methods for preparing 2D materials of non-layered bulk materials like zinc chalcogenides [60], lead sulfide [61], and molybdenum nitride [62]. Therefore, it is possible to synthesize the monolayer CdTe either with existing techniques or minor modifications. In such a scenario, the DFT prediction of novel phases and their properties can be an efficient tool, as in the case of germanene and silicene [59]. Therefore, the DFT predictions for 2D CdTe can provide enough motivation and guidance for experimentalists.

In the line of the DFT study, Wang [63] noted that the freestanding graphene-like structure of monolayer CdTe is unstable and stabilizes when grown on a graphene substrate and possesses the potential for water splitting. Zhou [64] noticed a similar instability in the freestanding hexagonal single-layer structure of CdTe. Interestingly, they revealed that the total energy has an odd/even dependency (i.e., even layers are lower in total energy than an odd number of layers) and have no imaginary frequencies in the phonon spectra of even layers. Surprisingly, CdS is shown to be stable in all respects in the same freestanding hexagonal planar structure with excellent visible photocatalytic properties [65]. This dynamic stability of freestanding honeycomb monolayer CdS is ambiguous because it contradicts the results of other first-principles studies [7, 63]. However, this dynamical instability is removed successfully by applying a 2% biaxial tensile strain [8]. In a DFT study, Iyikanat [10] pointed out that 2D CdTe stabilizes in a primitive cell of 8 atoms with a robust (not affected by the external strain) direct band gap of 1.42eV (GGA) instead of planar and bilayer, which consists of 2 and 4 atoms in their primitive unit cells, respectively. A comparative study [9] of 2D CdTe in different configurations like single-layer (planar and buckled) and bilayer buckled (α-CdTe) has shown the higher stability of the latter one compared with the former. Similar buckled structures for other cadmium chalcogenides (i.e., CdS and CdSe) are confirmed to be stable with excellent water-splitting properties [66].

A natural and worthy question is: how many polymorphs and stoichiometric ratios are possibly stable in the CdTe system? A quick answer to this is: manually, it is hard and sometimes impossible to check all the possible symmetries and stoichiometries in a system. Therefore, to accomplish this goal, various evolutionary algorithms [37, 67–69] are written

by researchers in which USPEX attracts tremendous interest from the condensed matter community due to its high success rate. Hence, in this work, we choose the USPEX to explore a variable compositional-phase diagram of the Cd-Te system. In this study, we benefited from the USPEX to find not only the stable (i.e., energetically most favorable) structures of different compositions but also the metastable phases, which sometimes possess unprecedented properties compared to the stable ones. The resultant structures consist of the buckled bilayer [66] and hexagonal bilayer [64] structures of CdTe, validating our search process, along with the other novel phases of $CdTe_x$ (i.e., $CdTe_2$ and $CdTe_4$). Furthermore, the modulation of electronic properties with thickness and external strain is investigated for consideration in future devices.

3.2   Computational details

To explore the low-energy structures in the variable-compositional phase diagram of Cd_xTe_y (with $x + y \leq 8$), the evolutionary algorithm employed in USPEX [37, 70], coupled with Vienna *Ab Initio* Simulation Package (VASP) [25] for structural relaxation, is used. The projector-augmented wave (PAW) [26] framework is considered for total energy calculations. The generalized gradient approximation (GGA) [19] is adopted to treat the exchange-correlation interactions of electrons. The parameters in the input file of USPEX are; 60 for the total number of generations, 200 structures in the first generation, 80 in the subsequent generations, and the thickness of the 2D layer is allowed to expand up to 4 Å. The search for low-energy structures in all populations is accelerated by considering a coarse Γ-centered k-mesh for Brillouin zone integrations and cutoff energy of 400 eV for plane-wave basis set in structural relaxations. To ensure accuracy, the structures at low-energy facets of the phase diagram are fully relaxed again with a denser k-mesh of spacing $2\pi \times 0.02$ Å^{-1}, higher cutoff energy of 500 eV, force convergence of 0.001 eV/Å, and the energy convergence of 10^{-8} eV. The optimal in-plane lattice constants are obtained from the total energy as a function of the lattice constant, as shown in Fig. 2.1. The calculations of electronic structures are performed on sufficiently high k-mesh of $2\pi \times 0.01$ Å^{-1}, as shown in Fig. 3.2 by convergence test. For the slab model, a vacuum of 23 Å is created in the out-of-plane direction, and the zero damping method of Grimme (DFT-D3) [71] is used for the van der Waals corrections. The phonon band structures are determined using the Phonopy code [72] based on the finite difference method by considering supercells of $3 \times 3 \times 1$ for Cd_4Te and Cd_3Te_2, $5 \times 5 \times 1$, $4 \times 4 \times 1$, $4 \times 7 \times 1$, $3 \times 3 \times 3$ for CdTe, $CdTe_2$, $CdTe_4$, and bulk-CdTe, respectively. The *ab initio* molecular dynamics (AIMD) simulations are performed with the NVT ensemble using the Nosé-Hoover thermostat [73] at a step size of 1 fs and a total time of 10 ps at temperatures of 300, 600, and 900 K. Supercells consisting of

total atoms 80 for Cd_3Te_2, 144 for CdTe, 150 for $CdTe_2$, and 120 for $CdTe_4$ are considered for AIMD simulations. The elastic constants are determined using the finite differences method. The band structures are calculated with both PBE and the Heyd-Scuseria-Ernzerhof hybrid (HSE06) [23] functionals.
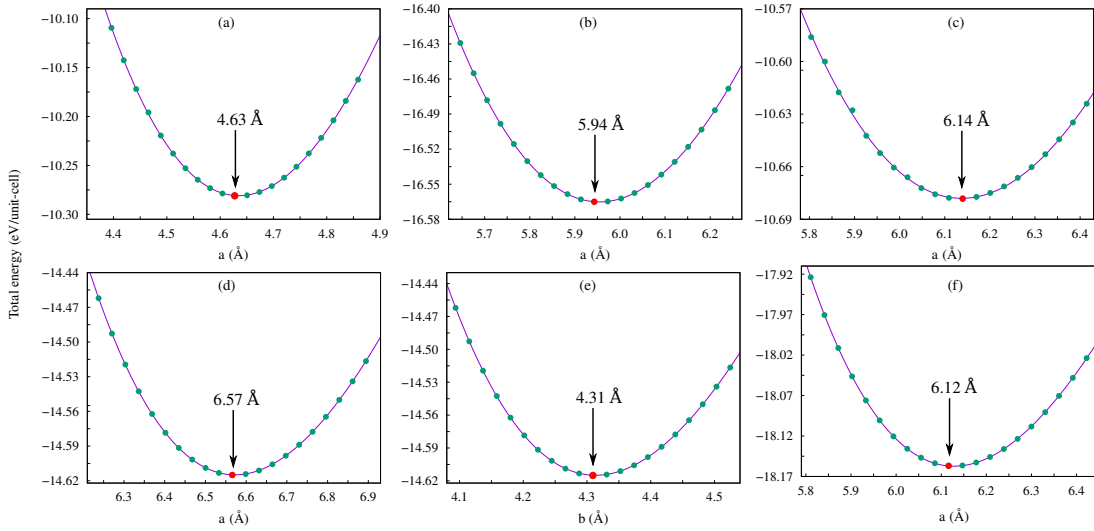
Figure 3.1: Total energy per unit cell as a function of in-plane lattice constants is plotted for (a) CdTe, (b) $CdTe_2$, (c) Cd_3Te_2, (d, e) $CdTe_4$, and (f) Cd_3Te_4 in their two-dimensional configurations. The solid circles represent DFT data, and the line is the fitting of the Murnaghan equation of state. The solid red circle represents the optimum lattice constant in each figure.
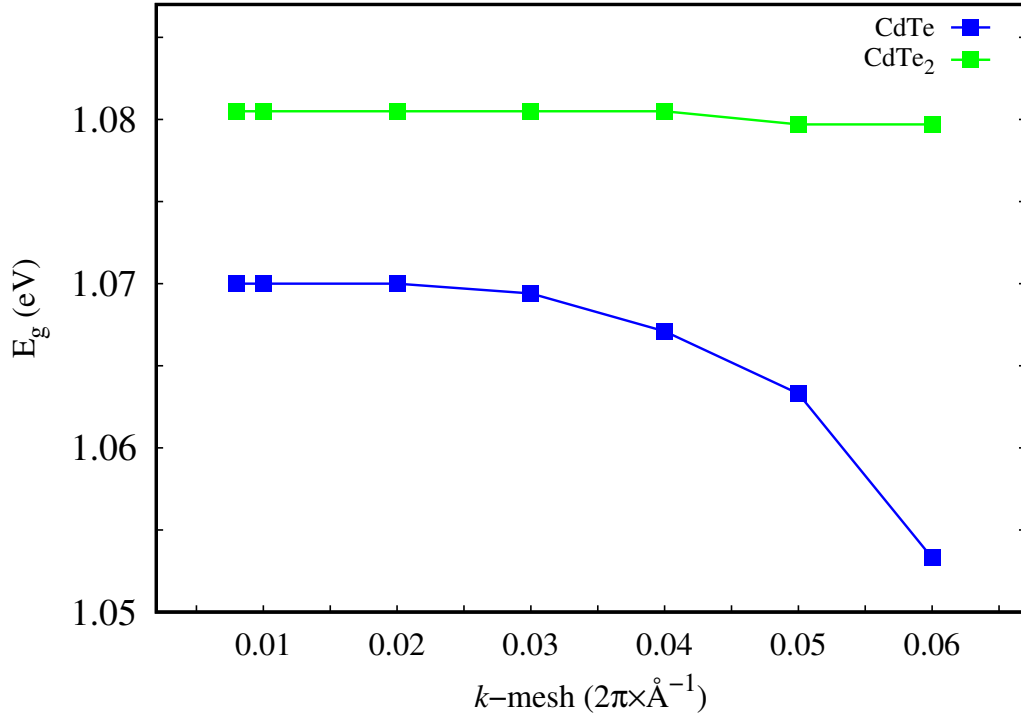
Figure 3.2: This figure shows the convergence of the band gap with increasing k-mesh in the unit $2\pi \times \text{Å}^{-1}$ for 2D CdTe and CdTe$_2$. The 0.01 is the optimum k-mesh, evident from a negligible variation in the band gap beyond it.

3.3 Results and discussion

3.3.1 Structure prediction

Enthalpy H, the approximate Gibbs free energy at 0 K of a system, is defined as; $H = U + PV$ with U, P, and V representing the internal energy, pressure, and volume, respectively. The thermodynamic stability of any system against its constituents depends on their formation of enthalpies $\triangle H$. Specifically for 2D Cd$_x$Te$_y$, $\triangle H$ is given as $\triangle H = H_{\text{Cd}_x\text{Te}_y} - xH_{\text{Cd}} - yH_{\text{Te}}$, where H_{Cd} and H_{Te} are the enthalpies of the lowest possible 2D configurations of elemental cadmium and tellurium as shown in Figs. 2.1(a, e). Fig. 2.1(c) depicts the normalized $\triangle H$ (in eV/atom) for various compositions and polymorphs of the 2D Cd$_x$Te$_y$ system at zero temperature and pressure. Conceptually, all the structures with positive ΔH means located above the

line connecting elemental 2D Cd and Te are unstable. While those structures having negative $\triangle H$ can either be stable or metastable [34] against Cd and Te. In this regard, numerous polymorphs of different stoichiometric ratios have negative $\triangle H$, but here we consider the lowest energy ones only. In Fig. 2.1(c), they are indicated with colors (solid circles) like magenta, red, dark blue, cyan, gray, black, yellow, and gold for Cd, Cd_4Te, Cd_3Te_2, CdTe, Cd_3Te_4, $CdTe_2$, $CdTe_4$, and Te, respectively. The 2D CdTe is located at the global minimum of the convex hull and has the same structure as predicted previously in the DFT study [9]. Further analysis found its buckled polymorph [64] at 41 meV/atom above the ground state. These positions of different polymorphs on the convex hull show their relative thermodynamic stability, which plays a crucial role in their experimental viability. The lowest energy structure of $CdTe_2$ [See Fig. 2.1(d)] is marginally stable as it occupies the position of 6 meV/atom above the convex hull. This observation contradicts the results in a recent report [74], showing it on the convex hull, which might result from their consideration of the insufficient number of structures and generations in the search process. The search for low-energy phases of variable composition strongly depends on the population size, especially in the first generation. Therefore, we consider 200 structures in the first generation and 80 in the subsequent generations. Sometimes the study of metastable structures has tremendous importance because of their superior properties and synthesis feasibility, such as optimization of the growth conditions or destabilizing the stable phases by charge transfer like in the case of TMDCs [75, 76]. The 2D metastable structures of $CdTe_4$, Cd_3Te_4, Cd_4Te, and Cd_3Te_2 are respectively 48, 62, 68, and 79 in units meV/atom above the convex hull (See Fig. 3.4 for details).

(a) Cd_3Te_2 (*P321*) (b) Cd_3Te_4 (*Cmm2*) (c) $CdTe_4$ (*Cm*) (d) Cd_4Te (*P1*)

$a_1 = a_2 = 6.12$, $\gamma = 120°$ $a_1 = a_2 = 6.14$, $\gamma = 93.2°$ $a_1 = 6.57$, $a_2 = 4.31$, $\gamma = 109.2°$ $a_1 = 4.98$, $a_2 = 5.03$, $\gamma = 118.5°$
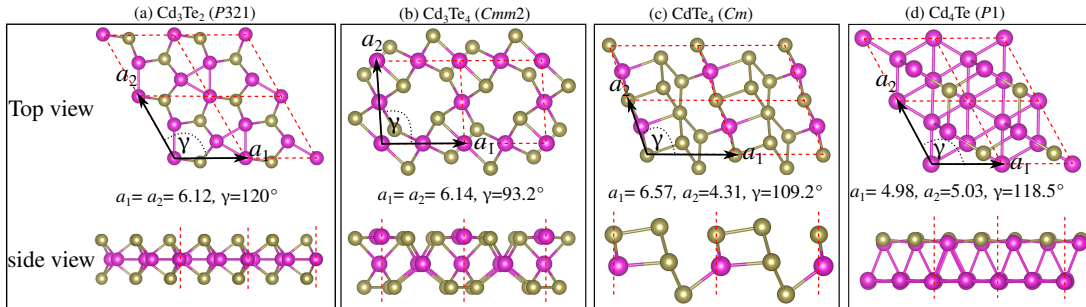
Figure 3.4: Top and side views of the 2D structures predicted by USPEX in this work, i.e., (a) Cd_3Te_2, (b) Cd_3Te_4, (c) $CdTe_4$, and (d) Cd_4Te. The (red) dashed lines represent the unit cell in each case.
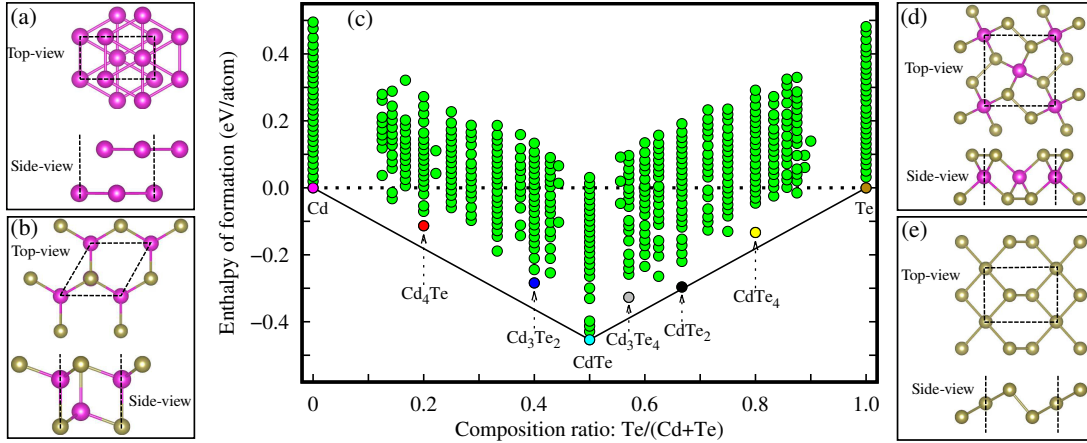
Figure 3.3: The top and side views of structures of compositions lying on the convex hull for (a) elemental 2D cadmium, (b) 2D CdTe, (d) 2D $CdTe_2$, and (e) elemental 2D tellurium, with the dash lines showing the unit cell in each case. (c) The formation of enthalpies for all 2D binary structures from the evolutionary search of USPEX with various stoichiometries between Cd (magenta) and Te (gold color), whereas those occupying the lowest energy facets, are indicated with different colors: i.e., Cd_4Te (red), Cd_3Te_2 (dark blue), CdTe (cyan), Cd_3Te_4 (gray), $CdTe_2$ (black), and $CdTe_4$ (yellow).

3.3.2 Stability screening

In the previous section, we screened the energetically most favorable structures of various compositions in the Cd_xTe_y system. These structures can be strong candidates for experimentally accessible phases if they pass successfully through state-of-art filters of dynamical, thermal, and mechanical stabilities [77].

3.3.2.1 Phonon

Figs. 3.5(b, c) show the phonon dispersion spectra of the energetically most favorable monolayers CdTe and $CdTe_2$, respectively. Additionally, Fig. 3.5(a) depicts the phonon band structure of the bulk CdTe (wurtzite structure, space group $P6_3mc$). Phonon band structures of some of the low-energy Cd_xTe_y are shown in Fig. 3.6. The absence of imaginary frequencies in the phonon spectra, except for Cd_4Te in Fig. 3.6(d), confirms their dynamical stabilities. A common observation from phonon spectra of all these structures is that the highest frequencies are lower than 6 THz due to the heavy masses of Cd and Te atoms. The gap in the optical branch that divides it into low and high energy areas is 0.9 and 0.41 in the unit of THz for monolayer CdTe and $CdTe_2$, respectively. The overlap between low-energy optical and acoustic phonon branches results in high acoustic-optical interaction near the Brillouin zone
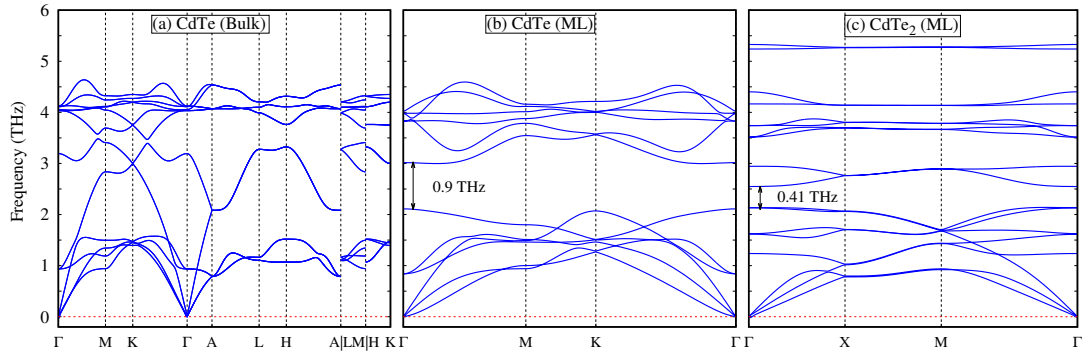
Figure 3.5: Phonon dispersion curves for (a) bulk CdTe, (b) monolayer CdTe, and (c) monolayer $CdTe_2$ along the high symmetry k points in the first Brillouin zones.

center in CdTe and along the X-M path in monolayer $CdTe_2$, which makes them potential thermoelectric materials [78].
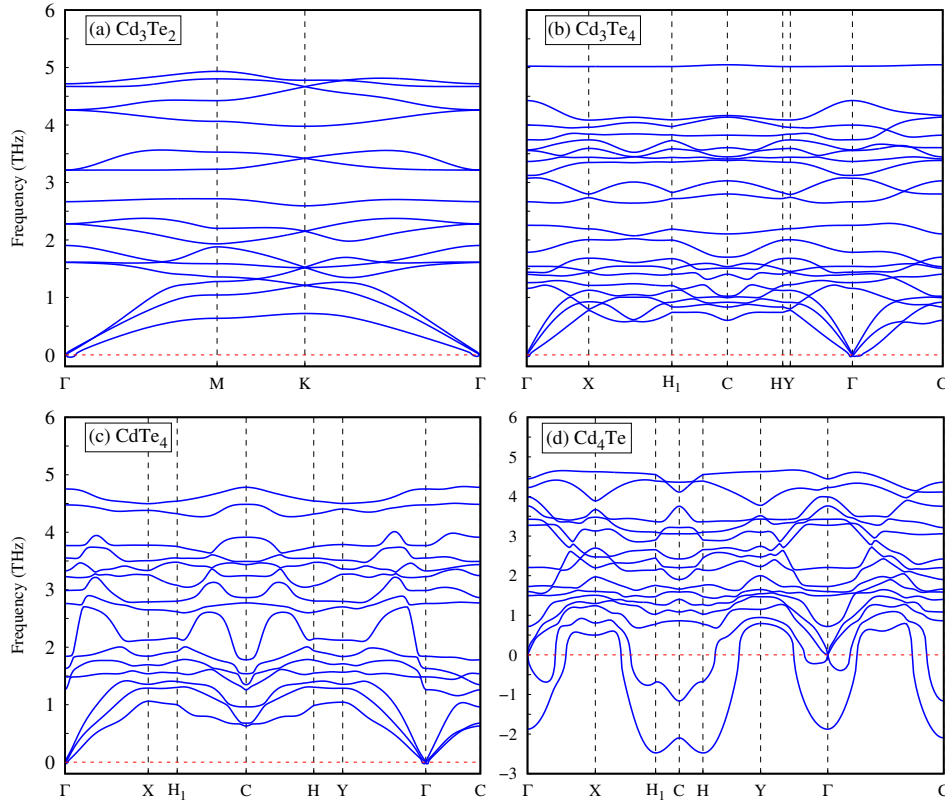
Figure 3.6: Phonon band structures in the first Brillouin zone of single-layer (a) Cd_3Te_2, (b) Cd_3Te_4, (c) $CdTe_4$, and (d) Cd_4Te. The presence of negative frequencies in phonon spectra of single-layer Cd_4Te shows its dynamical instability.

3.3.2.2 *Ab initio* molecular dynamics

Fig. 3.7(a, b) shows the AIMD simulation results at 300 K for monolayers CdTe and $CdTe_2$, respectively. The system's total energy rises initially and then oscillates about its average value in eV/unit-cell of nearly -9.75 for CdTe and -16.0 for $CdTe_2$. The absence of any sharp drop or rise in the total energy shows their thermodynamic stability at 300 K. Similarly, the temperature of the systems oscillates about 300 K, the input temperature for AIMD simulations. The structures of monolayer CdTe and $CdTe_2$, after a time of 10 ps of AIMD simulations, are shown as insets in Figs. 3.7(a, b). It depicts that although the atoms of the lattice are oscillating about their equilibrium positions but resulting in no bond breaking or phase transformations that confirm their thermodynamic stability. Further, we perform AIMD calculations at 600 and 900 K to check thermodynamic stability at higher temperatures. The results shown in Fig.

3.8 indicate the stability of monolayer CdTe at 600 and 900 K, while $CdTe_2$ is unstable at 900 K, evident from the broken bonds in the inset of Fig. 3.8(d). For other predicted meta-stable structures, i.e., Cd_3Te_2 and $CdTe_4$, the results are shown in Fig. 3.9. Both structures show thermodynamic stability at 300 K, as evident from the absence of any broken bonds and drop in energy and temperature profiles. At 600 K, however, Fig. 3.9(d) shows broken bonds in the final structure. Thus the monolayer $CdTe_4$ is thermodynamically unstable at 600 K.
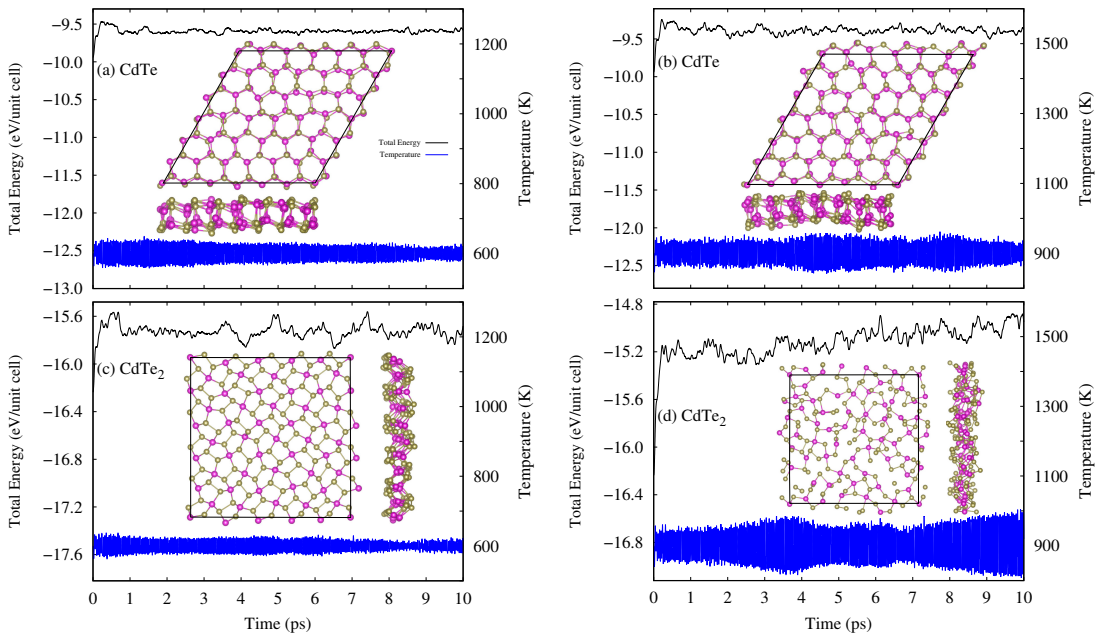
Figure 3.8: Total energy per unit cell and temperature profiles using *ab initio* molecular dynamics simulations at temperature of (a) 600 K, (b) 900 K for monolayer CdTe and (c) 600K, (d) 900 K for $CdTe_2$. The inset in each case shows the final structure from top and side views after 10 ps.
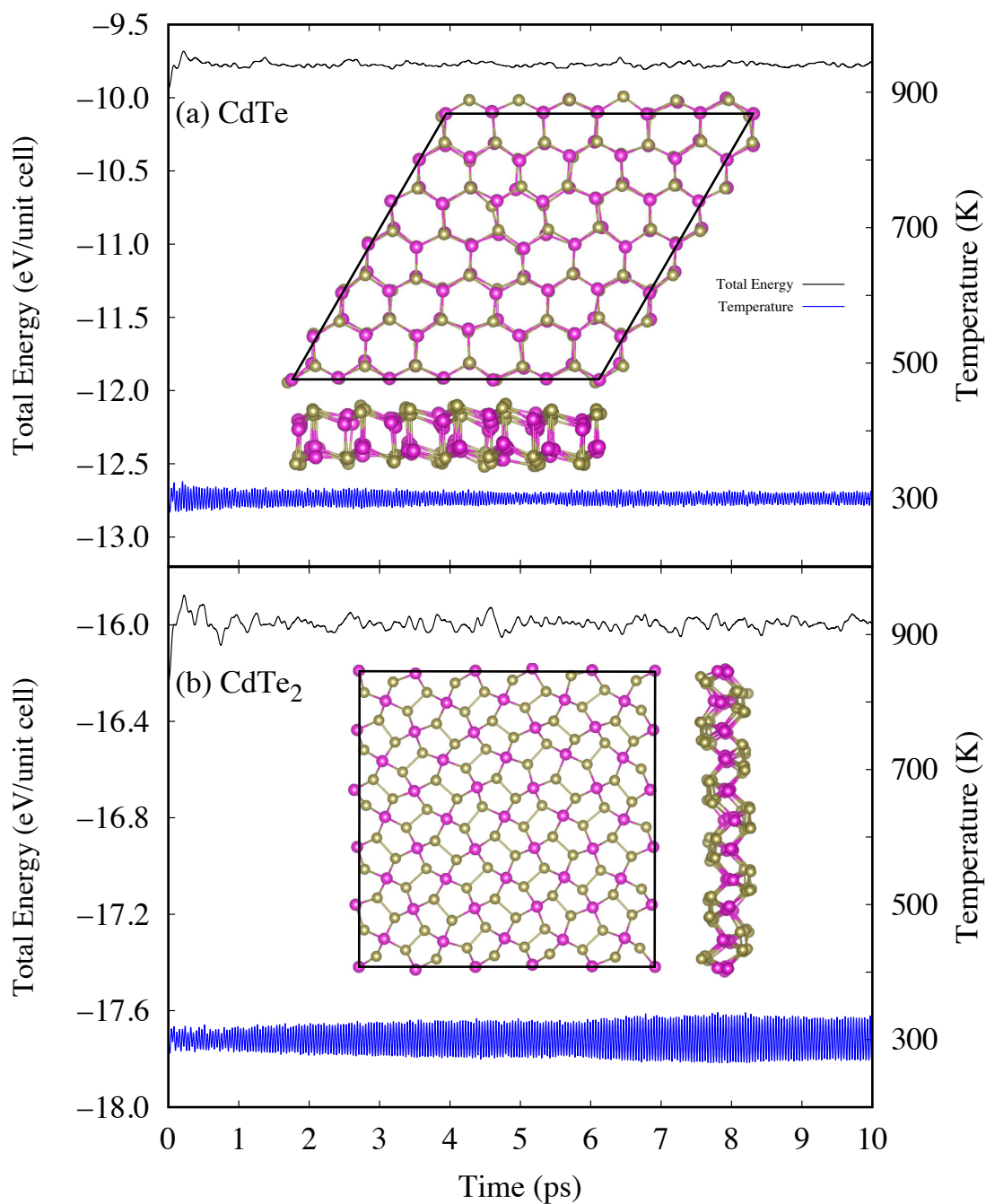
Figure 3.7: Total energy per unit cell and temperature profiles using AIMD simulations at 300 K for monolayer (a) CdTe and (b) CdTe$_2$. The insets show the top and side views of the simulated structures after 10 ps.
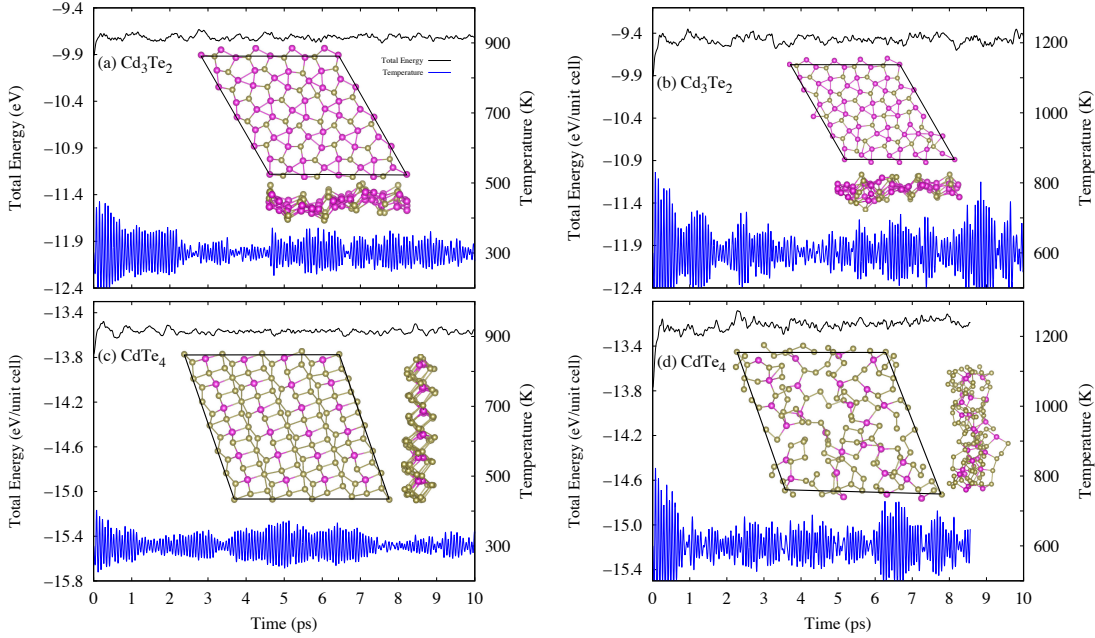
Figure 3.9: Total energy per unit cell and temperature profiles using *ab initio* molecular dynamics simulations at temperatures of (a, b) 300 K and 600 K for Cd_3Te_2 and (c, d) 300 K and 600 K for monolayer $CdTe_4$, respectively. The inset in each case shows the final structure (supercells of $4 \times 4 \times 1$ for Cd_3Te_2 and $4 \times 6 \times 1$ for $CdTe_4$) after 10 ps. In the case of $CdTe_4$ at 600 K, the AIMD calculations diverge.

3.3.2.3   Elastic constants

To confirm the elastic stability of all low-energy Cd_xTe_y structures, their elastic constants are determined and tabulated in Table 3.1. The elastic stability criteria for 2D structures are given in Ref. [79]. Trigonal structures of monolayer CdTe and Cd_3Te_2 satisfy the elastic stability criteria $C_{11} > 0$, $C_{66} > 0$, and $C_{11} > |C_{12}|$. The squared structure monolayer $CdTe_2$ satisfies the elastic stability criteria $C_{11} > 0$, $C_{66} > 0$, and $C_{11} \times C_{22} > C_{12}^2$. Similarly, monolayer Cd_3Te_4 and $CdTe_4$ with oblique structures satisfy the elastic stability criteria $C_{11} > 0$, $C_{11} \times C_{22} > C_{12}^2$, and $det \, |C_{ij}| > 0$; with $i, j = 1, 2, 6$. Hence, all the structures in Table 3.1 are mechanically stable.

3.3.3   Structural analyses

The lowest energy monolayer CdTe has a trigonal structure with space group $P\bar{3}m1$, as shown in Fig. 3.10(a). Its side view shows the two-layer configuration. To avoid confusion with

Table 3.1: Lattice parameters and elastic constants of low-energy Cd_xTe_y structures

Composition	Lattice parameters			Elastic constants (N/m)					
	a (Å)	b (Å)	γ	C_{11}	C_{22}	C_{12}	C_{66}	C_{16}	C_{26}
CdTe	4.63	4.63	120°	38.28	38.28	16.44	10.92	...	...
$CdTe_2$	5.94	5.94	90°	16.83	16.89	4.12	5.30	...	...
Cd_3Te_2	6.14	6.14	120°	11.58	11.47	−1.24	6.42	...	...
$CdTe_4$	6.57	4.31	109.15°	24.43	23.07	4.98	8.89	−3.72	3.17
Cd_3Te_4	6.12	6.12	93.21°	19.71	19.69	11.32	15.72	−4.67	−4.72

bilayers in the later section, we name them upper and lower sublayers. These sublayers have AB stacking, where each Te atom in the upper sublayer is located right on top of the Cd atom in the lower sublayer. Its bulk counterpart, shown in Fig. 3.12(a), is a stable hexagonal structure (space group $P6_3mc$) with $a = b = 4.61$ Å and $c = 7.57$ Å agrees well with experimental values $a = b = 4.57$ Å and $c = 7.47$ Å [80]. For a better comparison between bulk and 2D structures of CdTe, we show them together in Fig. 3.12(a,b). The in-plane lattice constant expands by 0.016 Å in 2D compared to the bulk. The out-of-plane Te-Cd-Te bond angle ϕ is 109.73°, and the in-plane angle θ is 109.21°. The former increases to 109.98° while the latter decreases to 108.96° in the 2D CdTe. There are two types of Cd-Te bonds in 2D CdTe [see Table 3.2], with the in-plane distance shorter by 0.223 Å compared to the out-of-plane, while in the corresponding bulk structure, this difference is as smaller as 0.004 Å. The buckling height denoted by h in Fig. 3.10(a) has a value of 0.97 Å and is slightly larger than 0.95 Å as of bulk. The Te atoms of the upper sublayer in 2D CdTe buckle upward in contrast to the bulk structure, where they buckle downward relative to the Cd atoms. As a result, the Cd atom of the upper sublayer comes closer to the Te of the lower sublayer to make a bond of the same length of 3.07 Å as the Cd atom of the lower sublayer with the Te of the upper sublayer. Thus in the 2D CdTe structure, each Cd and Te complete their four coordinations by making bonds with the four Te/Cd atoms in which three belong to the same (001) plane and the fourth one to the upper/lower sublayer, alternatively [see Fig. 3.12(a,b) for details]. The completion of four coordinations of Cd in 2D CdTe is crucial for its stability because it is otherwise unstable in the single layer (planar and buckled), where Cd cannot complete its fourth coordination [10, 63].

Fig. 3.10(b) shows the top view of the primitive unit cell of squared 2D $CdTe_2$ with space group $P\bar{4}2_1m$ which further consists of wrinkled pentagons of unequal side lengths. The side-view shows that 2D $CdTe_2$ consists of three constituent sublayers: the Cd sublayer sandwiches between two Te sublayers with a buckling height of 1.79 Å. The Te-Cd-Te bond angle in the in-plane is 102.06° and in the out-of-plane is 113.28°. 2D CdS_2 has a similar structure, recently reported in an article [66]. Each Cd atom makes four bonds with neighboring Te atoms: two

with each Te sublayer. However, Te makes three bonds: two with Cd atoms and one with the Te atom. This atomic configuration is different than the one cleaved from its bulk. Fig. 3.13 compares the bulk-cleaved and our predicted 2D structures of $CdTe_2$. Bulk $CdTe_2$ has a cubic structure (space group $Pa\bar{3}$) with $a = 7.19$ Å which is in good agreement with the previous report [81] see Fig. 3.13(a). The cleaved monolayer $CdTe_2$ shown in Fig. 3.13(b) has a structure similar to that of monolayer $PdSe_2$ [82], which is dynamically unstable. The side-views of Fig. 3.13(b, c) depict the difference in the Te arrangement of cleaved and our predicted 2D $CdTe_2$; the Te-Te bond formed between upper and lower sublayers in the cleaved monolayer but in the same sublayer in our case.

In addition to the crystal structures, the electron localization function (ELF) mapped in (001) and (100) planes are shown in Fig. 3.10(a, b) for bond analysis of the 2D CdTe and $CdTe_2$, respectively. The ELF of CdTe shows electrons localization around the Te atoms which means that the electrons transfer from Cd to Te to make a predominant ionic Cd-Te bond. Because in a covalent bond, electrons localize in the midway regions of the bonded atoms. The Bader charge analysis of 2D CdTe, given in Table 3.2, supports the ionic-dominant character of the Cd-Te bond. The lower electronegative Cd atom donates 0.5 electronic charges to the higher electronegative Te atoms. Similarly, the Cd-Te bond of 2D $CdTe_2$ has a predominant ionic character because electrons localize on Te atoms, as shown by ELF plots. However, the Te-Te bond of either the upper or lower sublayer is covalent-dominant because electrons localize comparatively in the middle region of the Te-Te bond, which is evident from the ELF plot in the (100) plane. Also, the Bader charge analysis of $CdTe_2$ shows that 0.45 electronic charge transfers from the Cd atom to the four Te atoms. The covalent character of the Te-Te bond might be the reason for the stability of structures with an excess ratio of Te atoms (i.e., $CdTe_2$ and $CdTe_4$).

We consider the AA stacking configuration for the bilayer CdTe similar to its bulk counterpart. However, for 2D $CdTe_2$, the bulk analog does not exist or has a different crystal structure. The different crystal structures of monolayers and the corresponding bulk analogs are noted previously in other materials like borophene [83], 1T phase of MoS_2 [84], and 2D-SiS [85]. Therefore, various stackings for bilayer $CdTe_2$ are possible. We show three configurations called AA, AB, and AB′ stackings in Fig. 3.11. In AA stacking, the top layer is the replica of the bottom layer. The AB stacking is obtained by rotating the top layer of AA stacking by 180° about the y-axis. Finally, the AB′ stacking is obtained by translating the top layer of AB stacking along the x-direction by $a/2$, where a is the lattice constant of 2D $CdTe_2$. The separation distance in AA stacking is shorter than AB and AB′ due to the intervention between the lower Te-sublayer of the top layer and the upper Te-sublayer of the bottom layer. The repulsion between nearest Te-atoms in AB stacking increases the separation distance. As
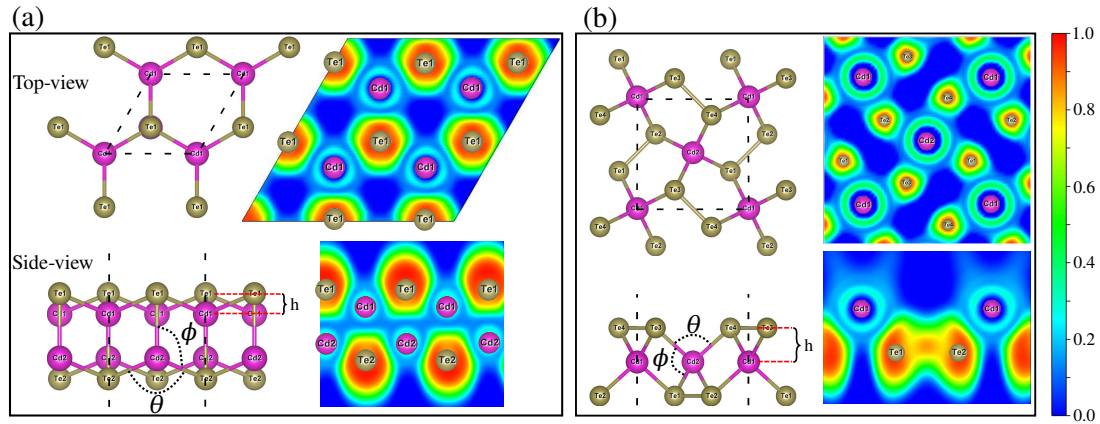
Figure 3.10: The top and side view of the 2D structures (dashed lines indicate primitive unit cell) along with their electron localization function (ELF) maps (in the plane of Cd and Te atoms) for (a) CdTe and (b) $CdTe_2$. The buckling height is denoted by h. The multicolor bar (left side) scales the value of ELF, where zero value (blue) means no localized electrons while one value (red) corresponds to completely localized electrons.

a result, the total energy of the system rises. However, in the AB$'$ configuration, the nearest Te-atoms of the top and bottom layers displace in the (001) plan and decrease the separation distance and the system's total energy. Thus, the AB$'$ configuration is the most favorable and will be considered in further study.

The primitive unit cell of 2D Cd_3Te_2 has a hexagonal structure with $a = b = 6.11$ Å and γ of 120°, where the Cd atomic layer is sandwiched by the Te atoms. Each Cd makes four bonds, two with other Cd in the same ab plane and two with the Te atoms (one from above and another from below) [see Fig. 3.4(b) for more details]. The Cd-Te bond in Cd_3Te_2 has an ionic character, while the Cd-Cd bond has a covalent character as the electrons localized in the central region of the bond [see Fig. 3.14(a)]. As a general trend, with the increase of Te ratio in the Cd_xTe_y system, Te atoms tend to shear their electron and result in meta-stable structures such as $CdTe_4$, whose lattice parameters and Bader charge analysis are respectively given in the Tables. 3.1 and 3.2, and the electron localization function is plotted in Fig. 3.14.

(a) AA   (b) AB   (c) AB′

-2.609 eV/atom   -2.601 eV/atom   -2.801 eV/atom

4.937   7.872   6.488
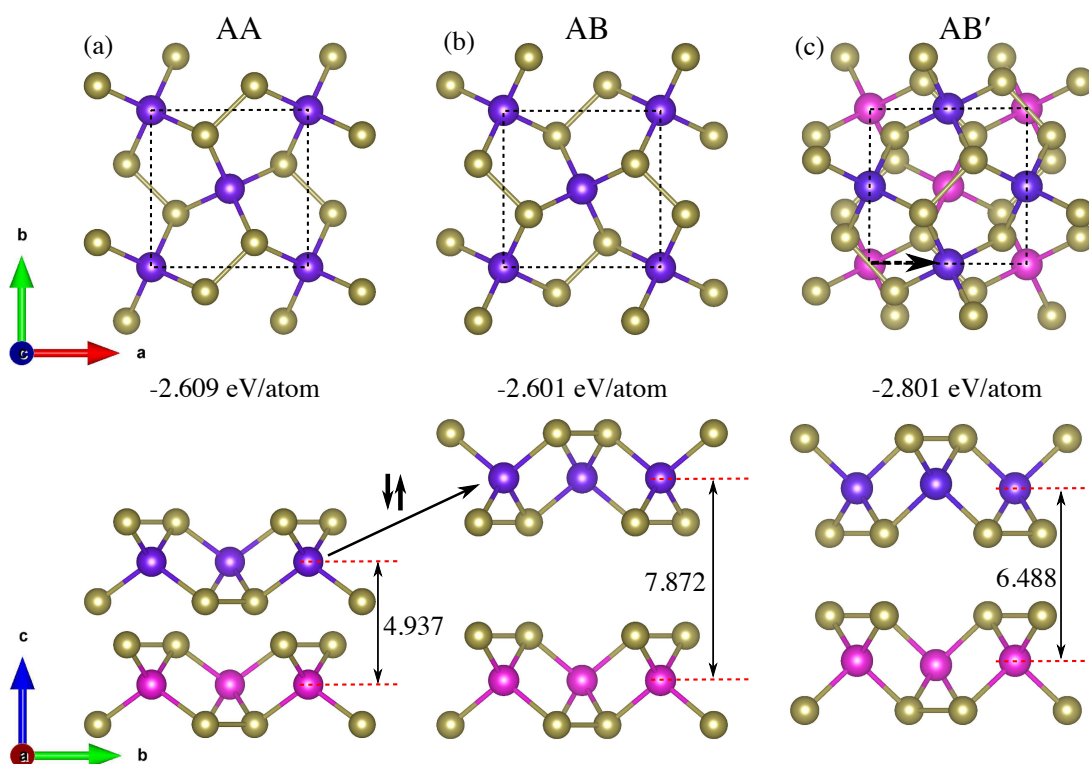
Figure 3.11: Three configurations of bilayer 2D CdTe$_2$ stacking are (a) AA stacking, (b) AB stacking, and (c) AB′ stacking. The symbol ↑↓ represents the upside-down rotation of the top layer in (a) relative to the bottom layer. The horizontal arrow in (c) denotes the $a/2$ shift of the top layer of (b) along the x-direction relative to the bottom layer. The calculated total energy per atom for each configuration is listed. After relaxations, the separation distances between Cd sublayers of the top and bottom layer along the z-direction are shown. The magenta and blue spheres represent the Cd atom of the bottom and top layers, whereas the gold color denotes the Te atom.

Table 3.2: This table shows the bond lengths and Bader charges on all atoms in the predicted stable monolayers. The positive and negative values of Bader charges show the gain and loss of electrons, e.g., -0.5/+0.5 for Cd/Te in CdTe implies that 0.5 electrons have transferred from Cd to Te. The vertical/horizontal double-headed arrows ($\updownarrow$ / $\leftrightarrow$) denote the out-of/in-plane bond lengths, respectively.

Composition	Bond length (Å)		Bader charges ($\lvert e \rvert$)					
	d_{Cd-Te}	d_{Te-Te}	Cd1	Cd2	Te1	Te2	Te3	Te4
CdTe	2.843 $\leftrightarrow$ 3.066 $\updownarrow$	...	−0.5	−0.5	0.5	0.5	...	...
CdTe$_2$	2.855	2.770	−0.45	−0.45	0.18	0.27	0.23	0.22
Cd$_3$Te$_2$	2.817	...	−0.31	−0.33	0.49	0.49	...	...
CdTe$_4$	3.068 $\leftrightarrow$ 2.884 $\updownarrow$	2.810	−0.47	...	0.27	−0.13	0.22	0.11
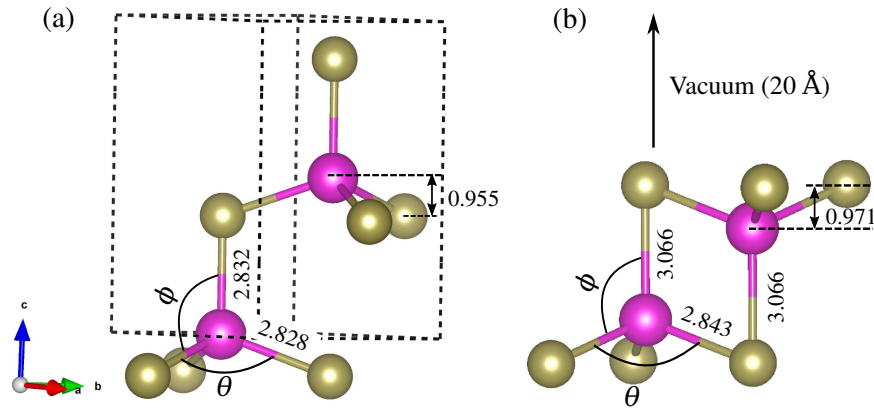
Figure 3.12: (a) The structure of Bulk CdTe in the wurtzite phase, where the dashed box outlines the primitive unit-cell. (b) The structure of the predicted 2D layer of CdTe by USPEX in this work. The magnitudes of bond lengths and buckling heights are in Å.
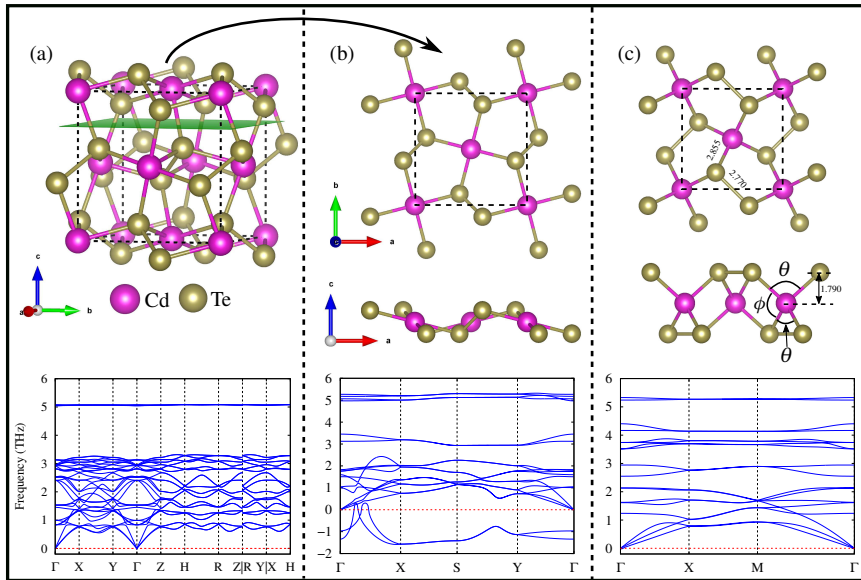
Figure 3.13: (a) The energetically favorable bulk structure of CdTe$_2$ and its dynamical stability is shown by its phonon spectra. The cleavage plane (001) is indicated by the green color. (b) The top and side views of exfoliated monolayer from the bulk CdTe$_2$, where the negative frequencies in its phonon spectra show the dynamic instability. (c) The top and side views of the stable monolayer CdTe$_2$ predicted in this work. The dashed box in (a) and squares in (b and c) outline the primitive unit cells.
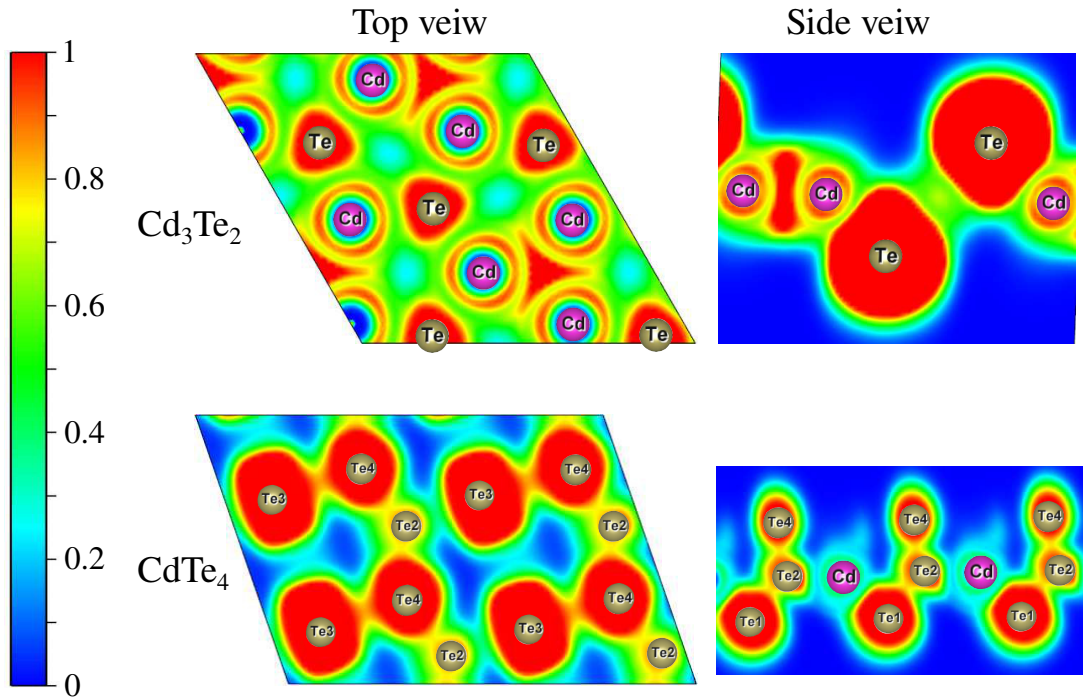
Figure 3.14: This figure shows the electron localization function (ELF) in crystal planes (001) and (100) of single-layer Cd_3Te_2 and $CdTe_4$. The multi-color bar (left side) scales the value of ELF, where zero and one value correspond to no localization and complete localization of electrons, respectively.

3.3.4 Electronic structure

Fig. 3.15(a) depicts the electronic structure (i.e., band structure and atom-projected density of states) of CdTe in its single layer (SL), bilayer (BL), trilayer (TL), and bulk configurations. For an accurate determination of the band gap, the band structure calculated using hybrid functional (HSE06) is also shown as PBE functional underestimates it. Contrary to transition metal dichalcogenides (TMDCs), which switch from the direct to indirect band gap when its thickness changes from SL to BL [86], CdTe retains its direct band gap in all forms, i.e., SL, BL, TL, and bulk. The robustness of the direct band gap towards the thickness of a sheet is an excellent property because controlling the thickness to exactly SL throughout the entire area of a wafer-scale sheet is a challenging task [6, 87]. The underestimation of the band gap by PBE compare to HSE06 functional is evident, although the topologies of band structures remain the same. Both, valence band maxima (VBM) and conduction band minima (CBM), are located at the Brillouin zone center, i.e., Γ(0,0,0) point in 2D and retain their position in reciprocal

space in BL, TL, and even in bulk. The dispersion near Γ (i.e., $K - \Gamma - M$) is symmetric in both VBM and CBM. The PBE/HSE06 band gap of 2D CdTe is 1.070/1.919, which drops to 0.940/1.748, 0.931/1.719, and 0.751/1.599 (in eV) for BL, TL, and bulk, respectively. Our calculated HSE06 band gap of 1.599 eV of bulk CdTe is in good agreement with the available experimental value of 1.60 eV [80]. A similar decrease in band gap with the thickness is observed in other TMDCs, metal chalcogenides, and other layered materials, which is attributed to the quantum confinement effect along the z-axis in two-dimensional material and the dielectric screening in bulk cases. The robust direct band gap in the CdTe system is due to the high dispersion in the band structures near the band edges, while in the case of TMDCs, the less dispersive band edges change their positions with the variation of thickness of the sheet. The PDOS in the lower panel of Fig. 3.15(a) shows the dominant contributions of Te p-orbital with minor contributions from p and d orbitals of the Cd atom to VBM. The CBM is dominantly contributed by Cd s orbital along with weak contributions from Te s and p orbitals. The absence of high overlapping of the orbitals of Cd with Te atoms in PDOS indicates the ionic character of the Cd-Te bond, which is consistent with our bond character analysis (electron localization function + Bader charges) in the previous section. The higher density of states in VBM compared to CBM is due to the smaller dispersion in the band structure of the former compared to the latter.

In Fig. 3.15(b), we show the electronic structures of the newly predicted two-dimensional $CdTe_2$ in its SL, BL, and TL structures. It has an indirect band gap of 1.080/1.792, 1.053/1.758, and 0.982/1.70 in the unit of eV calculated with PBE/HSE functionals for SL, BL, and TL, respectively. The fundamental band gap decreases by 27/24 meV with PBE/HSE06 with increasing thickness from SL to BL of $CdTe_2$, which is much lower than the decrease of 130/171 meV in the case of CdTe. This smaller decrease is due to the weak interlayer interaction of $CdTe_2$ compared to CdTe. Further increase in thickness from BL to TL suppresses the band gap (PBE/HSE06) by 71/58 meV for $CdTe_2$ and 9/29 meV for CdTe. Furthermore, the VBM is located at the high symmetry point M(0.5,0.5,0), whereas CBM is at the midway in the $M - \Gamma$ k-path. They retain their positions against the thickness variation from SL to TL. Both VBM and CBM contributed from the Te-p orbital. Similar to CdTe, there is slight overlapping among the orbitals of Cd and Te atoms near the band edges in SL $CdTe_2$, reflecting the ionic bond character of Cd-Te. One can see a second minimum at symmetric point X(0.5,0,0) in the conduction band by 220 meV above the CBM in SL, which comes closer to CBM in the case of BL $CdTe_2$.
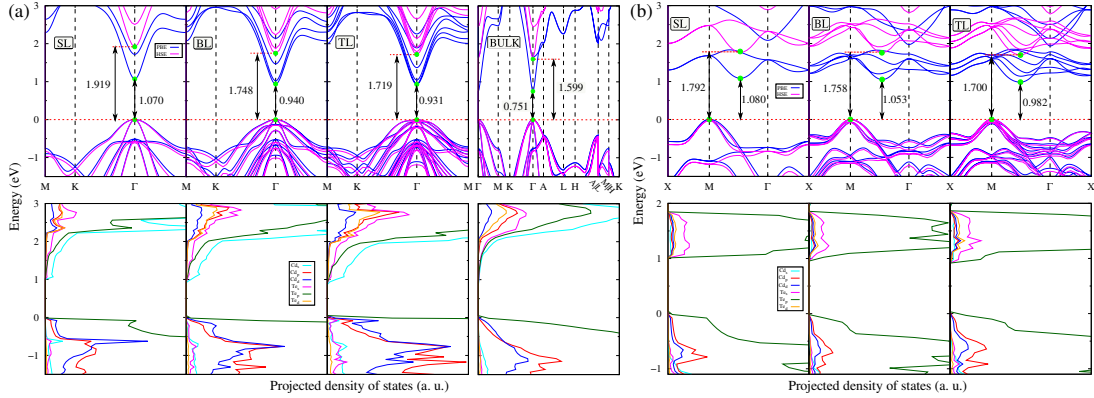
Figure 3.15: Electronic band structure calculated with PBE and HSE06 functionals and the corresponding PBE atom-projected density of states (PDOS) of Cd and Te atoms for (a) CdTe in its single-layer (SL), bilayer (BL), trilayer (TL), and bulk (b) $CdTe_2$ in its single-layer (SL), bilayer (BL), and trilayer (TL). The zero in the energy axis is denoted by the horizontal broken line, whereas the valence band maximum (VBM) sets to it. The band edges, i.e., VBM and CBM, are highlighted with solid green circles. The fundamental band gaps (in eV) with PBE and HSE06 are mentioned in each case.
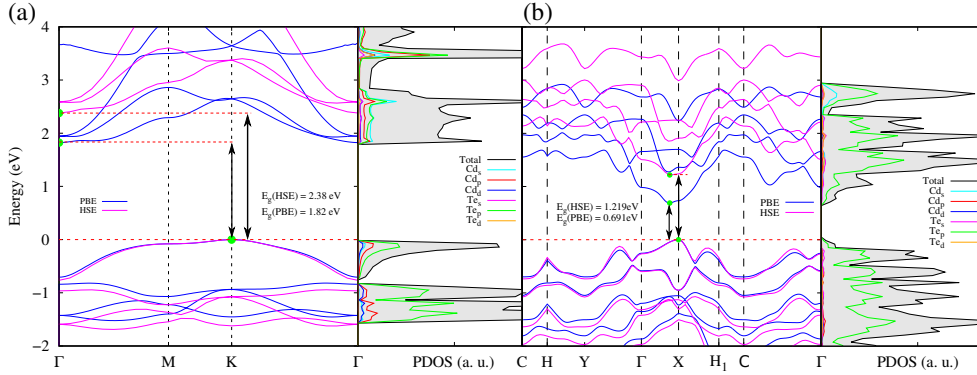
Figure 3.16: Electronic band structure calculated with PBE and HSE06 functionals and the corresponding PBE atom-projected density of states (PDOS) of Cd and Te atoms for single-layer (a) Cd_3Te_2 and (b) $CdTe_4$. The zero in the energy axis is indicated by the horizontal dashed line, which is set at the valence band maximum (VBM). The band edges (i.e., VBM and CBM) are highlighted with solid green circles, and the fundamental band gaps (PBE and HSE06) are mentioned.

We define the strain as $\varepsilon = \frac{a-a_0}{a_0}$, where a_0 and a are un-strained and strained lattice constants, respectively. Its negative value corresponds to a compressive strain and a positive value to a tensile strain. One of the weak points of monolayer TMDCs is the sensitive direct band gap

to external deformations, such that less than $\pm3\%$ of external strain makes it an indirect band gap semiconductor [88]. Synthesis of a strain-free single layer of a material is challenging because small deformations are ubiquitous due to the mismatch of the substrate's lattice and its thermoelectric expansion coefficient with the over-grown monolayer [89, 90]. Therefore, the robustness of the direct band gap to external deformations (i.e., tensile and compressive) is of high importance regarding the performance of devices. In Fig. 3.17, we investigate the electronic structure under external tensile and compressive strains. The strain causes a non-linear variation in the band gap of monolayer CdTe, which first increases by 0.5 eV in the range of 0~5% and then drops by 0.2 eV under 5 to 10% strain. But in the compression region, from 0 to -5%, a decrease of 0.1 eV in the band gap occurs. Increasing the compression further from -5 to -10% causes an increase of 0.1 eV in the band gap. The band gap retains its direct nature through the whole range of biaxial strain from 0 to -10% and from 0 to 6%. A direct-to-indirect transition occurs in the strained region beyond 7%. Close observation of bands near the VBM with the increase of tensile strain show two nearly degenerate (differ by 15 meV) secondary maxima on both sides of Γ are pushed upward gradually towards VBM. Beyond 7% strain, these secondary maxima cross the VBM resulting in an indirect band gap. The critical strain (for direct-to-indirect switching) of 7% for SL CdTe is considerably higher than 3% for monolayer MoS_2. Comparing the PDOS of the un-strained and strained configurations of CdTe, one can see the increase in the overlap between Cd-s and Te-p orbitals near the CBM under 10% strain. Due to the decrease in the dispersion of VBM under tensile strain, the density of states increases. Under compression, the CBM exchanges between Cd-s and Te-p orbitals.

The strain modulation of the monolayer $CdTe_2$ electronic structure is shown in Fig. S11. The band gap increases/decreases monotonically with tensile/compressive strains. The semiconductor-to-metal transition occurs by -10% biaxial compressive strain. Both VBM and CBM become flattened with the increase of tensile strain. The secondary maxima in the valance band move upward and cross the fundamental VBM under the 10% strain. Due to the flattened band edges under the stretching, there is a minor difference in the indirect and direct band gap. The CBM retains its position at the mid-way of the $M - \Gamma$ k-path, except for a small move towards M under 10% strain. Under compression, the band gap closes while retaining its CBM and VBM locations as an un-strained configuration. The change in band gap with strain is 0.07 eV/strain(%), which is higher than other 2D TMDCs, showing potential for optoelectronic devices.
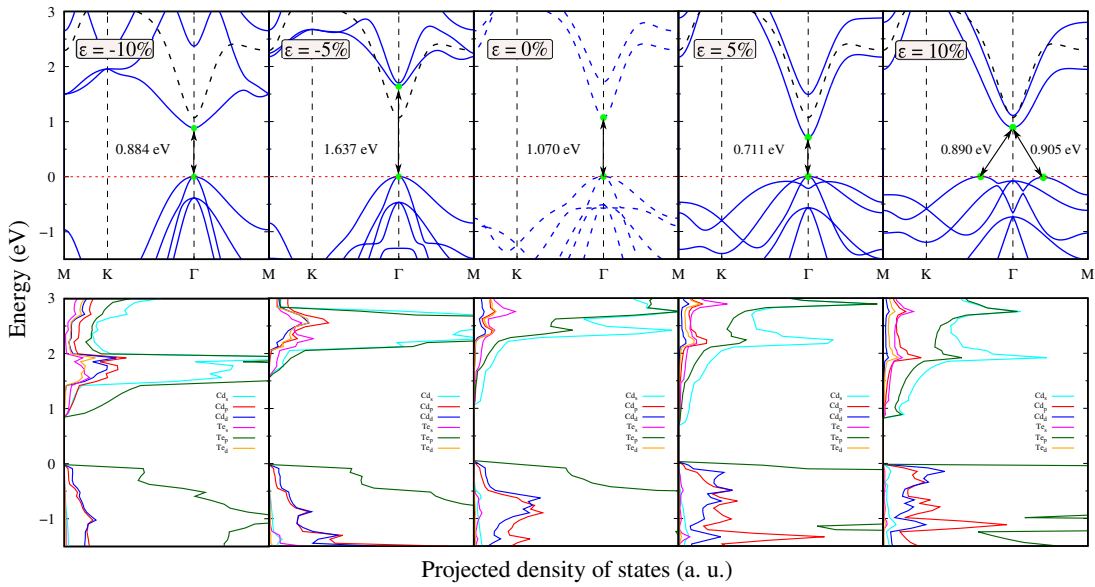
Figure 3.17: Electronic band structure and atom-projected density of states (PDOS) of unstrained and strained (i.e., tensile and compressive strained up to ±10%) monolayer CdTe using PBE functionals. The zero in the energy axis is denoted by the horizontal broken line and the VBM is set to it. The VBM and CBM are indicated with solid green circles. The lowest conduction band of the unstrained band structure (represented by a dashed line) is plotted on all strained band structures for comparison.
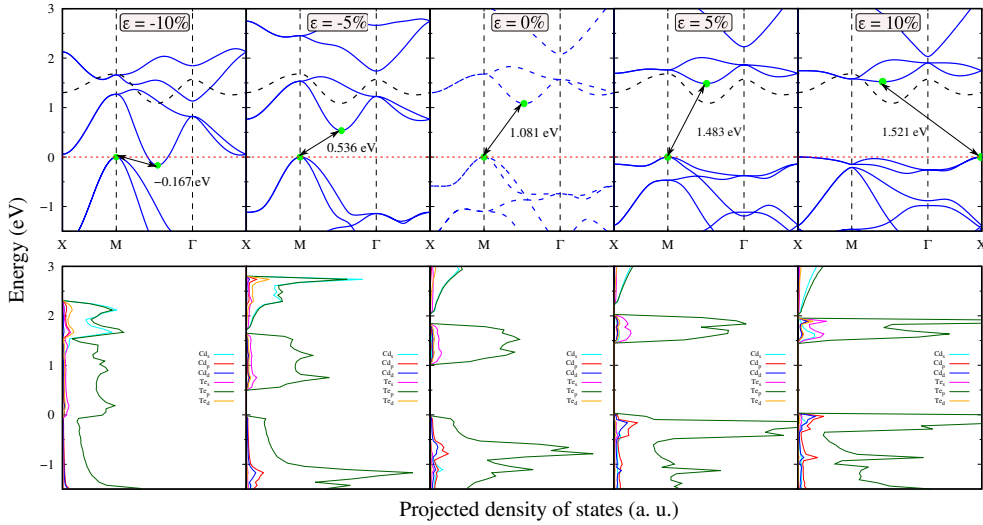
Figure 3.18: Electronic band structure and atom-projected density of states (PDOS) of unstrained and strained (i.e., tensile and compressive strained up to $\pm 10\%$) monolayer $CdTe_2$ using PBE functionals. VBM and CBM are indicated with solid green circles, and the zero in the energy axis (red dashed line) is set at VBM in each case. The lowest conduction band of the unstrained band structure (represented by dashed lines) is plotted on all strained band structures for comparison.

3.4 Conclusions

In summary, using USPEX code in conjunction with VASP, we found several low-energy Cd_xTe_y 2D structures in which hexagonal CdTe is at global minimum and $CdTe_2$ is only a few meV above the convex-hull. Passing these structures through the state-of-art stability filters proved their experimental accessibility. The Cd-Te bond character in both phases is predominantly ionic, but the Te-Te bond in 2D $CdTe_2$ has a covalent character. Contrary to monolayer MoS_2, the direct band gap nature of 2D-CdTe retains in the bilayer, trilayer, bulk, and strained configurations. The $CdTe_2$ has an indirect band gap which is highly tunable by strain. Its band gap becomes pseudo-direct due to the flattening of both VBM and CBM under the tensile strain but shows metallic behavior under 10% compression.

Chapter 4

Thermal transport in two-dimensional Ge$_x$S$_y$

4.1   2D Ge$_x$S$_y$

The demand for two-dimensional (2D) materials has significantly increased due to their unique properties and potential for miniaturization in future devices. One such material is graphene, derived from graphite, which exhibits exceptional characteristics such as high carrier mobility and lattice thermal conductivity (κ_l), making it suitable for efficient thermal transport [5, 6, 91]. However, in the context of thermoelectric devices, the efficiency at temperature T is quantified by a dimensionless figure of merit, $ZT = \frac{\sigma S^2 T}{\kappa_e + \kappa_l}$, where σ, S, κ_e, and κ_l represent electrical conductivity, Seebeck coefficient, electronic thermal conductivity, and lattice thermal conductivity, respectively. It is worth noting that ZT is inversely proportional to the κ_l. Therefore, the high κ_l and metallic nature of intrinsic graphene pose challenges for its direct use in thermoelectric devices, and various methods like nanostructuring and doping are employed to mitigate these issues [92]. Consequently, alternative materials are being explored, with 2D transition metal dichalcogenides (TMDs) gaining considerable attention. Nonetheless, most TMDs exhibit relatively high lattice thermal conductivity [93], prompting researchers to redirect their focus toward 2D IV-VI materials. These materials have emerged as a prominent research area due to their ability to achieve ultra-low lattice thermal conductivity and higher Seebeck coefficients [94].

The suitable band gap, earth abundance, and non-toxic characteristics of germanium sulfides and its constituent elements make the orthorhombic (*Pnma*) phase of GeS the primary focus of researchers. The monolayer GeS (*Pmn*2$_1$) can be obtained through mechanical exfoliation from its bulk and has shown great potential thermoelectric device applications due to its

high electron mobility and ultra-low lattice thermal conductivity. Similarly, the 1T structure of 2D GeS$_2$ [95] and the low-symmetric ($P2_12_12$) phase of two-dimensional (2D) Ge$_2$S [96] have also exhibited excellent properties, particularly as thermoelectric and anode materials. However, while the bulk counterparts of these Ge$_x$S$_y$ compounds exhibit various polymorphs, such as cubic [97], orthorhombic [98], amorphous [99] phases of GeS, and monoclinic [100], orthorhombic [101], and beta [102] phases of GeS$_2$, it remains unexplored whether their monolayer forms possess unique and undiscovered structures. This intriguing possibility suggests that the monolayers of these compounds may exhibit distinct properties, thereby warranting further investigation and exploration.

In the pursuit of obtaining 2D counterparts of materials, researchers employ various experimental procedures. These methods can be of two categories: top-down and bottom-up approaches. In the first approach, a single layer is exfoliated from the bulk material, which is particularly feasible for layered materials held together by van der Waals forces such as graphene [5] or 2D TMDs. Conversely, in the bottom-up approach layer grows on a substrate from vapors of precursors such as physical or chemical vapor depositions [103]. In parallel, density functional theory (DFT) can predict a single layer by cutting it from the layered bulk and allowing for relaxation with sufficient vacuum in the out-of-plane direction. In contrast, the non-layered bulk materials lack preferred planes for cleaving a single layer, leading to many possible 2D structures along various planes. Among these, the one with the lowest formation energy is energetically favorable, called the ground-state 2D structure of the given composition. The ground states of materials have particular importance due to their higher possibility of experimental realization. Another strategy involves replacing atoms in already explored monolayer lattices with the elements under investigation and searching for the most energetically favorable configuration, such as in the case of germanene and silicene [59]. However, manually arranging the atoms in all possible structures can be a tedious task. Fortunately, significant advancements in computational tools have revolutionized the field of materials science. Among these tools, the Universal Structure Predictor: Evolutionary Xtallography (USPEX) [37, 70] stands out with its high success rate among genetic-algorithm-based search codes. USPEX offers a specific 2D search capability, making it particularly suitable for identifying the lowest-energy phases in compounds with variable compositions, such as 2D Cd$_x$Te$_y$ [104]. By harnessing the power of USPEX, one can efficiently search for and identify the energetically stable structures of 2D Ge$_x$S$_y$ compounds.

This study predicts novel ground-state structures of 2D Ge$_x$S$_y$ compounds with three different compositions: Ge$_2$S, GeS, and GeS$_2$, that exhibit higher stability than their previously reported counterparts. Specifically, we focus on their crystal structures, electronic structure, and phonon transport properties. The 2D GeS phase demonstrates lower lattice thermal con-

ductivity compared to its orthorhombic monolayer counterpart. We delve into the underlying mechanisms responsible for the ultra-low κ_l of 2D GeS, examining factors such as anharmonicity, phonon group velocity, their lifetimes, and weighted phase space for three-phonon scattering. Moreover, 2D GeS_2 shows intriguing in-plane anisotropic elastic stiffness and κ_l, while 2D Ge_2S has comparatively higher κ_l. The interplay of anisotropic acoustic and low-frequency optical phonon group velocity and relatively higher lifetimes to their distinguished κ_l in 2D GeS_2 makes this study of fundamental interest.

4.2 Computational methodology

The search for lowest-energy structures of 2D germanium sulfide involves USPEX [37, 70] in conjunction with the Vienna Ab initio Simulation Package (VASP) [105]. Our variable-compositional search is constrained to a layer thickness of 0~6 Å and the constituent atoms in a unit cell of 2~12. In this search, a total of 80 generations are considered. The first generation contains 200 randomly created structures, while the subsequent generations have 80 structures each that evolve through natural selection and variation operators such as mutation, crossover, and symmetry operations. The relative energetic stability of different compositions and structures was determined by comparing the formation energy per atom (E_f), which is calculated using the equation:

$$E_f = \frac{1}{x+y}[E(Ge_xS_y) - xE(Ge) - yE(S)] \tag{4.1}$$

In this equation, $E(Ge_xS_y)$, $E(Ge)$, and $E(S)$ represent the total energies of the lowest possible 2D configurations of Ge_xS_y, elemental germanium, and sulfur, respectively. The total energy of each structure is calculated using the projector-augmented wave (PAW) [26] method, which is well-suited for handling core electrons. To account for the electronic exchange-correlation interaction, the generalized gradient approximation (GGA) [18] with the Perdew-Burke-Ernzerhof parameterization (PBE) is employed. In order to maximize computational efficiency, a strategy is adopted that includes a relatively coarse k-mesh with resolution of $2\pi \times (0.08 \sim 0.04)$ Å^{-1}, a smaller cutoff energy of 450 eV for plane wave expansion, a vacuum size of 15 Å, and exclusion of the zero damping of Grimme (DFT-D3) [71] for the van der Waals corrections in the first 60 generations, followed by its inclusion in the final 20 generations.

To ensure the accuracy, the resulting 2D Ge_xS_y structures undergo re-optimization using a lager cutoff energy of 540 eV, a vacuum size of 20 Å, and a denser Γ-center k-mesh with a resolution of $2\pi \times 0.02$ Å^{-1}. The convergence criteria for energy is set to 10^{-8} eV and for forces to 10^{-3} eV/Å. Electronic band structures are computed using both the GGA and

Heyd-Scuseria-Ernzerhof (HSE06) [23] methods. For *ab initio* molecular dynamics (AIMD) simulations, we employ the NVT ensemble with a step size of 1 fs and a total time of 10 ps at temperatures of 300 K, 600 K, and 900 K. We use the Nosé-Hoover thermostat [73] to maintain constant temperature during simulations. The Phonopy code [72] is used to calculate the phonon dispersion based on the finite displacement method with supercells. We use supercell of $6 \times 5 \times 1$ for Ge_2S, $5 \times 5 \times 1$ for GeS, and $3 \times 3 \times 1$ for GeS_2, which are the same size as those used for AIMD simulations.

We utilized an iterative self-consistent approach implemented in the ShengBTE package [2] to solve the phonon Boltzmann transport equation (PBTE) and predict the lattice thermal conductivity. This method relies on two sets of interatomic force constants (IFCs): harmonic (second-order) and anharmonic (third-order). The harmonic IFCs are obtained using the Phonopy code [72] and anharmonic IFCs through the thirdorder.py python script based on the method developed by Lindsay *et al.* [44] in combination with VASP. With these sets of IFCs, one can express the $\alpha\beta$ component of lattice thermal conductivity tensor as [2]:

$$\kappa_l^{\alpha\beta} = \frac{1}{k_B T^2 V N} \sum_\lambda f_0(f_0 + 1)(\hbar\omega_\lambda)^2 v_\lambda^\alpha \tau_\lambda (v_\lambda^\beta + \Delta_\lambda^\beta) \qquad (4.2)$$

Here, $\lambda(k, p)$ represents a phonon mode characterized by the wave vector k and branch number p. Δ_λ^β with the dimension of velocity is the correction to relaxation time approximation (RTA) prediction. V denotes the unit-cell volume, ω is the phonon frequency, N is the number of q points in the first Brillouin zone (BZ) for a Γ-centered regular grid, T represents the temperature, v_λ^α is the group velocity of the phonon in the α direction, τ_λ is the λ phonon lifetime, and f_0 is the phonon occupation number given by the Bose-Einstein distribution. The obtained κ_l is rescaled for 2D Ge_xS_y by multiplying a factor L_z/d_{eff}, where L_z is the total length of the unit cell along the z direction and d_{eff} is the effective-thickness of the materials obtained from the corresponding bulk structure. The values of d_{eff} are 7.579, 9.068, and 7.710 in units of Å for Ge_2S, GeS, and GeS_2, respectively [see Fig. 4.1 for details]. The long-range interactions are included by Born effective charge tensors computed with the density functional perturbation theory (DFPT) [106].

4.3 Results and discussion

4.3.1 Structure prediction and stability

The comparative energetic stability among various structures of a material can be represented by the energy convex hull (ECH). The ECH of the 2D Ge:S system [See Fig. 4.2] is con-
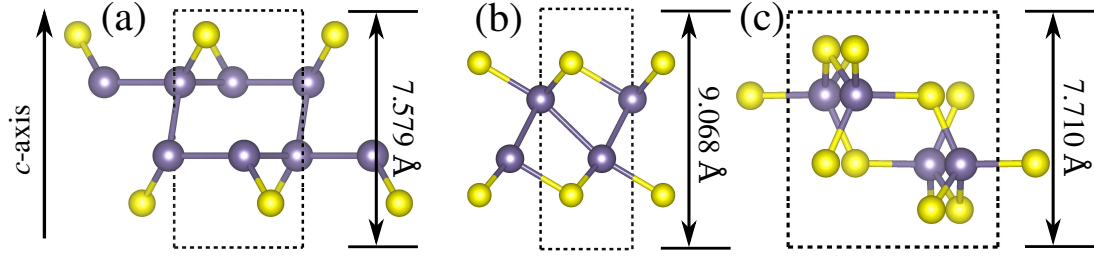
Figure 4.1: The fully relaxed unit cells of bulk (a) Ge_2S, (b) GeS, and (c) GeS_2 structure. The vertical double-headed arrows show the effective thicknesses for each 2D Ge_xS_y compound.

structed by plotting the formation energy per atom, given by Eq. (1), of a given composition ratio in all possible structures along the y-axis and composition ratio $S/(Ge+S)$ along the x-axis. In literature, several polymorphs of bulk GeS, such as orthorhombic α, cubic, and amorphous phases [97, 99, 107], have been reported due to different bonding modes. ECH construction is an efficient and powerful tool for identifying the most stable structure and composition [33], especially for materials with numerous polymorphs. These most stable structures will lie on the convex hull, such as in the Ge:S system, Ge_2S (magenta), GeS (cyan), and GeS_2 (dark blue), as shown in Fig. 4.2. These lowest-energy 2D Ge_2S, GeS, and GeS_2 (discussed later) have different structures and lower formation energies than the previously reported ones. For comparison, the formation energies of the already reported 2D Ge_2S [96], GeS [108], and GeS_2 [95] structures are represented in Fig. 4.2 by magenta, cyan, and blue triangles, respectively. The previously known 2D Ge_xS_y structures, i.e., Ge_2S, GeS, and GeS_2, have higher formation energies than our's predicted counterpart monolayers by 85, 47, and 84 in units of meV/atom, respectively, and consequently occupy positions above the convex hull. The worth noticing from the ECH analysis is the superior energetic stability of our predicted Ge_xS_y that indicates easier experimental accessibility. Therefore they deserve a detailed stability analysis, and we constrain the discussion to the structures on the convex hull only.

The phonon band structure, which provides critical insights into the dynamic stability of the newly predicted 2D phases of the Ge_2S, GeS, and GeS_2, are determined and shown in Fig. 4.3. These results reveal the dynamic stability of the 2D Ge_2S, GeS and GeS_2, as there are no imaginary frequencies in Fig. 4.3(a, b, and c). There are total of $3n$ phonon branches, where n is the number of atoms in the primitive unit cell. The first three lowest-frequency phonon branches are called acoustic phonons, which are further classified into transverse acoustic (TA), longitudinal acoustic (LA), and z-axis acoustic (ZA). The ZA mode, also called flexural mode, represents the out-of-plane atomic vibrations and has a quadratic wave vector dependence contrary to the TA and LA, which have linear dispersion near the Γ-point. In Fig. 4.3(c),
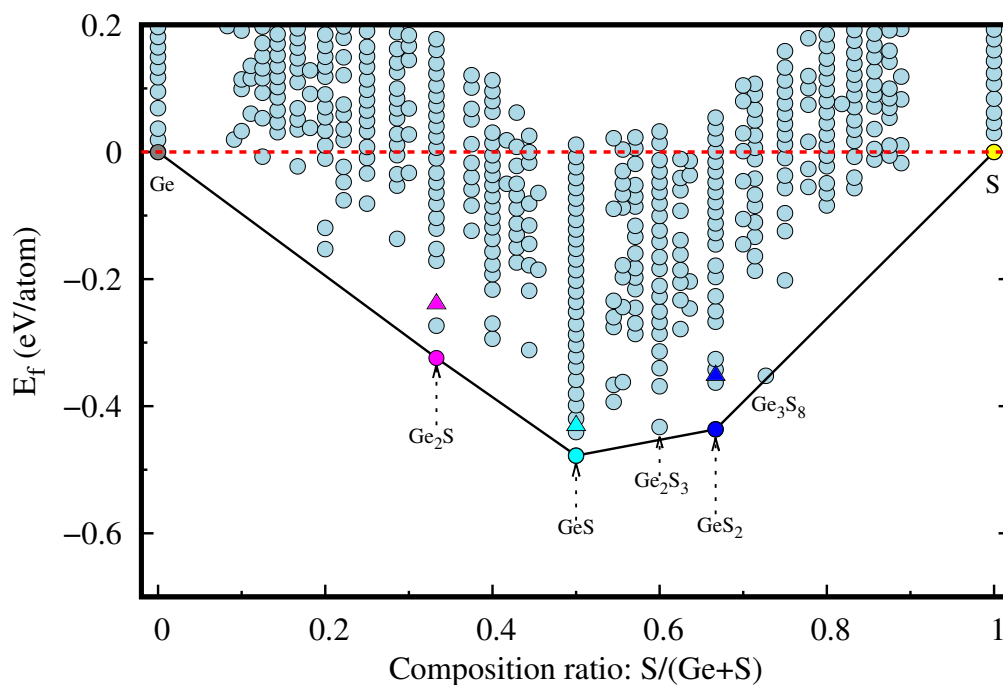
Figure 4.2: This figure shows the evolution of the energy convex hull (ECH) during the US-PEX search, where the solid bounding curve indicates the final ECH of the 2D Ge-S system. The energetically most stable structures of 2D Ge$_x$S$_y$ are highlighted with various colored circles, whereas those previously reported ones are represented with filled triangles.
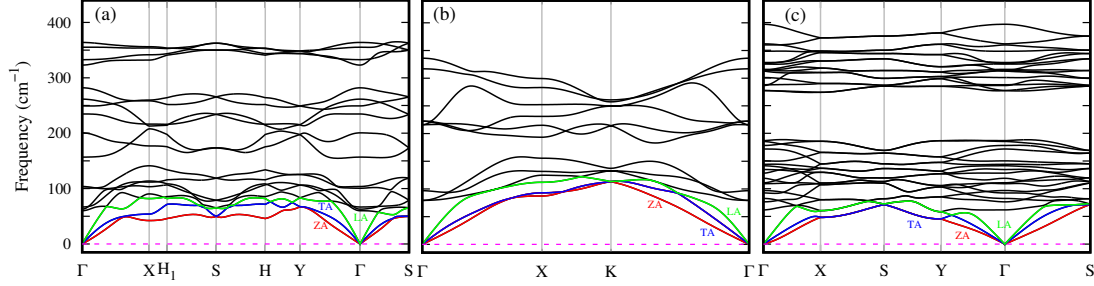
Figure 4.3: Phonon band structures of 2D (a) Ge$_2$S, (b) GeS, and (c) GeS$_2$. The green, blue, red, and black colors represent the longitudinal acoustic (LA), transverse acoustic (TA), flexural acoustic (ZA), and optical mode phonons, respectively.

the LA mode along Γ-Y direction has softer behavior (smaller slope) than along the Γ-X direction. This difference in the phonon dispersion suggests the presence of anisotropic lattice thermal conductivity, which will be discussed later. The remaining $3n-3$ phonon branches are known as optical branches, divided into low and high-frequency bands separated by a gap. This gap is 16/41 cm^{-1} in Ge$_2$S/GeS while 88 cm^{-1} in GeS$_2$. The common observation from Fig. 4.3 is the overlapping of the low-frequency optical phonons with acoustic phonons. It is one of the indicators of the high possibility of three-phonon scattering, which will eventually decrease lattice thermal conductivity. The maximum phonon frequency (ω_{max}) in all predicted structures is below 400 cm^{-1}. Specifically, ω_{max} is 365 cm^{-1} for Ge$_2$S, smaller than its $P2_12_12$ phase (561 cm^{-1}) [96], and 337 cm^{-1} for GeS, in the same range as the $Pmn2_1$ phase (~330 cm^{-1}) [94]. ω_{max} is 397 cm^{-1} for 2D GeS$_2$, comparable to its $1T$ phase (~400 cm^{-1}) [95]. Further, the dispersion in the high-frequency optical branches is comparatively lower in GeS$_2$ than in Ge$_2$S and GeS.

In addition to energetic and dynamic stability, the elastic stability of predicted 2D Ge$_x$S$_y$ provides more insights into their viability. The elastic stability of our predicted 2D monoclinic Ge$_2$S ($P2/c$), GeS$_2$ ($P2_1/c$), and trigonal GeS ($P\bar{3}m1$) is confirmed using the corresponding stability criteria [79] based on the elastic constants presented in Table 4.1. Specifically, GeS with trigonal structure satisfies the criteria $C_{11} > 0$, $C_{66} > 0$, and $C_{11} > |C_{12}|$. The elastic constants of GeS$_2$ satisfy the criteria for rectangular lattice, i.e., $C_{11} > 0$, $C_{66} > 0$, and $C_{11} \times C_{22} > C_{12}^2$. Similarly, due to its oblique structure, Ge$_2$S satisfies the criterion $det\,|C_{ij}| > 0$, with $i,j = 1,2,6$.

Generally, 2D materials are more vulnerable to high temperatures compared to their bulk. Therefore, analyzing the thermal stability of predicted 2D Ge$_x$S$_y$ compounds at elevated temperatures is worthwhile. For this purpose, AIMD simulations are performed to investigate the thermodynamic stability of newly predicted monolayers at different temperatures of 300, 600,

and 900 K. The simulations results are shown in Fig. 4.4 at 300 K and Fig. 4.5 & 4.6 at 600 and 900 K temperatures, respectively. These results reveal that 2D GeS and GeS$_2$ exhibit higher structural stability because no significant changes were observed in the overall morphology or bond lengths at 300, 600, and 900 K. However, the thermally stable 2D Ge$_2$S at 300 and 600 K becomes unstable when the temperature rises to 900 K, as evident from the broken bonds in the inset of Fig. 4.6(a). We conclude this section with the remarks that our predicted three compositions of 2D Ge$_x$S$_y$ are energetically more favorable than previously reported ones, stable dynamically and elastically, and can withstand higher temperatures.

4.3.2   Structural analyses

The properties of a material, either bulk or two-dimensional, are entangled with its crystal structures [109]. Therefore, before delving into electronic structure and phonon transport properties, it is crucial to investigate the crystal structures of the low-energy lying 2D Ge$_x$S$_y$. In Figs. 4.7(a–c), we show the 2D structures of the stable compositions Ge$_2$S, GeS, and GeS$_2$, respectively. The top and side views of each structure in these figures will facilitate the readers to understand the discussion in this section. The dashed lines represent the primitive unit cell in each case. Regarding symmetry, Ge$_2$S has a monoclinic unit cell with space group $P2/c$, GeS$_2$ unit cell has space group $P2_1/c$, while GeS adopts trigonal structure with space group $P\bar{3}m1$. Due to the low symmetry of 2D Ge$_2$S, views of various orientations are shown in Fig. 4.7(a). It composes two sublayers; the red-dashed and the solid-black rhombic lattices represent the bottom and top sublayers, respectively. The top sublayer can be obtained from the bottom by mirror symmetry along the z-axis plus a glide of 0.5b along the $\overrightarrow{b}$ lattice vector, where b is the lattice constant. For clarity, we show the top view of only the bottom sublayer on the right side of Fig. 4.7(a). It consists of irregular (unequal bonds) parallel zigzag chains of Ge atoms in the ab-plane connected through S atoms. Each Ge atom makes four bonds, one with the S atom and three with other Ge atoms, of which two Ge belong to the same sublayer and one Ge to the neighboring sublayer. Hence, the two sublayers are attached by Ge-Ge bond of length 2.52 Å. The Ge-Ge bond lengths in zigzag chain are 2.47 Å and 2.51 Å. Other lattice parameters and mechanical properties, such as elastic constants and Poisson's ratios, are tabulated in Tab. 4.1.

Fig. 4.7(b) shows the top and side views of 2D GeS. It consists of two oppositely buckled honeycomb sublayers with AB stacking. In this structure the inplane coordinates of the S atoms are $(1/3\overrightarrow{a}, 1/3\overrightarrow{b})$ and of the Ge atoms are $(0,0)$ and $(1/3\overrightarrow{a}, 2/3\overrightarrow{b})$, where $\overrightarrow{a}$ and $\overrightarrow{b}$ are the lattice vectors. For GeS, $a = b = 3.63$ Å is the optimized lattice constant. Within each sublayer, Ge/S atoms are bonded with three S/Ge atoms through a bond length of 2.44 Å. The two sublayers are then weakly connected by a Ge-Ge bond of length 2.93 Å. Fig. 4.7(c)

Figure 4.4: The total energy per unit cell and temperature profiles of 2D materials (a) Ge$_2$S, (b) GeS, and (c) GeS$_2$ are obtained through AIMD simulations at 300 K. The simulated structures were visualized from top and side in the insets after a simulation time of 10 ps.
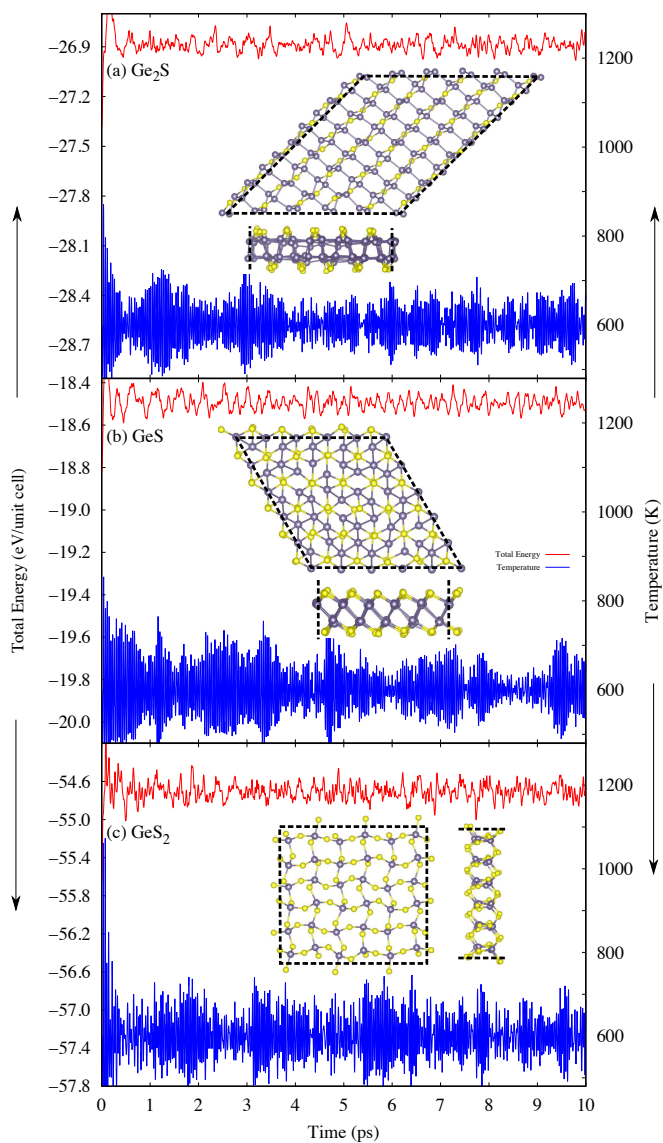
Figure 4.5: The total energy per unit cell and temperature profiles of 2D materials (a) Ge_2S, (b) GeS, and (c) GeS_2 are obtained through AIMD simulations at 600 K. The simulated structures are visualized from top and side in the insets after a simulation time of 10 ps.
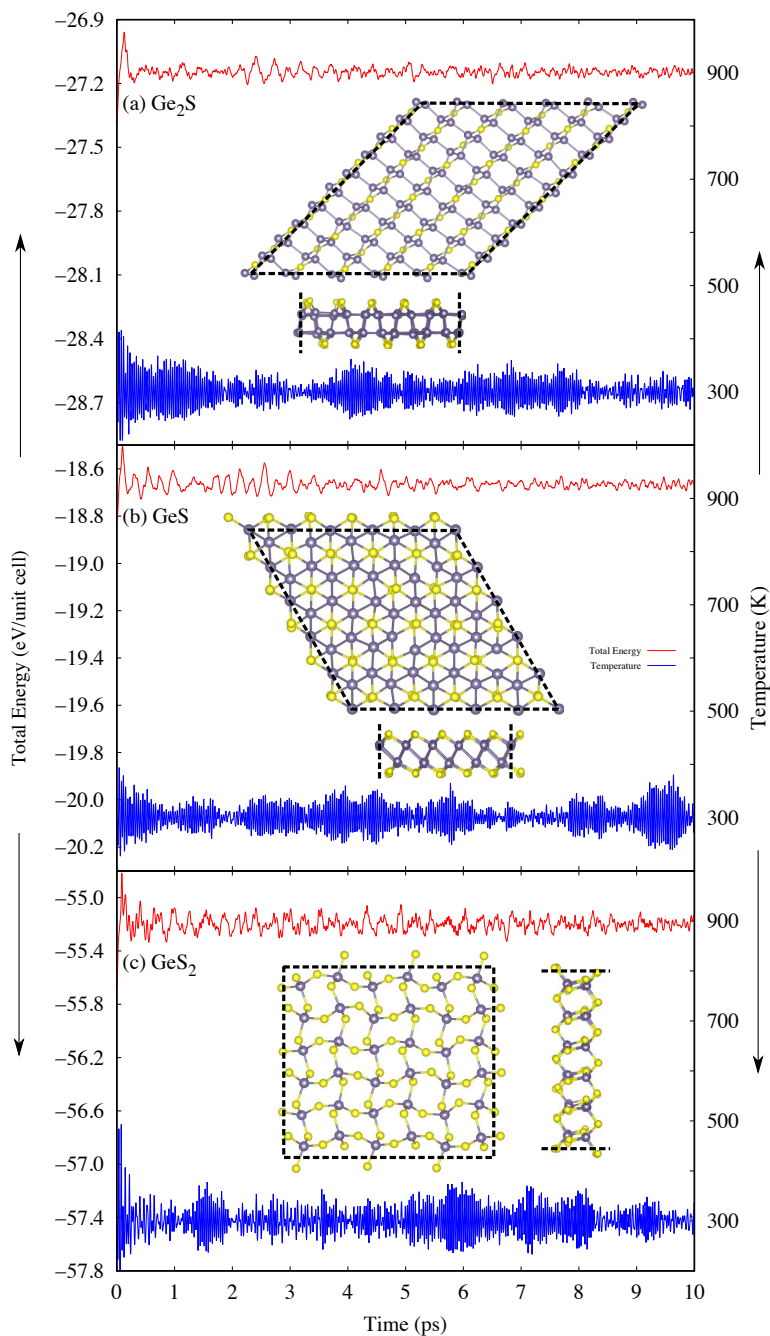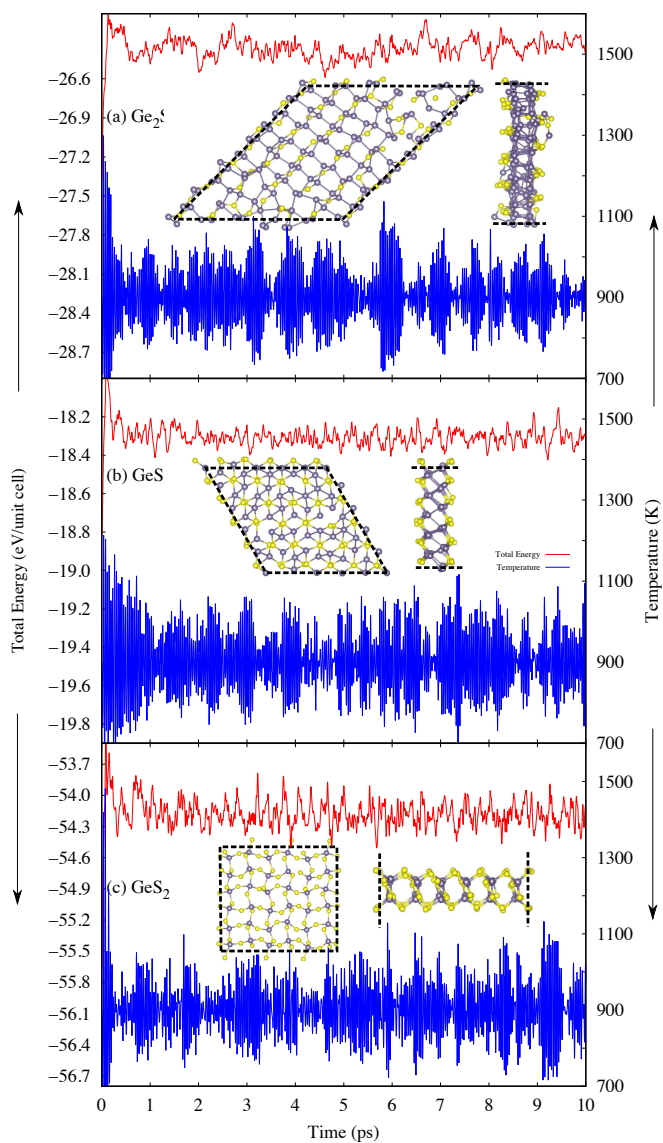
Figure 4.6: The total energy per unit cell and temperature profiles of 2D materials (a) Ge_2S, (b) GeS, and (c) GeS_2 are obtained through AIMD simulations at 900 K. The simulated structures are visualized from top and side in the insets after a simulation time of 10 ps.
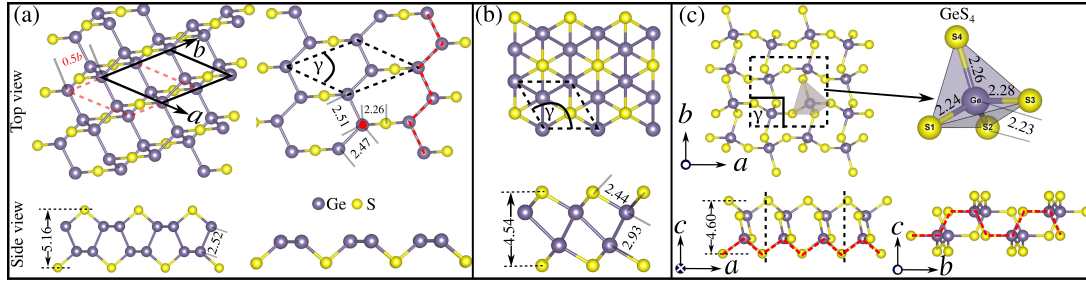
Figure 4.7: The top and side views of 2D (a) Ge$_2$S, (b) GeS, and (c) GeS$_2$ and the primitive unit cell are shown with dashed lines in each top view. All bond lengths and thicknesses of the layers are shown in the unit of Å. The solid circle (red) in (a) represents the bond between two sublayers. The red-dashed lines in (c) represent zigzag and armchair directions.

depicts that the primitive unit cell of 2D GeS$_2$ constitutes corner-sharing distorted (unequal edges) GeS$_4$ tetrahedra. The GeS$_4$-tetrahedron contains the Ge atom in its center, bonded with four S atoms at the corners. All four Ge-S bonds in GeS$_4$ tetrahedron have different lengths, i.e., 2.23, 2.24, 2.26, 2.28 in Å, which reduces the unit-cell symmetry from orthorhombic *Pbcm* (β-2D silica [110]) to monoclinic $P2_1/c$. The side views in Fig. 4.7(c) exhibit the zigzag morphology along *a*-axis and armchair along the *b*-axis. The GeS$_4$ tetrahedra centers align in the *ac*-plane and buckle in the *bc*-plane, which leads to a hinge-like structure along the *b*-axis. This arrangement in 2D GeS$_2$ results in a rectangular lattice with lattice parameters $a = 6.87$ Å and $b = 6.17$ Å. The structural anisotropy of the lattice is reflected in its high elastic anisotropy, where Young's modulus along the *a*-axis is 63.8 Nm^{-1}, which is more than twice of along the *b*-axis (27.6 Nm^{-1}). Like phosphorene [111, 112], we expect that GeS$_2$ will have high anisotropic lattice thermal conductivity because it is often directly proportional to the elastic modulus [113].

4.3.3   Electronic structure

The electronic band structure and the total density of states (DOS) with projected density of states (PDOS) for the three compositions of 2D Ge$_x$S$_y$ are presented in Fig. 4.8. Its first look shows the semiconducting nature of all these compositions. 2D Ge$_2$S in Fig. 4.8(a) depicts a nearly direct and narrow band gap of 0.12/0.84 eV using PBE/HSE06 functional. The valence band maximum (VBM) and conduction band minimum (CBM) occur along $\Gamma - $ C $-$ V $-$ S path. The complete *k*-path used for plotting this band structure is given in Fig. 4.9(c). Interestingly, the *k*-points corresponding to the band edges, denoted by (C, V), do not occur along the high symmetry *k*-path of the first Brillouin zone (BZ). We identified this behavior of 2D Ge$_2$S from Fig. 4.9(a), where the band edges of the high-symmetry *k*-path

Structure (sp. group)	Lattice parameters a (Å), b (Å), γ (°)	Elastic constants (Nm^{-1}) $C_{11}, C_{22}, C_{12}, C_{66}$	Young's moduli Y_x, Y_y (in Nm^{-1})	Poisson's ratio ν_x, ν_y
Ge$_2$S ($P2/c$)	4.98, 5.56, 45°	47.80, 54.68, 8.07, 27.96 $C_{26} = 10.03, C_{16} = 5.84$	46.6, 53.3	0.147, 0.169
GeS ($P\bar{3}m1$)	3.63, 3.63, 120°	85.40, 85.40, 28.46, 28.47	75.9, 75.9	0.333, 0.333
GeS$_2$ ($P2_1/c$)	6.87, 6.17, 90°	64.58, 27.84, 4.22, 12.56	63.8, 27.6	0.152, 0.065

Table 4.1: Structural and elastic properties of 2D Ge$_x$S$_y$ compounds. Young's moduli and Poisson's ratios are calculated from the elastic constants by the corresponding formulas: $Y_x = (C_{11}C_{22} - C_{12}^2)/C_{22}$, $Y_y = (C_{11}C_{22} - C_{12}^2)/C_{11}$, $\nu_x = C_{12}/C_{22}$, and $\nu_y = C_{12}/C_{11}$.

[Fig. 4.9(b)] does not match the totalDOS. This discrepancy should be attributed to the band structure being limited to only high-symmetry k-points while the total DOS covers the whole first BZ. The k-path is revised, as shown in Fig. 4.9(c), by including accurate band edges [C (0.333 0.384 0), V (0.37 0.425 0)] determined from DOS with a denser k-mesh of reciprocal space resolution of $2\pi \times 0.004$ Å^{-1}. Due to the high dispersion of band structure at CBM, there is a lower density of states than VMB. Furthermore, one can analyze the atomic orbital contributions to the band structure by PDOS, right panel in Fig. 4.8(a). It implies that the VBM of 2D Ge$_2$S is contributed by the p-orbitals of both Ge and S atoms, whereas the CBM mainly originates from the s-orbital of the Ge atom.

The 2D GeS and GeS$_2$ exhibit band structures in Fig. 4.8 (b & c) with indirect band gaps. Specifically, the VBM of 2D GeS is located on both sides of the Γ-point, i.e., along $\Gamma - X$ and $\Gamma - K$. The CBM is located at the X point, where the band structure is highly asymmetric, as shown in Fig. 4.8(b). The asymmetric conduction band around the CBM is a footprint of the electrical anisotropy. The VBM of 2D GeS includes the p and s orbitals of S and Ge atoms, respectively. Its CBM is composed of Ge-s, Ge-p, and S-p orbitals. 2D GeS$_2$ in Fig. 4.8(c) has VBM at Γ point and CBM at the Y point of the first Brillouin zone. The valance and conduction bands are flat near the band edges and have a higher density of states than 2D Ge$_2$S and GeS$_2$. The p-orbital of the S atom mainly contributes to the VBM and CBM, and there is also a comparable contribution from the Ge-s orbital to the CBM. The fundamental band gaps, calculated with PBE functionals, are 0.72/1.85 eV for 2D GeS/GeS$_2$. The dispersions of band structures with HSE06 functional remain similar to PBE, but the fundamental band gaps open to 1.05 eV for 2D GeS and 2.92 eV for 2D GeS$_2$. Thus, we have narrow, medium, and wide band gap 2D semiconductors: Ge$_2$S, GeS, and GeS$_2$, respectively.
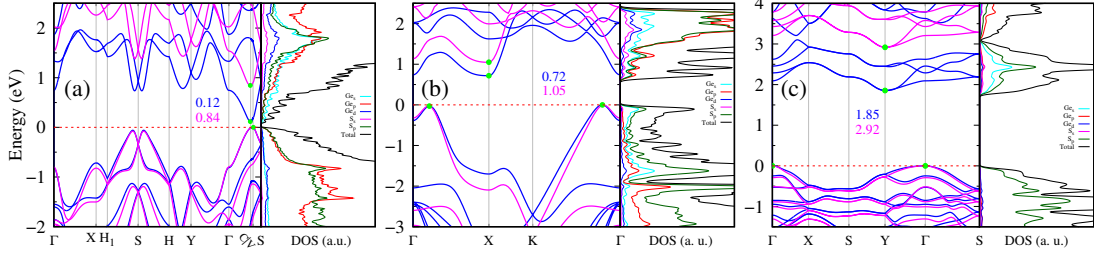
Figure 4.8: Electronic band structures using PBE (blue)/HSE06 (magenta) functionals and PBE total DOS with the corresponding projected density of states (PDOS) of Ge and S atoms are presented for 2D materials: (a) Ge_2S, (b) GeS, and (c) GeS_2. The zero of the energy axis is referenced to a horizontal red-dashed line that aligns with the valence band maximum (VBM). The band edges, i.e., VBM and CBM (conduction band minimum), are highlighted with solid green circles. The fundamental band gaps (in eV) are mentioned for each case.

4.3.4   Phonon transport in 2D Ge_xS_y compounds

Lattice thermal conductivity (κ_l) is a key characteristic of phonon transport and is obtained by iteratively solving the linearized phonon Boltzmann transport equation (PBTE). The solution of PBTE relies on second and third-order interatomic force constants (IFCs) as inputs. The influence of four-phonon scattering is disregarded due to its minimal impact on phonon transport in materials like 2D Ge_xS_y, which lack optical-acoustic gaps in phonon dispersions [114] (see Fig. 4.3). The third-order IFCs capture the phonon-phonon scattering processes and play a crucial role in predicting reliable thermal conductivity. A cutoff radius determines the region of interatomic interactions for third-order IFCs calculations. Selecting an appropriate cutoff radius ensures the proper inclusion of anharmonic interactions and improves the accuracy of κ_l. Furthermore, solving the PBTE involves discretizing the reciprocal space into a q-point grid hence achieving accurate κ_l requires a sufficiently dense q-point grid. Considering inadequate cutoff radii and q-point grids can lead to orders of variations in reported κ_l values. For instance, in the case of phosphorene, different κ_l values in the literature can be attributed to variations in the chosen cutoff radii and q-point grids [111, 112]. Therefore, to avoid ambiguity in κ_l, we present its convergence against the cutoff radius and q-point grid in Fig. 4.10. These figures depict an enormous variation of κ_l in the lower cutoff radius, which does not include sufficient nearest neighbors for interactions, and course q-point grid. We achieve sufficient convergent κ_l by considering cutoff radii of 7.4 Å, 10.8 Å, and 6.3 Å for 2D Ge_2S, GeS, and GeS_2, respectively. These include up to the 20th nearest neighbors for Ge_2S and 22nd for GeS and GeS_2. Our q-point grid tests show that κ_l well converges at $60\times60\times1$, $100\times100\times1$, and $45\times45\times1$ for Ge_2S, GeS, and GeS_2, respectively.

Figures 4.11(a-c) depict the temperature-dependent lattice thermal conductivities of 2D
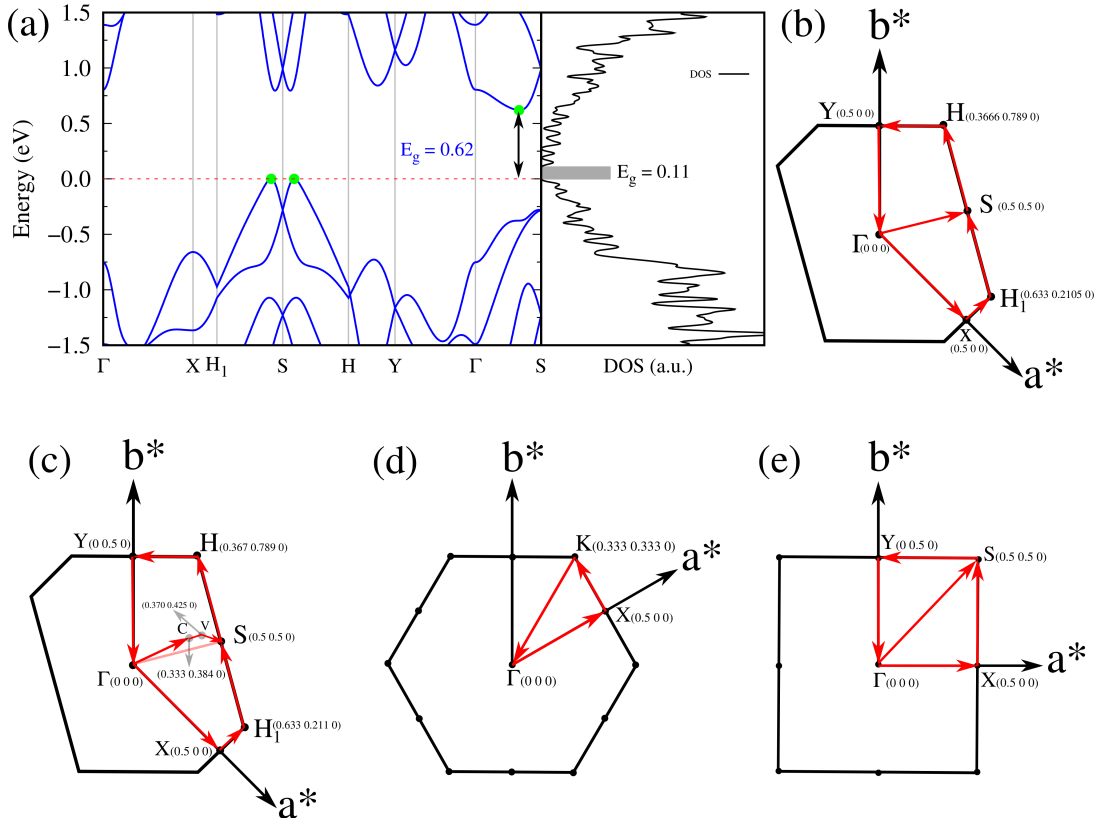
Figure 4.9: (a) The band structure of the 2D Ge$_2$S using the k-path shown in (b) along the high-symmetry points in the first Brillouin zone does not capture the correct band edges, evident from its mismatch with the density of states. Therefore, the k-path for Ge$_2$S is revised as in (c) to include the correct band edges denoted by C (0.333 0.384 0) and V (0.37 0.425 0). The k-path for extracting the band structures of 2D GeS and GeS$_2$ are presented in (d) and (e), respectively.
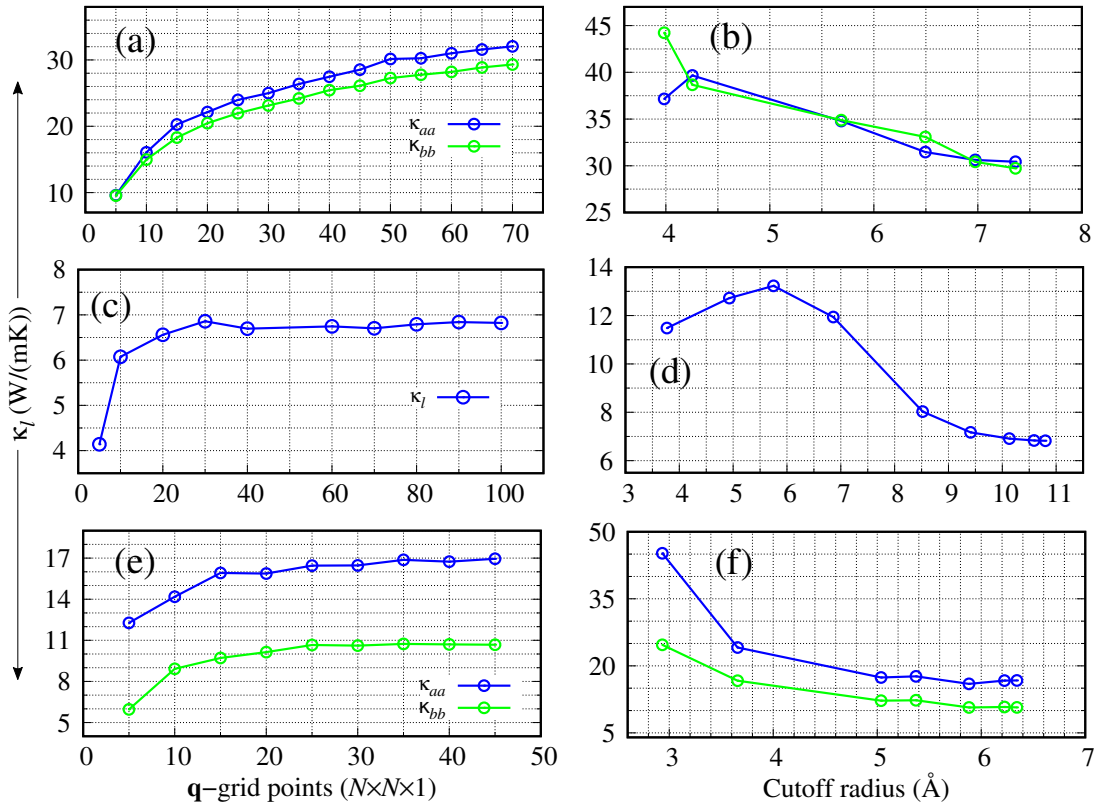
Figure 4.10: Convergence test of lattice thermal conductivity (κ_l) at 300 K against q points of Γ-centered grid and cutoff radii (used in calculations of third-order IFCs) for 2D (a, b) Ge_2S, (c, d) GeS, and (e, f) GeS_2.

Ge$_2$S within the stable temperature range of 200-600 K, 2D GeS and GeS$_2$ compounds over the temperature range of 200-900 K. Specifically, GeS has a room temperature κ_l of 6.82 Wm^{-1}K^{-1}, which is lower than monolayer MoSe$_2$, WSe$_2$, and phosphorene [115, 116]. Importantly, it is also smaller than its meta-stable orthorhombic phase (10.5/7.8 Wm^{-1}K^{-1} along zigzag/armchair direction) but higher than other IV-VI 2D compounds like GeSe (6.7/5.2 Wm^{-1}K^{-1}), SnS (4.7/4.4 Wm^{-1}K^{-1}), and SnSe (2.6/2.4 Wm^{-1}K^{-1}) along the respective directions [94]. On the other hand, 2D Ge$_2$S exhibits a room temperature κ_l of ~29 Wm^{-1}K^{-1}, which is the highest among the predicted 2D Ge$_x$S$_y$ compounds and close to that of phosphorene in the zigzag direction [116]. The novel stable phase of 2D GeS$_2$ has 16.95/10.68 W/m^{-1}K^{-1} along the zigzag/armchair directions at 300 K, larger than the reported value for its meta-stable 1T phase [95]. The anisotropy of κ_l can be quantified by the ratio κ_{aa}/κ_{bb}, where κ_{aa} and κ_{bb} represent the κ_l values along a- and b-axes, respectively. In the case of GeS$_2$, we designate the a-axis as the zigzag direction and the b-axis as the armchair direction [see Fig. 4.7(c)]. For 2D GeS, this ratio is exactly one, indicating isotropic phonon transport. Similarly, for 2D Ge$_2$S, the ratio is nearly one, implying a predominantly isotropic nature of κ_l. Interestingly, the in-plane anisotropy ratio κ_{aa}/κ_{bb} is 1.59 for the predicted stable 2D GeS$_2$, which is higher than other orthorhombic 2D IV-VI compounds such as GeS (1.35), GeSe(1.29), SnS (1.07), and SnSe (1.08), indicating giant in-plane anisotropic lattice thermal conductivity. Although phosphorene exhibits a larger in-plane anisotropy ratio of 2.21 [116] compared to 2D GeS$_2$, it is prone to stability issues at ambient temperatures [117]. Such intrinsic anisotropic materials are rare and of particular importance in nanodevice applications. Moreover, Figs. 4.11(a-c) show a consistent decrease in κ_l as the temperature increases, displaying a strong adherence to the $1/T$ relationship, as indicated by the solid fitting line in each plot. This trend is commonly observed in intrinsic 2D materials and is attributed to the dominant occurrence of three-phonon scattering via the umklapp process, which depends on temperature directly. The umklapp scattering process opposes heat flow by scattering phonons in the opposite direction, impeding their effective transport. In contrast, the phonon-phonon scattering by the normal process could not provide resistance to phonon transport [43].

Nanostructuring is a common approach to control the κ_l of a material. Generally, decreasing the grain size causes a reduction in the phonon's mean free path (MFP) Λ, resulting in a lower κ_l while keeping the electronic conductivity unchanged. This behavior offers significant potential for enhancing the system's thermoelectric figure of merit. The cumulative κ_l as a function of MFP in Figs. 4.11(d-f) provides insights into the effect of grain size on the κ_l of 2D Ge$_x$S$_y$ compounds at 300 K. To investigate the MFP range that dominantly contributes to κ_l, we fit the data with a logistic function $\kappa(\Lambda \leq \Lambda_{max}) = \kappa_{max}/(1 + \frac{\Lambda_0}{\Lambda})$, where κ_{max} is the ultimate lattice thermal conductivity, Λ_0 is the fitting parameter called the representative

MFP at which cumulative κ_l reaches 50% of its maximum value. The higher values of Λ_0, i.e., 569/371 nm for Ge_2S and 125/170 nm for GeS_2 compared to other IV-VI monolayers [118], indicate that nanostructuring will be highly effective in reducing their κ_l. In contrast, the low phonon MPF Λ_0 of 16.5 nm for GeS, comparable to orthorhombic IV-VI monolayers, implies that it will be hard to reduce its κ_l with nanostructuring and other methods like alloying might be a convenient way. For a given nanostructure size of 50 nm, the κ_l is reduced to 5.70/7.45 $Wm^{-1}K^{-1}$ for Ge_2S and 5.54/2.75 $Wm^{-1}K^{-1}$ for GeS_2, which becomes competitive with κ_l (5.83 $Wm^{-1}K^{-1}$) of GeS. The evident anisotropy in the Λ_0 for Ge_2S and GeS_2 along the a/b-axes implies that reducing the grain size of the system will have different impacts on the κ_l along the a-axis compared to the b-axis. Similar anisotropic trends in Λ_0 for phosphorene allotropes are reported in previous studies [119]. This anisotropy offers intriguing possibilities for tailoring the κ_l by providing additional flexibility for design purposes. The analysis of the cumulative κ_l at various temperatures within the range of 300-600 K for 2D Ge_2S and 300-800 K [see Fig. 4.12] for 2D GeS and GeS_2 demonstrates a uniform decrease in Λ_0 as the temperature rises.

Understanding the mechanisms involved in heat conduction through lattice vibrations in 2D Ge_xS_y compounds requires a comprehensive analysis. We calculate the phonon group velocities by the formula $v_\lambda = \frac{\partial \omega_\lambda(q)}{\partial q}$, where λ represents mode index, ω frequency, and q the wave vector of the phonon, and the results are shown in Fig. 4.13. The first look of Fig. 4.13 shows the lower group velocities, i.e., below the 6 km/s, in all 2D Ge_xS_y compared to other 2D materials like graphene, silicene [120], MoS_2 [121], phophorene [116], and the overall lower κ_l can be attributed to it. However, Figs. 4.13(b, e) depict comparable group velocities in the frequency range 200-300 cm^{-1} of optical phonon to its acoustic branches and higher than the optical phonon of Ge_2S and GeS_2. It implies that the lower group velocity alone does not guarantee the lower κ_l, and further investigation is required, particularly in conjunction with phonon lifetimes. The phonon lifetimes, which represent the time a phonon can exist before scattering with other lattice vibrations, for 2D Ge_xS_y compounds are shown in Figs. 4.14 (a-c). Specifically, the short phonon lifetimes of less than 10 ps in 2D GeS indicate frequent scattering events. These scattering events impede the heat transfer through the lattice, resulting in the reduced κ_l of GeS compared to Ge_2S and GeS_2.

The anisotropic κ_l observed in 2D GeS_2 can be attributed to the anisotropic group velocities of both acoustic and low-frequency optical phonons in the frequency 50-150 cm^{-1} range. Figs. 4.13(b, e) provide evidence of larger group velocities along the $\Gamma - X$ reciprocal lattice direction compared to the $\Gamma - Y$ direction in GeS_2 for acoustic and low-frequency optical phonons. This anisotropy in group velocities directly translates into anisotropic κ_l along the respective crystallographic directions. The frequency range of 50-150 cm^{-1}, mainly
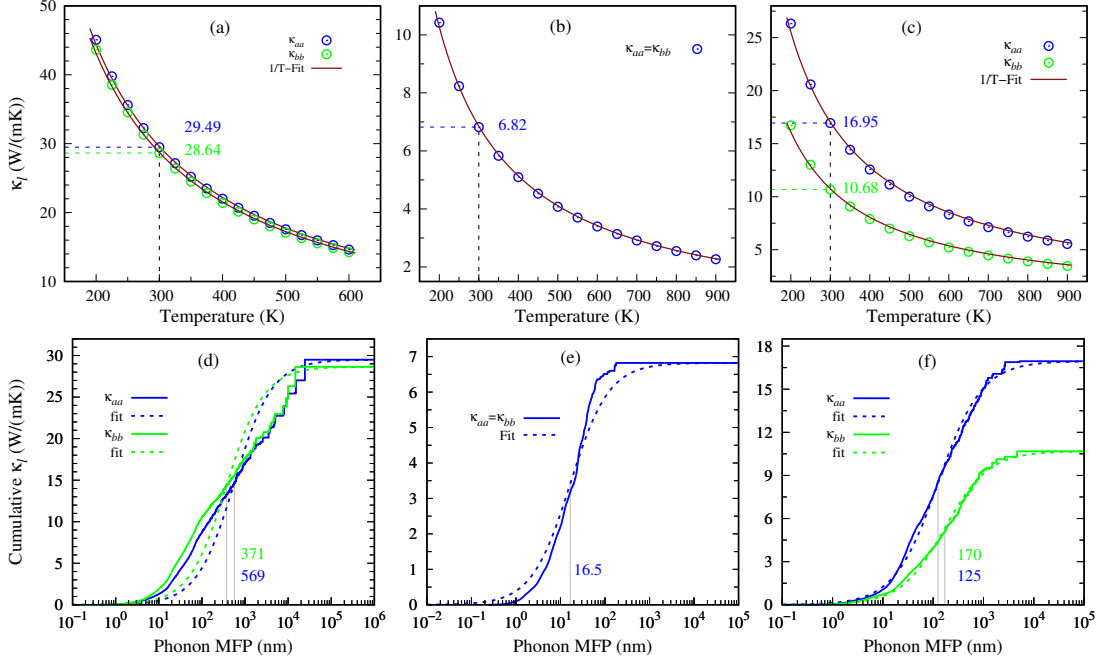
Figure 4.11: The lattice thermal conductivity as a function of temperature and the corresponding $1/T$ fitting for 2D materials (a) Ge$_2$S, (b) GeS, and (c) GeS$_2$. The cumulative κ_l is plotted against the phonon mean free path (MFP) and fitted using the expression $\kappa(\Lambda \leq \Lambda_{max}) = \kappa_{max}/(1 + \frac{\Lambda_0}{\Lambda})$ for (d) Ge$_2$S, (e) GeS, and (f) GeS$_2$, where the value (in nm) of the fitting parameter Λ_0 along a/b-axis is mentioned in each case.
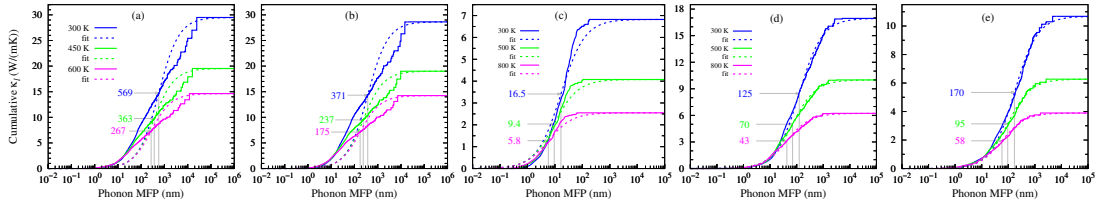
Figure 4.12: The cumulative κ_l is plotted against the phonon mean free path (MFP) and fitted using the expression $\kappa(\Lambda \leq \Lambda_{max}) = \kappa_{max}/(1 + \frac{\Lambda_0}{\Lambda})$, where Λ_0 is the fitting parameter. Panels (a) and (b) depict 2D Ge$_2$S along the a- and b-axes at temperatures of 300 K, 450 K, and 600 K. Panel (c) represents 2D GeS, while panels (d) and (e) illustrate GeS$_2$ along the a- and b-axes at temperatures of 300 K, 500 K, and 800 K. Λ_0 in units of nm is indicated with the corresponding colors in each case.
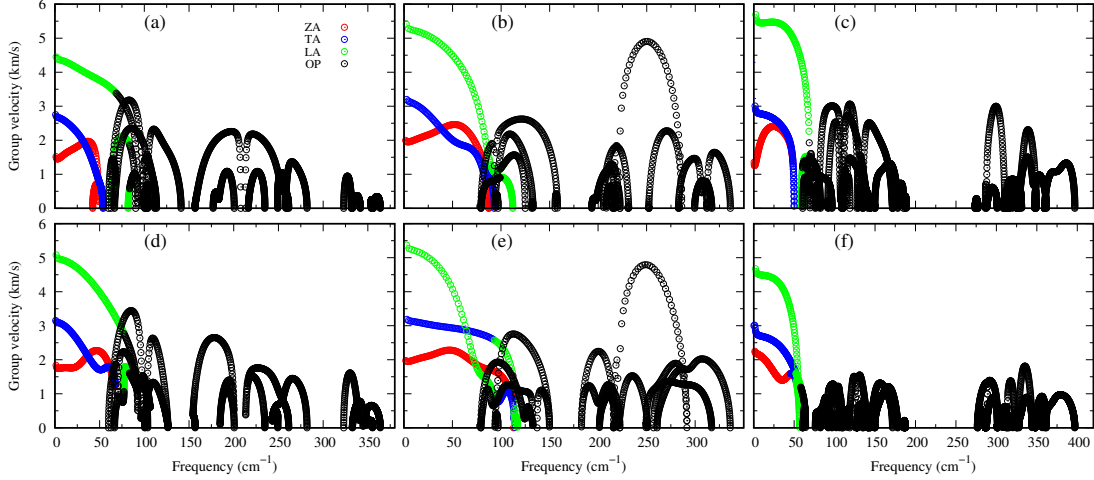
Figure 4.13: Figures (a, b, c) shows the phonon group velocity (v_λ) along $\Gamma - X$ for Ge$_2$S, GeS, and GeS$_2$, while (d, f) represents v_λ along $\Gamma - Y$ for Ge$_2$S, GeS$_2$, and (e) along $\Gamma - K$ for GeS, repectivley.

populated by optical phonons in GeS$_2$ and Ge$_2$S compositions, plays a crucial role due to the larger phonon lifetimes observed within this range. While heat transfer typically dominates by acoustic phonons, the acoustic-optical (low-frequency) phonon coupling effect allows for exceptions to this trend, as demonstrated in a recent study of nitride perovskite LaWN$_3$, where 60% of heat transfer occurs through optical phonons [122]. In the case of GeS$_2$ and Ge$_2$S, the phonon lifetimes within the mentioned frequency range are approximately 20 ps, which is four times longer than the lifetimes observed in GeS (~5 ps), evident from insets as enlarged views in Figs. 4.14(a-c). It highlights the significant role played by low-frequency optical phonons in heat transport. The frequency-resolved cumulative κ_l analysis [see Fig. 4.15(c)] further confirms the substantial contributions of low-frequency optical phonons to the overall κ_l. Moreover, the thermal anisotropy in GeS$_2$ aligns with its elastic properties. The zigzag direction exhibits a larger Young's modulus than the armchair direction, resulting in a larger κ_l along the zigzag direction.

Importantly, within the dominant heat-carrying frequency range (see Fig. 4.15), the phonon lifetimes of 2D Ge$_2$S and GeS$_2$ are significantly large than those of 2D GeS. However, this increase does not correspond to a proportional rise in κ_l. It highlights that phonon-phonon scattering cannot solely be determined by phonon lifetimes. Therefore, we investigate the lattice anharmonicity and the weighted phase space for three-phonon scattering. In Fig. 4.16, we display the Grüeisen parameter $\gamma_\lambda(q) = -\frac{a_0}{\omega_\lambda(q)}\frac{\partial \omega_\lambda(q)}{\partial a}$, where a_0 represents the equilibrium lattice constant, serving to quantify lattice anharmonicity of materials. Additionally, the weighted phase space W of three-phonon scattering (as defined by Wu Li [123]) for 2D Ge$_x$S$_y$
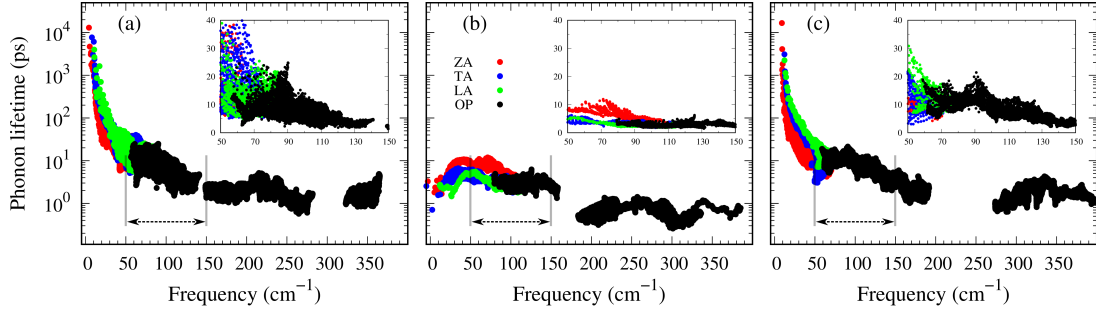
Figure 4.14: Phonon lifetimes of 2D Ge_2S, GeS, and GeS_2 are shown in Figures (a), (b), and (c), respectively. The insets display the enlarged view for visual comparison in the frequency range of 50~150 cm^{-1}.
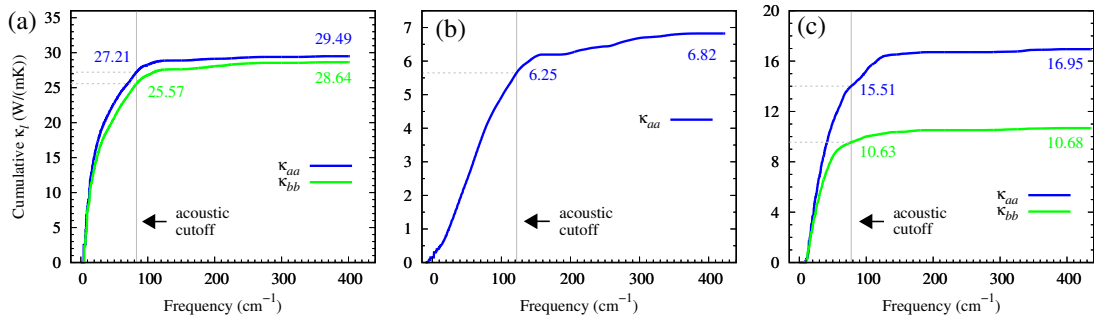
Figure 4.15: The cumulative κ_l along the a/b-axis versus phonon frequency for 2D (a) Ge_2S, (b) GeS, and (c) GeS_2 at 300 K. The vertical gray line in each case shows the maximum frequency of acoustic phonons named acoustic cutoff. The values in blue and green colors in these figures are the κ_l at specified acoustic cutoff in units of $Wm^{-1}K^{-1}$.
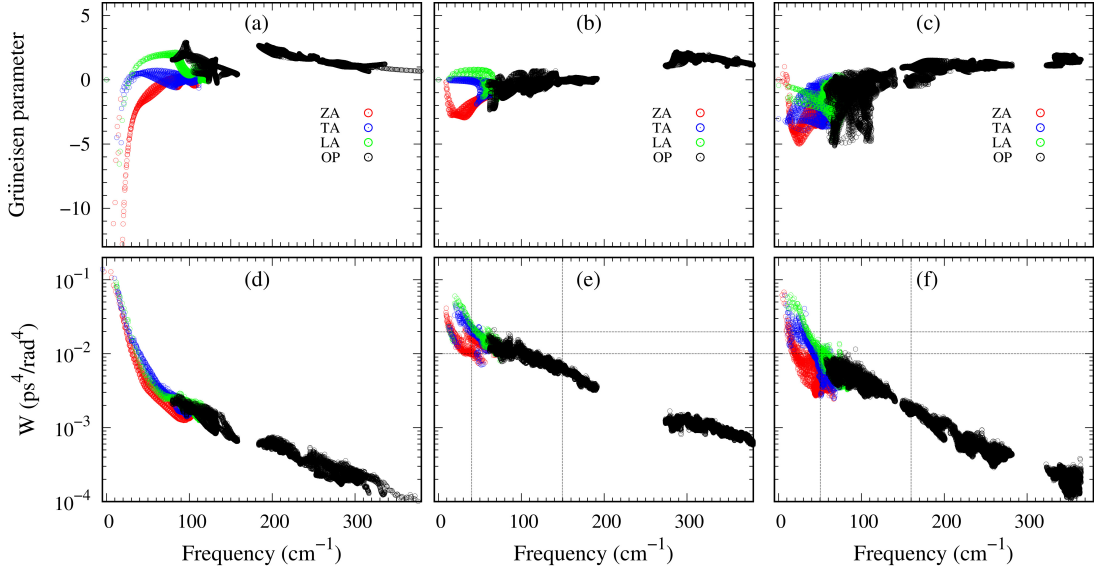
Figure 4.16: Phonon-mode-resolved Grüneisen parameter and the room temperature weighted phase space (W) for (a, d) 2D GeS, (b, e) 2D GeS$_2$, and (c, f) 2D Ge$_2$S. The gray dashed lines (in c and f) aid in visually comparing the W within the 50-150 cm^{-1} frequency range.

is presented in the lower panel of Fig. 4.16. Both these parameters, i.e., γ and W, exhibit an inverse relationship with phonon lifetimes, providing additional insights. The large magnitude of γ and phase space W in the range of acoustic frequencies, which serve as the primary heat carriers, is evident from Figs. 4.16(a, d) and aligns with the lower κ_l of 2D GeS. On the other hand, a comparison of γ, W between 2D Ge$_2$S and 2D GeS$_2$ reveals that while the $|\gamma|_{max}$ of Ge$_2$S (~5) is greater than that of 2D GeS$_2$ (~3), the weighted phase space for Ge$_2$S decreases significantly compared to GeS$_2$ as phonon frequency increases within the frequency range of 150 cm^{-1}. Consequently, the weaker anharmonicity of 2D GeS$_2$ is compensated by the larger three-phonon weighted phase space, resulting in a smaller κ_l compared to 2D Ge$_2$S. The large W can be attributed to the higher phonon population in the lower-optical branches, as shown in Fig. 4.3(c), due to the greater number of atoms in the primitive unit cell of GeS$_2$, increasing the probability of phonon-phonon scattering [124]. Furthermore, the higher phase space [as observed in Fig. 4.16(e)] of GeS$_2$ in the frequency range of 150 cm^{-1} supports our argument regarding its considerable anisotropic κ_l, attributed to both acoustic and low-frequency optical phonons within the 50-150 cm^{-1} frequency range.

4.4   Conclusions

In this manuscript, we present the discovery of novel energetically stable 2D configurations for Ge_2S, GeS, and GeS_2 structures, achieved through the utilization of the USPEX in conjunction with VASP. Their dynamic, elastic, and thermal stabilities are confirmed using state-of-the-art methods. Subsequently, we characterize their electronic structures, revealing semiconducting nature with narrow, medium, and wide band gaps for Ge_2S, GeS, and GeS_2, respectively. Then we focus on their lattice thermal conductivity (κ_l), which provides insights into their heat transport properties. All structures exhibit overall low κ_l values, with 2D GeS having the lowest value of 6.82 $Wm^{-1}K^{-1}$. We observe a significant decrease in κ_l of 2D Ge_2S and GeS_2 with decreasing grain size, suggesting that nanostructuring could further suppress their κ_l. Through a comprehensive analysis of the underlying mechanisms, we uncover the factors contributing to the observed low κ_l in 2D GeS and the in-plane anisotropy in 2D GeS_2. In 2D GeS, the combination of shorter phonon lifetimes, strong anharmonicity, higher weighted phase space, and smaller group velocities accounts for its low κ_l. The κ_l anisotropy of 2D GeS_2 is attributed to the anisotropic group velocities of both acoustic and low-frequency optical phonons. The low-frequency optical phonons in 2D Ge_2S and GeS_2 exhibited lifetimes four times longer than 2D GeS, resulting in increased κ_l. These findings contribute to the fundamental understanding of heat transport in 2D Ge_xS_y compounds, which have potential in thermal management and related fields.

Chapter 5

Summary and oultook

5.1 Summary

This thesis primarily focused on exploring the ground-state structures of 2D configurations of non-layered bulk materials like Cd-Te and Ge-S. The motivation behind this study stemmed from the successful synthesis of silicene and germanene, both derived from non-layered bulk structures. CdTe and GeS, lacking preferred cleavage planes, offered the potential for diverse 2D structures. CdTe, known for its direct band gap and relevance in solar cell applications, and GeS, a prominent member of IV-VI compounds in thermoelectrics, were particularly chosen for investigation. The search process was facilitated and rendered reliable through the combined use of USPEX and VASP. Consequently, 2D CdTe with four atoms and $CdTe_2$ with six atoms in the unit cell were identified as the ground states for their compositions. Similarly, three novel 2D structures: Ge_2S (six atoms), GeS (four atoms), and GeS_2 (twelve atoms) in the Ge_xS_y system, were discovered. These structures, residing on the convex hull, could be attributed to the polymorphic characteristic of Ge_xS_y compounds. Notably, the predicted structures exhibited lower formation energies than the already reported ones, demonstrating the reliability of the search process. In the case of 2D CdTe, the search results validated the previously reported structure, confirming its ground-state nature. This success not only provided ground-state structures but also revealed metastable structures outlined in a full convex hull. These metastable structures sometimes displayed unique properties and could potentially be synthesized under specific experimental conditions. It's crucial to emphasize the significance of determining ground-state 2D structures for Cd_xTe_y and Ge_xS_y in experimental synthesis. Worth noting is that all the 2D predicted structures, except CdTe, lacked counterparts in the bulk phases.

Additionally, these low-energy structures underwent rigorous dynamical, elastic, and thermal stability tests through state-of-the-art first-principles methods to validate their experimen-

tal viability. Detailed electronic structure studies were conducted on 2D CdTe and CdTe$_2$. 2D CdTe exhibited a direct band gap of 1.92 eV, while 2D CdTe$_2$ displayed an indirect band gap of 1.79 eV. Thickness and strain effects, common in experimental synthesis, were comprehensively analyzed. Unlike transition metal dichalcogenides (TMDCs), the direct band gap nature of 2D CdTe was found to be highly robust to both thickness and strain. Although its magnitude decreased from 1.92 to 1.59 eV with increasing thickness from monolayer to bulk, this robustness could have significant implications for solar energy conversion, as it is hindered by the direct-to-indirect transition seen in other TMDCs.

Furthermore, due to the semiconductor behavior of 2D Ge$_x$S$_y$ compounds, where heat flow primarily occurs through lattice vibrations, their lattice thermal conductivity was thoroughly studied using a full iterative solution of PBTE. Among them, 2D GeS exhibited a lattice thermal conductivity of 6.82 Wm^{-1}K^{-1}, lower than its 2D orthorhombic counterpart, making it promising for thermoelectric applications. Meanwhile, 2D GeS$_2$ displayed highly anisotropic lattice thermal conductivity with a ratio of 1.59, surpassing other 2D IV-VI compounds. Investigating the factors behind these excellent properties of 2D GeS revealed that the smaller group velocities, shorter phonon lifetimes, and a high phase space for three-phonon scattering are responsible for its ultralow lattice thermal conductivity. In the case of 2D GeS$_2$, the giant anisotropy in the lattice thermal conductivity could be attributed to the anisotropic phonon group velocities of the acoustic and low-energy optical branches, which were identified as the premier heat carriers in these materials. Finally, a nanostructuring mechanism was suggested for 2D Ge$_2$S and GeS$_2$ to further reduce lattice thermal conductivity, while other techniques like doping could prove beneficial for 2D GeS.

5.2   Outlook

Understanding the significance of ground state structures, which is located at global minimum of the energy surface, is crucial for experimentalists. However, some meta-stable structures, like the 1T and 1T′ structures of two-dimensional metal chalcogenides [125], have been successfully realized experimentally. These meta-stable configurations frequently exhibit exceptional properties compared to their ground state. Therefore, investigating meta-stable structures, as exemplified by 2D CdTe$_4$ and GeS$_4$, is essential. This investigation needs to comprehensively explore both electrical and lattice transport properties.

In this context, our preliminary findings have shown ultralow lattice thermal conductivity, surpassing that of other reported 2D materials. The active surfaces of 2D layers in bulk materials, owing to incomplete coordinations, require passivation with halogens or oxygen to prevent surface reactivity. Interestingly, these passivations sometimes enhance the desired

properties of the monolayer like in the case of phosphorene [126]. In our preliminary results, we observed enormous suppression in lattice thermal transport within the 2D layer, which holds promising potential for applications in thermometric devices.

In the future, our research will continue to focus on these two compelling directions. We aim to delve deeper into these phenomena, paving the way for innovative advancements in the field.

List of publications

1. **Asad Ali** and Young-Han Shin, "Strain and thickness effects on the electronic structures of low-energy two-dimensional Cd_xTe_y phases", *Physical Chemistry Chemical Physics*, **24** (2022) 29772–29780.

2. **Asad Ali** and Young-Han Shin, "Prediction of novel ground-state structures and analysis of phonon transport in two-dimensional Ge_xS_y compounds", *Physical Chemistry Chemical Physics,* **26** (2023) 602-611.

3. Muhammad Sheeraz, Mamoon Ur Rashid, **Asad Ali**, Fazli Akram a, Ho Jeong Lee, Jin San Choi, Jong-Seong Bae, Yong Soo Kim, Young-Han Shin, Chang Won Ahn, and Tae Heon Kim, "Stabilization of 6H-Hexagonal $SrMnO_3$ Polymorph by Al_2O_3 insertion", *Journal of the European Ceramic Society*, **41** (2021) 5155–5162.

4. Hamid Ullah, M Waqas Iqbal, **Asad Ali**, N A Noor, Young-Han Shin, Muhammad Junaid, Iqbal Khan, and H I El Saeedy, "Effects of gallium and arsenic substitution on the electronic and magnetic properties of monolayer SnS", *Physica Scripta*, **96** (2021) 095803.

Bibliography

[1] G. Chen, *Nanoscale Energy Transport and Conversion: A Parallel Treatment of Electrons, Molecules, Phonons, and Photons* (Oxford University Press, 2005).

[2] W. Li, J. Carrete, N. A. Katcho, and N. Mingo, Computer Physics Communications **185**, 1747 (2014).

[3] W. L. Mao, H.-k. Mao, P. J. Eng, T. P. Trainor, M. Newville, C.-c. Kao, D. L. Heinz, J. Shu, Y. Meng, and R. J. Hemley, Science **302**, 425 (2003).

[4] X.-F. Zhou, G.-R. Qian, X. Dong, L. Zhang, Y. Tian, and H.-T. Wang, Physical Review B **82**, 134126 (2010).

[5] K. S. Novoselov, A. K. Geim, S. V. Morozov, D. Jiang, Y. Zhang, S. V. Dubonos, I. V. Grigorieva, and A. A. Firsov, Science **306**, 666 (2004).

[6] J. Li, M. Chen, A. Samad, H. Dong, A. Ray, J. Zhang, X. Jiang, U. Schwingenschlögl, J. Domke, C. Chen, Y. Han, T. Fritz, R. S. Ruoff, B. Tian, and X. Zhang, Nature Materials **21**, 740 (2022).

[7] H. Zheng, X.-B. Li, N.-K. Chen, S.-Y. Xie, W. Q. Tian, Y. Chen, H. Xia, S. B. Zhang, and H.-B. Sun, Physical Review B **92**, 115307 (2015).

[8] P. Kumari, S. Debnath, and P. Mahadevan, Physical Review B **97**, 041404 (2018).

[9] E. Unsal, R. T. Senger, and H. Sahin, Journal of Materials Chemistry C **5**, 12249 (2017).

[10] F. Iyikanat, B. Akbali, J. Kang, R. T. Senger, Y. Selamet, and H. Sahin, Journal of Physics: Condensed Matter **29**, 485302 (2017).

[11] Q. H. Wang, K. Kalantar-Zadeh, A. Kis, J. N. Coleman, and M. S. Strano, Nature Nanotechnology **7**, 699 (2012).

[12] M. Born and R. Oppenheimer, Annalen der Physik **389**, 457 (1927).

[13] L. H. Thomas, Mathematical Proceedings of the Cambridge Philosophical Society **23**, 542 (1927).

[14] E. Fermi, Rend. Accad. Naz. Lincei **6**, 32 (1927).

[15] P. Hohenberg and W. Kohn, Physical Review **136**, B864 (1964).

[16] W. Kohn and L. J. Sham, Physical Review **140**, A1133 (1965).

[17] J. P. Perdew and Y. Wang, Physical Review B **45**, 13244 (1992).

[18] J. P. Perdew, K. Burke, and M. Ernzerhof, Physical Review Letters **77**, 3865 (1996).

[19] J. P. Perdew, K. Burke, and M. Ernzerhof, Physical Review Letters **78**, 1396 (1997).

[20] A. D. Becke, The Journal of Chemical Physics **98**, 1372 (1993).

[21] K. Kim and K. D. Jordan, The Journal of Physical Chemistry **98**, 10089 (1994).

[22] J. P. Perdew, M. Ernzerhof, and K. Burke, The Journal of Chemical Physics **105**, 9982 (1996).

[23] J. Heyd, G. E. Scuseria, and M. Ernzerhof, The Journal of Chemical Physics **118**, 8207 (2003).

[24] G. Kresse and J. Hafner, Physical Review B **49**, 14251 (1994).

[25] G. Kresse and J. Furthmüller, Physical Review B **54**, 11169 (1996).

[26] G. Kresse and D. Joubert, Physical Review B **59**, 1758 (1999).

[27] P. E. Blöchl, Physical Review B **50**, 17953 (1994).

[28] A. D. Becke and K. E. Edgecombe, The Journal of Chemical Physics **92**, 5397 (1990).

[29] A. Martín Pendás, E. Francisco, and M. A. Blanco, Chemical Physics Letters **454**, 396 (2008).

[30] B. Silvi and A. Savin, Nature **371**, 683 (1994).

[31] K. Koumpouras and J. A. Larsson, Journal of Physics: Condensed Matter **32**, 315502 (2020).

[32] A. Le Bail, Journal of Applied Crystallography **38**, 389 (2005).

[33] B. Dong, Z. Wang, N. T. Hung, A. R. Oganov, T. Yang, R. Saito, and Z. Zhang, Physical Review Materials **3**, 013405 (2019).

[34] Q. Li, D. Zhou, W. Zheng, Y. Ma, and C. Chen, Physical Review Letters **110**, 136403 (2013).

[35] L. Zhang, Y. Wang, J. Lv, and Y. Ma, Nature Reviews Materials **2**, 1 (2017).

[36] X.-F. Zhou, X. Dong, A. R. Oganov, Q. Zhu, Y. Tian, and H.-T. Wang, Physical Review Letters **112** (2014).

[37] A. R. Oganov and C. W. Glass, The Journal of Chemical Physics **124**, 244704 (2006).

[38] C. W. Glass, A. R. Oganov, and N. Hansen, Computer Physics Communications **175**, 713 (2006).

[39] G. Benenti, D. Donadio, S. Lepri, and R. Livi, La Rivista del Nuovo Cimento **46**, 105 (2023).

[40] G. Fugallo, M. Lazzeri, L. Paulatto, and F. Mauri, Physical Review B **88**, 045430 (2013).

[41] J. M. Ziman, *Electrons and Phonons: The Theory of Transport Phenomena in Solids* (OUP Oxford, 1960).

[42] R. Peierls, in *Selected Scientific Papers of Sir Rudolf Peierls*, World Scientific Series in 20th Century Physics, Vol. Volume 19 (CO-PUBLISHED BY IMPERIAL COLLEGE PRESS AND WORLD SCIENTIFIC PUBLISHING CO., 1997) pp. 15–48.

[43] C. Kittel, *Introduction to Solid State Physics* (Wiley, 2004).

[44] W. Li, L. Lindsay, D. A. Broido, D. A. Stewart, and N. Mingo, Physical Review B **86**, 174307 (2012).

[45] G. P. Srivastava, *The Physics of Phonons* (CRC Press, 1990).

[46] A. J. H. McGaughey, M. I. Hussein, E. S. Landry, M. Kaviany, and G. M. Hulbert, Physical Review B **74**, 104304 (2006).

[47] A. A. Maradudin and A. E. Fein, Physical Review **128**, 2589 (1962).

[48] L. Paulatto, F. Mauri, and M. Lazzeri, Physical Review B **87**, 214303 (2013).

[49] A. Shah, *Solar Cells and Modules* (Springer Nature, 2020).

[50] M. A. Green, Y. Hishikawa, E. D. Dunlop, D. H. Levi, J. Hohl-Ebinger, M. Yoshita, and A. W. Ho-Baillie, Progress in Photovoltaics: Research and Applications **27**, 3 (2019).

[51] P. Hatton, M. J. Watts, A. Abbas, J. M. Walls, R. Smith, and P. Goddard, Nature Communications **12**, 4938 (2021).

[52] H. Steinberger, Progress in Photovoltaics: Research and Applications **6**, 99 (1998).

[53] J. Zayed and S. Philippe, International Journal of Toxicology **28**, 259 (2009).

[54] V. M. Fthenakis, M. Fuhrmann, J. Heiser, A. Lanzirotti, J. Fitts, and W. Wang, Progress in Photovoltaics: Research and Applications **13**, 713 (2005).

[55] Z. A. Peng and X. Peng, Journal of the American Chemical Society **123**, 183 (2001).

[56] S. Ithurria, M. D. Tessier, B. Mahler, R. P. S. M. Lobo, B. Dubertret, and A. L. Efros, Nature Materials **10**, 936 (2011).

[57] Z. A. VanOrman, C. R. Conti, G. F. Strouse, and L. Nienhaus, Chemistry of Materials **33**, 452 (2021).

[58] K. S. Novoselov, A. K. Geim, S. V. Morozov, D. Jiang, Y. Zhang, S. V. Dubonos, I. V. Grigorieva, and A. A. Firsov, Science **306**, 666 (2004).

[59] S. Cahangirov, M. Topsakal, E. Aktürk, H. Şahin, and S. Ciraci, Physical Review Letters **102**, 236804 (2009).

[60] Y. Sun, Z. Sun, S. Gao, H. Cheng, Q. Liu, J. Piao, T. Yao, C. Wu, S. Hu, S. Wei, and Y. Xie, Nature Communications **3**, 1057 (2012).

[61] S. Acharya, B. Das, U. Thupakula, K. Ariga, D. D. Sarma, J. Israelachvili, and Y. Golan, Nano Letters **13**, 409 (2013).

[62] Y.-L. Hong, Z. Liu, L. Wang, T. Zhou, W. Ma, C. Xu, S. Feng, L. Chen, M.-L. Chen, D.-M. Sun, X.-Q. Chen, H.-M. Cheng, and W. Ren, Science **369**, 670 (2020).

[63] J. Wang, J. Meng, Q. Li, and J. Yang, Physical Chemistry Chemical Physics **18**, 17029 (2016).

[64] J. Zhou, J. Huang, B. G. Sumpter, P. R. C. Kent, Y. Xie, H. Terrones, and S. C. Smith, The Journal of Physical Chemistry C **118**, 16236 (2014).

[65] P. Garg, S. Kumar, I. Choudhuri, A. Mahata, and B. Pathak, The Journal of Physical Chemistry C **120**, 7052 (2016).

[66] M. Naseri, A. Bafekry, M. Faraji, D. M. Hoat, M. M. Fadlallah, M. Ghergherehchi, N. Sabbaghi, and D. Gogova, Physical Chemistry Chemical Physics **23**, 12226 (2021).

[67] T. S. Bush, C. R. A. Catlow, and P. D. Battle, Journal of Materials Chemistry **5**, 1269 (1995).

[68] S. M. Woodley, P. D. Battle, J. D. Gale, and C. R. A. Catlow, Physical Chemistry Chemical Physics **1**, 2535 (1999).

[69] S. M. Woodley, in *Applications of Evolutionary Computation in Chemistry*, Structure and Bonding, edited by R. L. Johnston (Springer, Berlin, Heidelberg, 2004) pp. 95–132.

[70] A. R. Oganov, A. O. Lyakhov, and M. Valle, Accounts of Chemical Research **44**, 227 (2011).

[71] S. Grimme, J. Antony, S. Ehrlich, and H. Krieg, Journal of Chemical Physics **132**, 154104 (2010).

[72] A. Togo and I. Tanaka, Scripta Materialia **108**, 1 (2015).

[73] G. J. Martyna, M. L. Klein, and M. Tuckerman, The Journal of Chemical Physics **97**, 2635 (1998).

[74] B. Wan, Z. Gao, X. Huang, Y. Yang, L. Chen, Q. Wang, C. Fang, W. Shen, Y. Zhang, H. Ma, H. Gou, X. Jia, and Z. Zhang, ACS Applied Energy Materials **5**, 9549 (2022).

[75] M. S. Sokolikova and C. Mattevi, Chemical Society Reviews **49**, 3952 (2020).

[76] D. Dombrowski, A. Samad, C. Murray, M. Petrović, P. Ewen, T. Michely, M. Kralj, U. Schwingenschlögl, and C. Busse, ACS Nano **15**, 13516 (2021).

[77] O. I. Malyi, K. V. Sopiha, and C. Persson, ACS Applied Materials & Interfaces **11**, 24876 (2019).

[78] P.-F. Liu, T. Bo, J. Xu, W. Yin, J. Zhang, F. Wang, O. Eriksson, and B.-T. Wang, Physical Review B **98**, 235426 (2018).

[79] M. Maździarz, 2D Materials **6**, 048001 (2019).

[80] O. Zakharov, A. Rubio, X. Blase, M. L. Cohen, and S. G. Louie, Physical Review B **50**, 10780 (1994).

[81] J. Rousset, P. Olsson, B. McCandless, and D. Lincot, Chemistry of Materials **20**, 6550 (2008).

[82] C. Long, Y. Liang, H. Jin, B. Huang, and Y. Dai, ACS Applied Energy Materials **2**, 513 (2019).

[83] X. Wu, J. Dai, Y. Zhao, Z. Zhuo, J. Yang, and X. C. Zeng, ACS Nano **6**, 7443 (2012).

[84] G. Eda, H. Yamaguchi, D. Voiry, T. Fujita, M. Chen, and M. Chhowalla, Nano Letters **11**, 5111 (2011).

[85] J.-H. Yang, Y. Zhang, W.-J. Yin, X. G. Gong, B. I. Yakobson, and S.-H. Wei, Nano Letters **16**, 1110 (2016).

[86] T. Cheiwchanchamnangij and W. R. L. Lambrecht, Physical Review B **85**, 205302 (2012).

[87] B. Tian, J. Li, A. Samad, U. Schwingenschlögl, M. Lanza, and X. Zhang, Advanced Materials , 2201253 (2022), doi:10.102/adma.202201253.

[88] C.-H. Chang, X. Fan, S.-H. Lin, and J.-L. Kuo, Physical Review B **88**, 195420 (2013).

[89] W. H. Chae, J. D. Cain, E. D. Hanson, A. A. Murthy, and V. P. Dravid, Applied Physics Letters **111**, 143106 (2017).

[90] D. Yoon, Y.-W. Son, and H. Cheong, Nano Letters **11**, 3227 (2011).

[91] A. A. Balandin, S. Ghosh, W. Bao, I. Calizo, D. Teweldebrhan, F. Miao, and C. N. Lau, Nano Letters **8**, 902 (2008).

[92] Y. Anno, Y. Imakita, K. Takei, S. Akita, and T. Arie, 2D Materials **4**, 025019 (2017).

[93] M. Zulfiqar, Y. Zhao, G. Li, Z. Li, and J. Ni, Scientific Reports **9**, 4571 (2019).

[94] A. Shafique and Y.-H. Shin, Scientific Reports **7**, 506 (2017).

[95] X. Wang, W. Feng, C. Shen, Z. Sun, H. Qi, M. Yang, Y. Liu, Y. Wu, and X. Wu, Frontiers in Materials **8**, 709757 (2021).

[96] T. Jiang, Y.-J. Zhu, X.-J. Ye, and C.-S. Liu, Journal of Applied Physics **132**, 075001 (2022).

[97] R. E. Abutbul, E. Segev, U. Argaman, G. Makov, and Y. Golan, Advanced Materials **30**, 1706285 (2018).

[98] W. H. Zachariasen, Physical Review **40**, 917 (1932).

[99] Masahiko. Shimada and Frank. Dachille, Inorganic Chemistry **16**, 2094 (1977).

[100] G. Dittmar and H. Schäfer, Acta Crystallographica Section B: Structural Crystallography and Crystal Chemistry **31**, 2060 (1975).

[101] W. H. Zachariasen, The Journal of Chemical Physics **4**, 618 (2004).

[102] Z. V. Popović, M. Holtz, K. Reimann, and K. Syassen, physica status solidi (b) **198**, 533 (1996).

[103] Y. Li, G. Kuang, Z. Jiao, L. Yao, and R. Duan, Materials Research Express **9**, 122001 (2022).

[104] A. Ali and Y.-H. Shin, Physical Chemistry Chemical Physics **24**, 29772 (2022).

[105] G. Kresse and J. Furthmüller, Computational Materials Science **6**, 15 (1996).

[106] X. Gonze and C. Lee, Physical Review B **55**, 10355 (1997).

[107] B. D. Malone and E. Kaxiras, Physical Review B **87**, 245312 (2013).

[108] A. K. Singh and R. G. Hennig, Applied Physics Letters **105**, 042103 (2014).

[109] X. Li, L. Tao, Z. Chen, H. Fang, X. Li, X. Wang, J.-B. Xu, and H. Zhu, Applied Physics Reviews **4**, 021306 (2017).

[110] Z. Gao, X. Dong, N. Li, and J. Ren, Nano Letters **17**, 772 (2017).

[111] L. Zhu, G. Zhang, and B. Li, Physical Review B **90**, 214302 (2014).

[112] G. Qin, X. Zhang, S.-Y. Yue, Z. Qin, H. Wang, Y. Han, and M. Hu, Physical Review B **94**, 165445 (2016).

[113] D. R. Clarke, Surface and Coatings Technology Proceedings of the 29th International Conference on Metallurgical Coatings and Thin Films, **163–164**, 67 (2003).

[114] T. Feng, L. Lindsay, and X. Ruan, Physical Review B **96**, 161201 (2017).

[115] S. Kumar and U. Schwingenschlögl, Chemistry of Materials **27**, 1278 (2015).

[116] G. Qin, Q.-B. Yan, Z. Qin, S.-Y. Yue, M. Hu, and G. Su, Physical Chemistry Chemical Physics **17**, 4854 (2015).

[117] J. D. Wood, S. A. Wells, D. Jariwala, K.-S. Chen, E. Cho, V. K. Sangwan, X. Liu, L. J. Lauhon, T. J. Marks, and M. C. Hersam, Nano Letters **14**, 6964 (2014).

[118] G. Qin, Z. Qin, W.-Z. Fang, L.-C. Zhang, S.-Y. Yue, Q.-B. Yan, M. Hu, and G. Su, Nanoscale **8**, 11306 (2016).

[119] J. Zhang, H. J. Liu, L. Cheng, J. Wei, J. H. Liang, D. D. Fan, P. H. Jiang, and J. Shi, Scientific Reports **7**, 4623 (2017).

[120] B. Peng, H. Zhang, H. Shao, Y. Xu, G. Ni, R. Zhang, and H. Zhu, Physical Review B **94**, 245420 (2016).

[121] B. Peng, H. Zhang, H. Shao, Y. Xu, X. Zhang, and H. Zhu, Annalen der Physik **528**, 504 (2016).

[122] Q. Ren, Y. Li, Y. Lun, G. Tang, and J. Hong, Physical Review B **107**, 125206 (2023).

[123] W. Li and N. Mingo, Physical Review B **91**, 144304 (2015).

[124] C. Liu, C. Wu, T. Song, Y. Zhao, J. Yang, P. Lu, G. Zhang, and Y. Chen, ACS Applied Energy Materials **5**, 15356 (2022).

[125] J. Zhou, J. Lin, X. Huang, Y. Zhou, Y. Chen, J. Xia, H. Wang, Y. Xie, H. Yu, J. Lei, D. Wu, F. Liu, Q. Fu, Q. Zeng, C.-H. Hsu, C. Yang, L. Lu, T. Yu, Z. Shen, H. Lin, B. I. Yakobson, Q. Liu, K. Suenaga, G. Liu, and Z. Liu, Nature **556**, 355 (2018).

[126] S. Lee, S.-H. Kang, and Y.-K. Kwon, Scientific Reports **9**, 5149 (2019).